CHALMERS

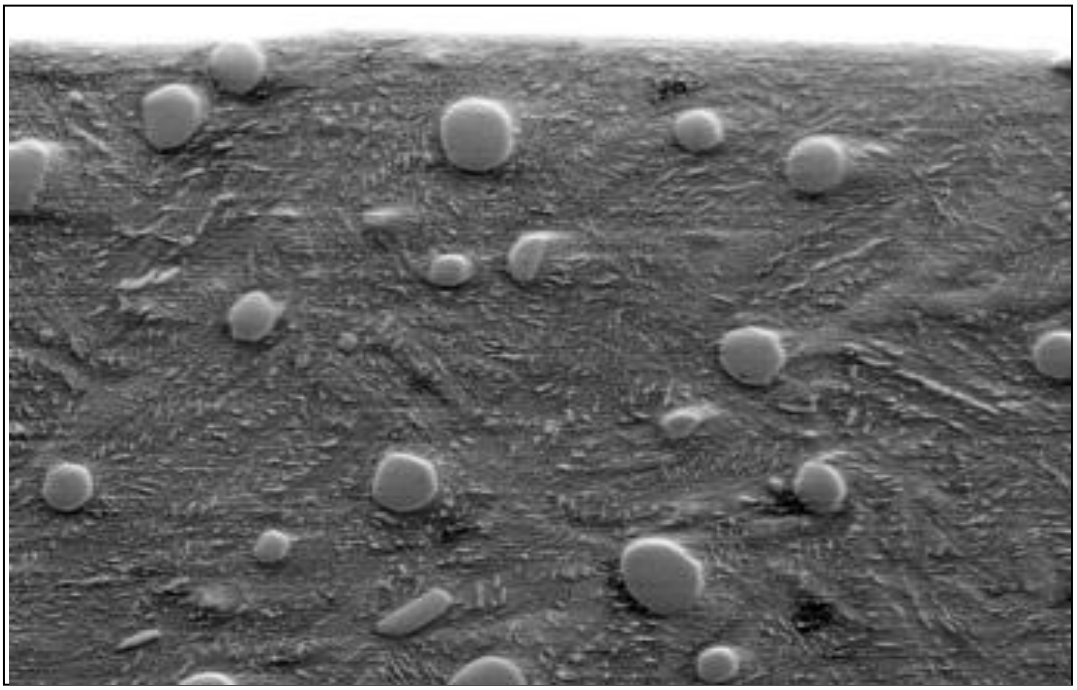

Prediction of Near Surface M_3C after Hard Turning of SAE 52100 Steel

Master of Science Thesis

RICHARD DAHLGREN
Department of Materials and Manufacturing Technology
CHALMERS UNIVERSITY OF TECHNOLOGY
Gothenburg, Sweden, 2011
Report No. 99/2012

Prediction of near surface M_3C-carbides after hard turning of SAE 52100 Steel

by

RICHARD DAHLGREN

Diploma work No. 99/2012
at Department of Materials and Manufacturing Technology
CHALMERS UNIVERSITY OF TECHNOLOGY
Gothenburg, Sweden

Diploma work in the Master program Advanced Engineering Materials

Performed at: SKF AB Manufacturing Development Center
SE- 415 50 Gothenburg

Supervisor: Seyed B. Hosseini
SKF AB Manufacturing Development Center
SE- 415 50 Gothenburg

Examiner: Prof Uta Klement
Department of Materials and Manufacturing Technology
Chalmers University of Technology
SE - 412 96 Gothenburg

Prediction of Near Surface M_3C-carbides after Hard Turning of SAE 52100 Steel
RICHARD DAHLGREN

Diploma work no 99/2012
Department of Materials and Manufacturing Technology
Chalmers University of Technology
SE-412 96 Gothenburg
Sweden
Telephone + 46 (0)31-772 1000

Cover:
[SEM image of M_3C-carbides distributed in a Bainitic matrix.]

Reprosevice
Gothenburg, Sweden 2012

Prediction of Near Surface M_3C-carbides after Hard turning of SAE 52100 Steel

RICHARD DAHLGREN
Department of Materials and Manufacturing Technology
Chalmers University of Technology

SAMMANFATTNING

Materialavverkande processer så som hårdsvarvning och slipning kan orsaka strukturella förändringar av ett arbetsstyckes yta, en sådan förändring är bildandet av skört, hårt och etsresistent skikt som kallas ”vitt skikt”. Det har fått sitt namn ifrån det vita utseendet det har när man studerar det i ljusmikroskop. Trots omfattande forskning kring vita skikt så förstår man inte mekanismerna och förutsättningarna för uppkomsten av det vita skiktet till fullo.

Uppkomsten av det vita skiktet påverkar ytintegriten som i sin tur påverkar egenskaperna hos den bearbetade komponenten. Med bakgrund av detta är det viktigt att förstå karakteristiken kring skapandet av det vita skiktet så som restspänningar, volymfraktion av restaustenit, hårdhet och upplösning av $(Fe,Cr)_3C$- karbider.

I den här studien analyserades upplösning/tillväxt av $(Fe,Cr)_3C$- karbider efter hårdsvarvning. Detta gjordes experimentellt genom Svep Elektron Mikroskop (SEM) samt teoretiskt genom en modell i programmet DICTRA.
Karbiderna karakteriserades med hänsyn till storlek, form och distribution i arbetsstyckets yta med SEM. Datormodellen användes för att simulera hårdsvarningsprocessen genom att applicera tryck och temperatur på arbetsstycket.

SEM-analysen visar på en lägre volymfraktion av karbider för de martensitiska ytorna svarvade med den lägsta hastigheten. Resultaten från simuleringarna visar på en väldigt liten påverkan av karbiderna under de korta värmecykler som materialet utsätts för under hårdsvarningsprocessen.

Nyckelord: $(Fe,Cr)_3C$- karbider, Vitt skikt, Hårdsvarvning , Kullager-stål, SEM, DICTRA, Moving Boundary Model.

Prediction of Near Surface M_3C-carbides after Hard turning of SAE 52100 Steel

RICHARD DAHLGREN
Department of Materials and Manufacturing Technology
Chalmers University of Technology

ABSTRACT

Material removal processes like hard turning and grinding can introduce structural changes in the surface of the workpiece material, such as the formation of a featureless, brittle, hard, and etch-resistant layer. This featureless layer is called “white layer” due to its appearance in light optical microscope. Despite the extensive research results regarding the white layer the fundamental conditions and mechanisms for its formation is not yet fully understood. Due to different microstructure of the white layer the surface integrity is significantly altered, which affects the performance of the machined component. Therefore it is of great importance to understand the characteristics of white layer formation such as residual stresses, volume fraction of retained austenite, hardness as well as dissolution of (Fe,Cr)3C- carbides.

In this study the dissolution/growth of the (Fe,Cr)3C- carbides were analyzed experimentally after hard turning and theoretically by applying a moving boundary model in DICTRA. The carbides were characterized regarding size, shape and distribution at the workpiece surface in Scanning Electron Microscope (SEM). The moving boundary model was used to simulate the hard turning process in terms of temperature and pressure applied to the surface of workpiece.

The SEM-analysis shows a limited dissolution of carbides in the martensitic surfaces machined with low cutting speed. The simulation results indicate that the carbide dissolution is very limited during the short thermal cycles the carbides were exposed to during hard turning.

Keywords: $(Fe,Cr)_3C$- carbides, White layer, Hard turning, Bearing steel, SEM, DICTRA, Moving Boundary Model.

Contents

CHAPTER 1

Introduction

1.1 Background

Hard turning as well as grinding introduces structural changes in the surface of the workpiece material, such as the formation of a featureless, brittle, hard, and etch-resistant layer. The newly formed layer on the machined surface, which also is known as “White Layer”, appears white during visual inspection in the light optical microscope. Despite the knowledge and the amount of research results available about the white layer characteristics, the fundamental conditions and mechanisms for the formation of the white layers are not fully understood. Generally three different mechanisms are supposed to be promoting white layer formation i) plastic deformation ii) rapid heating followed by subsequent rapid cooling an iii) surface reaction with the environment[1]. It is important to investigate if the pressure and/or temperature are high enough to alter the surface/subsurface microstructure (carbide dissolution/grow) during hard turning as the final surface integrity can have a large impact on a machined component.

1.2 Aim & Goals

The goal of this Master thesis is to characterize the carbides close to the surface after machining, in order to be able to study the influence (temperature and pressure) on the material during cutting. The work has been divided into two parts, one practical and one theoretical. The practical part includes microstructure investigation of samples hard turned with different cutting conditions. The theoretical part includes a computer model describing the carbide dissolution/growth during hard turning the computer is evaluated with respect to the results from the experimental analysis.

1.3 Limitations

For the computer simulation only thermal and pressure diffusion kinetics are considered. The computer model used will not consider any shear/strain activated dissolution of the carbides.

CHAPTER 2

Theory

2.1 White layer

During hard turning (turning of hardened steel (60 HRC)) a thermo-mechanically induced layer is formed called “white layer” due to its resistance to etching causing it to appear white in optical microscope and featureless in SEM [2]. This layer is very hard and can have a thickness of 0.5 - 12 µm depending on the process parameters. It is often accompanied by a softer layer beneath, which is known as dark layer and often described as an over-tempered zone. White and dark layer formation is not limited to hard turning as it has also been found in other material removal processes such as reaming, grinding and electrical discharge machining.

2.1.1 Mechanism of white layer formation

The mechanism behind white layer formation is yet not fully understood and therefore there is a wide range of theories trying to explain the occurrence of white layer formation. The next section presents two proposed mechanisms.

Dynamic recovery (Mainly mechanical)

Dynamic recovery is suggested by several authors [3,4,5] to be the main mechanism of white layer formation. It has been observed that certain metals undergoing plastic deformation under high strain rates (10^3 to 10^6) [2] develop adiabatic shear bands. This means that only an insignificant portion of the heat generated during the deformation is dissipated during the short deformation time, making it generally an adiabatic process.
The process can be explained as the beginning of dislocations being arranged in cell boundaries. Assisted by the local increase in temperature due to rapid localized deformation, dislocations concentrate into tangles producing regions of high and low dislocation density and forming sub-grain boundaries [4].

Reverse martensitic transformation (mainly thermal)

Reverse martensitic transformation is a term used for the phase transformation from martensite to austenite. Several reports [6,7,8] have shown increased retained austenite content in the white layer compared to the bulk indicating that white layer formation is accompanied with a phase transformation. Chou and Evans [7] have simulated the hard turning process by using a moving heat source model according to Jaegers theory [9] and found a good agreement with their experimental values from hard turning of SAE 52100 steel. They explain the white layer formation with rapid heating caused by the friction between the tool and the workpiece. The machined surface turns into an austenitic state and when the tool leaves the surface, rapid cooling by convection of the air transforms the machined surface back into a fine grained martensitic structure.

2.2 The Fe-C system

The term “steel” refers to an iron-carbon alloy with carbon content up to 2 wt.% C. With the iron-carbon alloy as a base, other alloying elements such as Cr, Ni, Mo, Mn can be added to obtain desired properties such as hardness, hardenability, and corrosion resistance. A review of the iron-carbon phase diagram reveals 3 allotropes of iron: α-ferrite, δ-ferrite and γ-austenite. The first two allotropes have a bcc (body centered cubic) structure and the latter has an fcc (face centered cubic) structure. The bcc phases of iron have a very limited solubility of carbon compared to the fcc (austenite phase). The difference in solubility is the key to heat treatment of steels. By heating steel up to the austenitic state and allowing it to cool down, a wide range of microstructures can be obtained making it possible to tailor the properties of the steel by using different heat treatments [9].

2.2.1 Martensite

Martensite is one of the phases which may form when steel is rapidly cooled from the austenitic state. The rapid cooling allows for the carbon formerly in solid solution with austenite to stay in solution with the new phase. Therefore, martensite can be considered a supersaturated solid solution of carbon in ferrite, which will decompose into ferrite and cementite given time. The carbon is solved interstitially and provides solution strengthening resulting in a high hardness of the martensite phase.
The martensite transformation is dependent on a high cooling rate to avoid formation of other solid state phases such as ferrite, pearlite or bainite. The critical cooling rate needed can be very high for plain carbon steel but steel alloyed with ferrite-stabilizing solutes (Cr,Mo,Si) suppress the nucleation of the other solid state phases allowing for lower cooling rates.
The transformation from austenite to martensite is a diffusionless process and proceeds through a shearing of the austenite lattice (fcc) into martensite (bct,bcc) resulting a in large deformation and a volume expansion [9].

The morphology of martensite differs depending on the carbon content of the steel. In low carbon steel with up to 0.5 wt.% C, the martensite is arranged in laths. When the carbon content reaches 0.5%, additional plate like martensite starts to develop and the phases coexist up to 1 wt .% C. Carbon content higher than 1% generates only plate martensite.

2.2.3 Bainite

Bainite is formed when the cooling rate is sufficient to avoid ferrite and pearlite but insufficient to form martensite. Bainite is a mixture of carbide and ferrite. There are two forms of bainite, upper and lower bainite. Upper bainite forms at a higher temperature than the lower bainite and is characterized by needles or laths of ferrite with cementite precipitates between the laths, while lower bainite is characterized by fine ferrite plates incorporating dispersed carbides [9].

2.2.4 Cementite

Cementite is a metastable compound between iron and carbon with the formula Fe_3C. It is formed when cooling slowly from austenite to ferrite because of the low solubility of carbon in ferrite. Another way to obtain this phase is by heating of martensite in the range of 150-700°C (tempering) allowing excess carbon to precipitate as carbides. A complete tempering process results in cementite carbides in a ferritic matrix [9].

2.3 SAE 52100

In this investigation a high carbon steel of grade SAE 52100 has been used. The chemical composition of the material is given in Table 1. Both martensite and bainite microstructures were studied with respect to carbide dissolution after hard turning, examples of the both microstructures presented in in Fig. 1.

SAE 52100 is a common steel used in the bearing industry due to its excellent heat treatment properties in terms of hardenability, control of grain size, consistency of spheroidization and resistance to decarburization allowing for both martensitic and bainitic through-hardening depending on the application. It also has good resistance for rolling contact fatigue after appropriate heat treatment.

A key component for its heat treatment properties is the chromium content which increases the ferrite-to-austenite transformation temperature and widens the three phase region of ferrite + austenite + $(Fe,Cr)_3C$. Chromium also results in finer pearlite lamellae which renders finer carbides and improves the spherodization properties. The stability of carbides is also improved which is essential for creating fine grained medium carbon martensite [11].

Table 1 Nominal chemical composition of SAE 52100 in wt%[10]

Element	C	Mn	Si	Cr
Wt.%	1.04	0.35	0.25	1.45

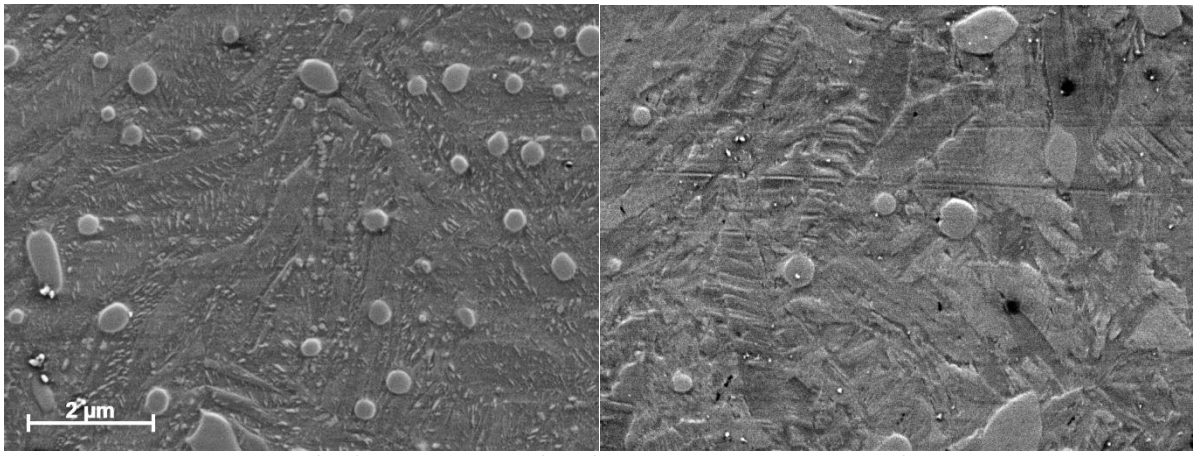

Fig. 1 Example of the bainitic (left) and martensitic (right) microstructure in SAE 52100(The scale bar applies for both images).

2.4 Carbide dissolution

2.4.1 General theory

Carbide dissolution consists of three step, i) decomposition of the carbide ii) atoms from the carbide crossing the interface (carbide/matrix) and iii) diffusion of the atoms from the carbide into the matrix (austenite) [12]. The two first steps proceed relatively fast and the cementite dissolution is determined by the diffusion of chromium and carbon through the austenite phase.

The rate at which the carbides decrease in size depends on the chromium diffusion since the carbon is an interstitial and does not affect the volume of the carbide significantly.

2.4.2 During hard turning

There are many theories and investigations providing different explanations about the dissolution of carbides during hard turning ranging from complete dissolution to unaffected carbides. This section aims to cover some of the investigations supporting the different results.

Complete dissolution

Zurecki et al. [13] showed that there is almost a complete dissolution of surface carbides during hard turning which increases the carbon content of the matrix and thereby decreases the melting point. They explain it in a 3-step process:

(I) The thermal input and plastic shearing of the machined surface result in a substantial increase in temperature, an extensive microstructural refinement, and a nearly complete dissolution of carbides in the surface layer.

(II) As hard carbides dissolve in the hot, austenitic matrix of the machined surface, the material strength decreases to the point of unlocking a catastrophic shear. The mechanism of carbide dissolution and the accompanied loss in strength is self-feeding since the melting point (solidus) of the steel decreases with increasing amount of carbon entering the matrix from dissolved carbides.

(III) A rapid cooling of the sheared layer with the tool departure results in 'freezing in-place' of the submicron, white layer structure. Small areas of unquenched martensite and retained austenite may develop within or just below the sheared layer.

Unaffected carbides

Because of the high heating and cooling rates, Chou and Evans [7] claim that there is insufficient time for the martensite to decompose and that the carbides are therefore unaffected. They also stated that martensite transforms to austenite by a massive transformation (diffusionless).

Partial dissolution of carbides

Barry and Byrne [8] have seen refinement of carbides during white layer formation in hard turning. They have proposed that the refinement could be due to dissolution of carbides and re-precipitation upon cooling. Turley [14] suggested that the carbides have been annihilated by the dispersion of carbon to dislocations, vacancies and subgrain boundaries.

2.5 Turning

Turning like many other machining operations is accomplished by straining a local region of the workpiece to fracture by the relative motion of the tool and the workpiece. Machining is normally employed to produce shapes with good dimensional tolerances and surface integrity.
The two axis of motion are called primary and feed motion. The primary motion is the main motion and is provided by the rotation of the workpiece and the feed motion is a linear motion of the tool in the axial direction aimed to facilitate continuous material removal.

2.5.1 Cutting tool and wear

The cutting tool is a vital part in the turning operation and the tool can be designed in various ways for different applications. The general geometry is summarized in Fig. 2.

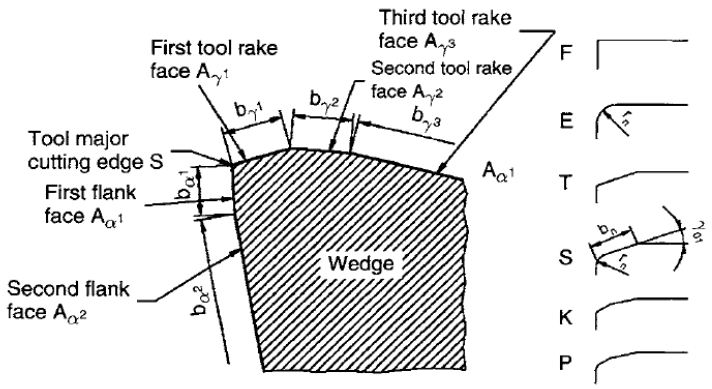

Fig. 2 General geometry of a cutting tool and variants of cutting edge shapes, in courtesy of Elsevier [15]

During the turning operation, the tool is subjected to heavy load and high temperature which causes the tool to deteriorate over time. Damages of the tool are classified into two groups, wear and fracture. Fracture is characterized by catastrophic failure like cracking or chipping of the tool whereas wear is characterized by a continuous and progressive loss of material from the tool.

Common wear types

- *Crater wear*: observed on the rake face and primarily caused by a chemical interaction between rake face and the hot chip.

- *Flank wear:* observed on the flank and caused by abrasive action of hard constituents such as Fe_3C and non-metallic inclusions in the workpiece material.

- *Built-up edge (BUE):* adhering of the chip to the tool tip causing attrition of the tool when the adhered material breaks off.

- *Notch wear:* primarily caused by oxidation of the tool generating a notch in the flank face.

- *Thermal cracks: c*racks in the tool generated by repeated heating and cooling [15].

2.5.2 Forces

The force applied by the tool on the workpiece can be divided in to three components, see Fig. 3. These are the cutting force, F_c, which acts in tangential direction, the feed force, F_f, which acts in direction of the feed (axial direction), and the passive force, F_p, which acts in radial direction [15].The passive force is the significant force when it comes to pressure of the workpiece, since its counterforce is directed into the workpiece.

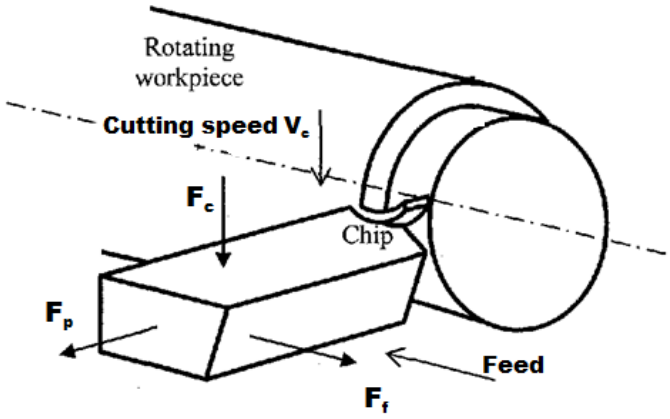

Fig. 3 Forces active during turning, in courtesy of K. Philip Varghese [16]

2.5.3 Heat

Metal cutting generates a significant amount of heat since the power used for plastic deformation is largely converted into heat near the tool cutting edge. The heat is generated in three zones as described below and shown in Fig. 4 [15]:

1. Primary shear zone located in the shear plane; heat generated due to intensive plastic deformation.
2. Secondary shear zone located at the tool/chip interface; heat generated due to friction.
3. Tertiary shear zone in the contact between workpiece and the flank due to friction; heat generation in this zone increases with flank wear since the contact area is increased with wear. This heat generation is of great importance for white layer formation in the workpiece.

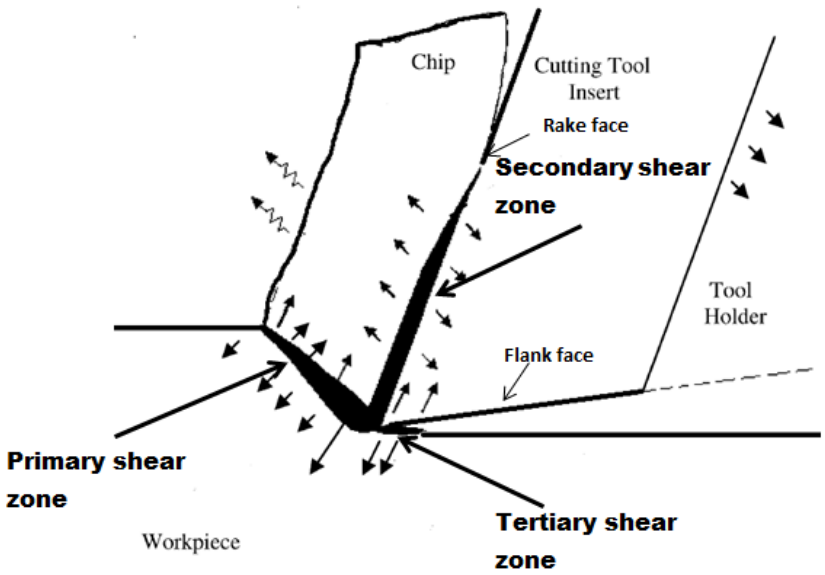

Fig. 4 Heat zones and heat flow during turning, in courtesy of Elsevier [17]

The heat generated and the fluxes between the chip, tool and workpiece are strongly influenced by the cutting speed. When the cutting speed is increased, the time in which heat flows into the

workpiece and the tool is shortened. This result in a higher amount of heat carried away by the chip, hence reducing the amount of heat going in to the workpiece. The correlation can be seen in Fig. 5.

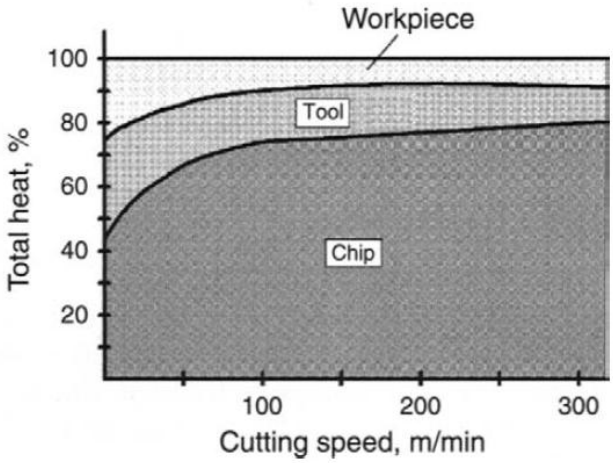

Fig. 5 Percentage of generated heat transferred into the workpiece, tool and chip as a function of cutting speed, in courtesy of Elsevier [15].

2.5.4 Hard turning

Hard turning is a term used for turning of materials with a hardness exceeding 45 HRC. This process generates more heat and higher cutting forces than conventional turning of softer materials. To be able to cut these hard materials even harder cutting tools are needed and cubic boron nitride (CBN) inserts are commonly used.

2.6 Multicomponent Diffusion theory

Phase transformation is often accompanied with diffusion, a flux of atoms. Diffusion can be explained as nature's way to equalize a solution. Simply put, in presence of a concentration gradient a net flux of atoms will be established in order to reduce the gradient.
Fick's first law describes the connection between the concentration gradient and the flux. The simplest form of the law dealing with an isothermal, isobaric one-phase alloy with diffusion of species k in one direction z is written as

$$J_k = -D_k \frac{\partial c_k}{\partial z} \qquad \text{(Eq 2.6.1)}$$

where J_k is the interdiffusion flux and is often measured in $\left(\frac{mol}{s*m^2}\right)$. c_k is the concentration of species k, and D_k is its diffusivity or the interdiffusion coefficient.
Fick's first law can be combined with the continuity equation

$$\frac{\partial c_k}{\partial t} = \frac{\partial}{\partial z}(-J_k) \qquad \text{(Eq 2.6.2)}$$

to create Fick's second law

$$\frac{\partial c_k}{\partial t} = \frac{\partial}{\partial z}\left(D_k \frac{\partial c_k}{\partial z}\right) \qquad \text{(Eq 2.6.3)}$$

This equation can be used to predict how diffusion causes the concentration to change with time. However, the equation only applies to a single component solution. Commercial alloys contain more than two components; therefore the law must be extended in order to be applicable to a multi component system. This was done by Onsager in 1931 [18], where he suggested that each thermodynamic flux is linearly related to every thermodynamic force, resulting in this expression for an isothermal isobaric system.

$$J_k = -\sum_{i=1}^{n} L'_{ki} \frac{\partial \mu_i}{\partial z} \qquad \text{(Eq 2.6.4)}$$

where μ_i is the chemical potentials for the various components. L'_{ki} is a proportionality factor which depends on the mobility of the different components. The flux J_k is defined as

$$\sum_{k=1}^{n} V_k J_k = 0 \qquad \text{(Eq 2.6.5)}$$

This can be rewritten to express the fluxes as a function of concentration gradients instead of gradients in chemical potential.

$$J_k = -\sum_{i=1}^{n} L'_{ki} \sum_{j=1}^{n} \frac{\partial \mu_i}{\partial c_j} \frac{\partial c_j}{\partial z} \qquad \text{(Eq 2.6.6)}$$

Further, by introducing the unreduced diffusivities,

$$J_k = -\sum_{i=1}^{n} D_{kj} \frac{\partial c_j}{\partial z} \qquad \text{(Eq 2.6.7)}$$

we end up with

$$D_{kj} = -\sum_{j=1}^{n} L'_{ki} \frac{\partial \mu_i}{\partial c_j} \qquad \text{(Eq 2.6.8)}$$

Since $\frac{\partial \mu_i}{\partial c_j}$ are purely thermodynamic quantities we can divide diffusivities into two separate parts, one purely thermodynamic part, ($\frac{\partial \mu_i}{\partial c_j}$), and one kinetic part, L'_{ki}.

The concentration gradients in Eq. 2.6.7 are connected and as a simplification the *n* gradient is often discarded. With the *n* gradient eliminated and the reduced diffusivities introduced, Eq. 2.6.7 now becomes

$$J_k = -\sum_{i=1}^{n-1} D_{kj}^{n} \frac{\partial c_j}{\partial z} \qquad \text{(Eq 2.6.9)}$$

Combining Eq. 2.6.9 with the continuity equation (Eq. 2.6.2) will give a system of coupled partial differential equations which enables calculations in multicomponent alloys. These systems rarely have analytical solutions; hence numerical methods are generally required to solve them [19].

2.7 Thermodynamic and Kinetic databases

To be able to solve the systems in the preceding section, access to both thermodynamic and kinetic data is needed (and as always when it comes to numerical models the accuracy of the results is dependent on the quality of the provided data)

The use of thermodynamic data for calculation of phase diagrams has been around for more than 35 years now. One method which has been very successful is the CALPHAD (CALculation of Phase Diagram) method which expresses the Gibbs energy of individual phases as a function of temperature, composition and pressure [20]. Equilibrium of the desired system is calculated by minimizing the Gibbs energy. The thermodynamic parameters in the model are evaluated from available thermodynamic data from experiments using a minimum sum of squares method to optimize the calculated values to the experimental values

Influenced by the CALPHAD method, Andersson and Ågren [21] developed a method for calculating kinetic data. In their model, the atomic mobility of the individual species in a multicomponent solution phase is modeled as a function of temperature, composition and pressure. Using absolute-reaction theory arguments the mobility coefficient for element B, M_b, is divided into a frequency factor M_B° and an activation enthalpy Q_B

$$M_B = \frac{M_B^\circ}{RT}\ exp\left(\frac{-Q_B}{RT}\right) \qquad \text{(Eq 2.7.1)}$$

where R is the gas constant and T is the absolute temperature. The parameters M_B° and Q_B vary with temperature, composition and pressure. The composition dependency is modeled as a linear combination of the values at each endpoint of the composition space and a Redlich-Kister expansion

$$\phi_B = \sum_i x_i\, \phi_B^i + \sum_i \sum_{j>1} x_i\, x_j \left[\sum_{r=0}^{m} {}^r\phi_B^{i,j}(x_i - x_j)^r\ i\ j\right] \qquad \text{(Eq 2.7.2)}$$

where ϕ_B represents ln M_B° or Q_B. The term ϕ_B^i is the value of ϕ_B for pure i and thus represents one of the endpoint values in the composition space. The term ${}^r\phi_B^{i,j}$ represents binary interaction parameters, the commas separating different species interacting with each other. The terms x_i and x_j are mole fractions for elements i and j, respectively. As in the case when evaluating thermodynamic data, the model parameters are determined by an optimization procedure where experimental data is taken into account. The reason to store the individual mobilities in the database rather than interdiffusion coefficients is a matter of convenience since in an n-component system there are n mobilities and $(n-1)^2$ interdiffusion coefficients. Hence, for a system with more than two components there are less mobilities than interdiffusion coefficients and thus less data needs to be stored. The conversion of mobilities into interdiffusion coefficients is an easy matter if the thermodynamic data for the system is available.

2.8 DICTRA

DICTRA is a simulation tool using thermodynamics to predict diffusion kinetics and phase transformations. Using the DICTRA software several models for different applications have been developed. The model which is applicable in this study is the "moving boundary model" developed by Ågren [20].

2.8.1 Moving boundary model

The moving boundary model handles phase transformations caused by diffusion for example dissolution or growth of particles embedded in a matrix. The basic model consists of two single-phase regions separated by a planar boundary and the boundary migration is determined by the diffusion of atoms to and from the interface. If we have a system with two adjacent phases α and β with one phase growing into the other, the number of moles in a component k should be conserved hence a flux balance equation can be formulated as follows

$$\frac{v^{\alpha}}{V_m^{\alpha}}\left[x_k^a - x_k^{\beta}\right] = J_k^{\alpha} - J_k^{\beta} \qquad k = 1,2 \ldots . n-1 \tag{Eq 2.8.1}$$

Where v^{α} is the interface migration rate, x_k^a and x_k^{β} are the contents of component k in α and β close to the phase interface, and J_k^{α} and J_k^{β} are the corresponding diffusional fluxes. The term V_m^{α} is the molar volume of the α-phase. By calculating the initial boundary condition at the interface, the integration in time can be carried out. If the migration of the phase interface is slow compared to the interfacial reactions, an assumption regarding the local thermodynamic equilibrium at the interface can be made. Applying this commonly used assumption allows the boundary conditions to be determined. This enables the solution of the diffusion problem in the single phases α and β which enables solving of the flux-balance equation (Eq. 2.8.1) and hence determining the migration rate of the phase interface. In a multicomponent case, a system of nonlinear equations will be generated which has to be solved by iteration/numerically.
The assumption of local equilibrium at the interface implies that the chemical potential is constant across the phase interface and that the concentrations of the components can be extracted from a phase diagram. This means that the transformation rate is solely controlled by the diffusion of components to and from the interface. This is a simplification which disregards a number of effects which can influence the transformation kinetics, e.g. curved interfaces, finite mobility of the interface, and solute drag and elastic stresses [22].

2.8.2 Cell model

For more complex problems in a larger system where several moving boundaries are present, a cell model can be used. The moving boundary model described earlier is considered as one cell and to expand the system more cells are added and connected to the previous model.

The cells are interconnected by requiring that the activity of choice is equal at the boundaries of the cells and the total amount of each component is constant. To be able to maintain the overall mass balance the net flux between the cells must be zero. This is achieved by iteratively determine an activity that will result in a zero net sum of fluxes.

The cell size is fixed which renders the outer boundary of the cell immobile and it is only the intracellular boundaries which connect the regions that move depending on growing/shrinking regions [19].

CHAPTER 3

Experimental and analysis techniques

3.1 Hard turning

Before this project was started, a series of turning operations were done in order to analyze the influence of the cutting parameters on the formation of white layer. The tests were carried out on 12 steel rings of AISI 52100 (see section 2.3). Two different heat treatments were carried out to obtain either a martensitic (M1-M6) or a bainitic (B1-B6) microstructure. Prior to final hardening treatment, the microstructure of the steel consisted of evenly distributed spheroidized $(Fe,Cr)_3C$ carbides in a ferritic matrix.

During hard turning, the cutting speed, V_C, and flank wear, V_B, were varied in a systematic way for both bainitic and martensitic rings as shown Fig. 6. All other cutting parameters were kept constant.

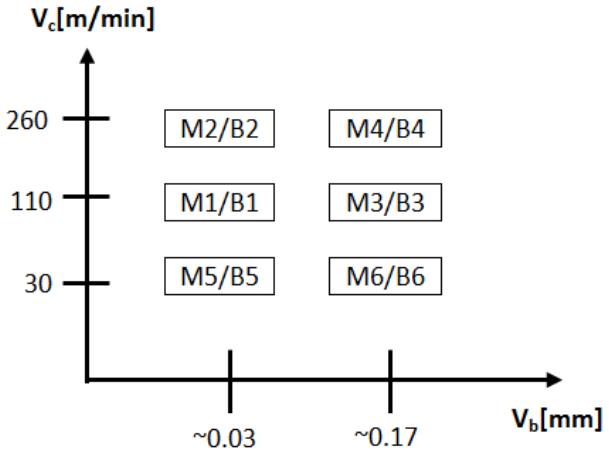

Fig. 6. Cutting speed and flank wear used during cutting tests; M and B denotes martensitic and bainitic structure.

3.2 Sample preparation

Small pieces of the hard tuned rings were cut out from each specimen and hot mounted in Struers Polyfast©™ resin. The samples were cut from the rings according to Fig. 7.

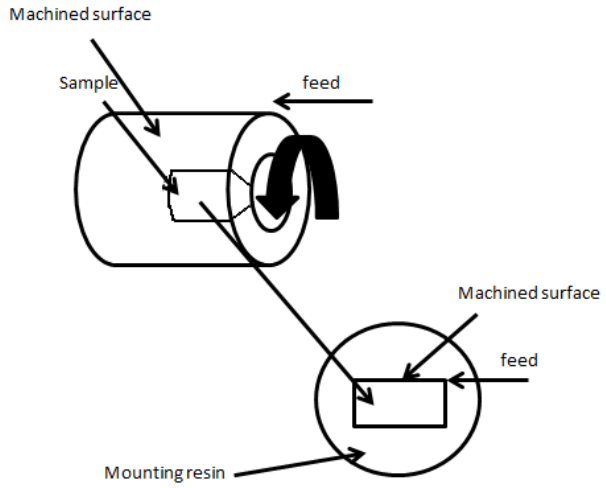

Fig. 7 Sketch showing principally how samples were cut from machined rings and mounted in resin.

After hot mounting, all samples then were polished in 3 steps with 9, 3 and 1 micron diamond paste to a mirror like surface. To enhance the visual detection of the carbides, the samples were also polished with an oxide polishing suspension (OP-S™(Struers)) for 30 minutes. Afterwards, the samples were extracted from the mounting resin and cleaned in an ultrasonic bath in 3 steps, firstly with acetone, secondly with isopropanol and finally with ethanol.
As a final preparation for the SEM investigation, the samples were glued with carbon paste to small holders.

3.3 Scanning Electron Microscopy

All samples were visually analyzed in SEM with the specific setting as shown in Table 2.

Table 2

Machine	Zeiss 1550 Gemini with field emission gun
Accelerating voltage	2.0 kV
Detector	Secondary Electron
Working distance	5-6 mm
Magnification	30.000x

In each of the 12 samples, 5 random positions near the machined surface were chosen. At each position, an area of 21 µm (depth) * 81 µm (length) was selected from which 27 images were recorded as described in Fig. 8. For reference carbide distribution within the material, an area of 7*9*15 µm area in the bulk (1mm from the machined surface) of one martensitic (M4) and one bainitic (B5) sample was investigated.

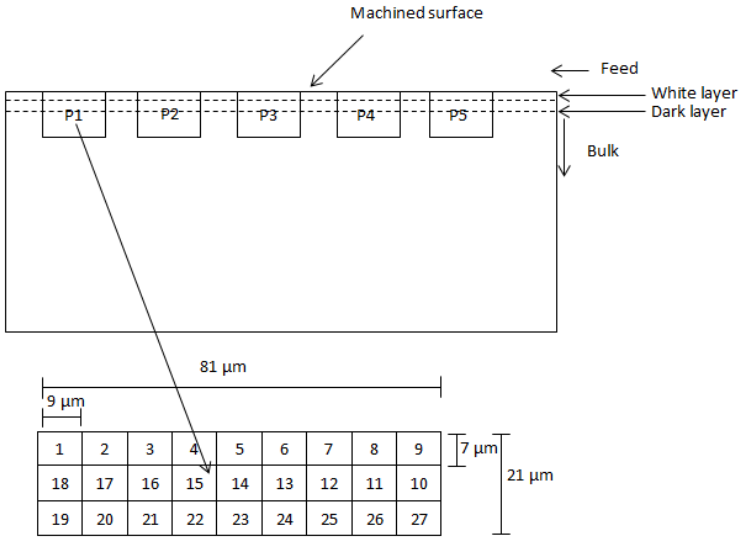

Fig. 8 Schematic view of the imaging setup in SEM

3.4 Image analysis

All images were processed with Photoshop to enhance contrast for easier visual detection of the carbides. The software Axiovision was used to record size, aspect ratio and distance from the surface. All images were processed manually since the contrast between matrix and carbides was insufficient for the auto-detection system in Axiovision.

3.5 DICTRA

Based upon the Moving Boundary Model described in section 1.7.1, a model for carbide dissolution has been developed [23]. This model has been the base for the simulation.

For practical (calculative) reasons, the model is defined in a ternary system with Fe, Cr and C as components disregarding the small amounts of other alloying elements. This is a reasonable simplification since the influence of the other alloying elements is limited as compared to carbon and chromium.

A system of three carbides with sizes corresponding to carbides found in the bulk material during SEM-analysis were modeled using the cell approach with a moving boundary model in each cell as shown in Fig. 9. The cells consist of a spherical carbide region surrounded by an austenite region. Hence, with this model it is assumed that we have a fully austenitic matrix in the beginning due to rapid heating. Furthermore it is assumed that the spheroidal carbides maintain their shape during the entire dissolution process. As described in section 2.8.2, the cells are coupled by requiring zero net flux between them and that the chemical potential for each component at their common border is the same.

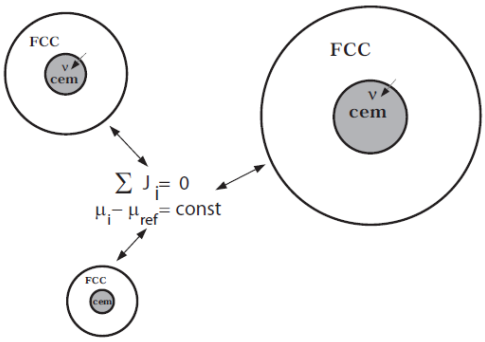

Fig. 9 Sketch showing the principle of the DICTRA model

3.5.1 Parameters for simulation

Temperature

The temperatures that occur in hard turning under the given conditions have been determined in a parallel project. For medium and high cutting speed and high V_B, the measured temperature was well above A_1 temperature which is the temperature where austenite begins to form and carbides dissolve. For the lowest cutting speed and independent of the tool flank wear, the temperature was well below the A_1 temperature. For medium cutting speed and new tool (M5/B5) the temperature was below the A_1 temperature while for the highest cutting speed (M4/B4), the temperature was slightly higher than A_1. For a summary see Fig. 10.

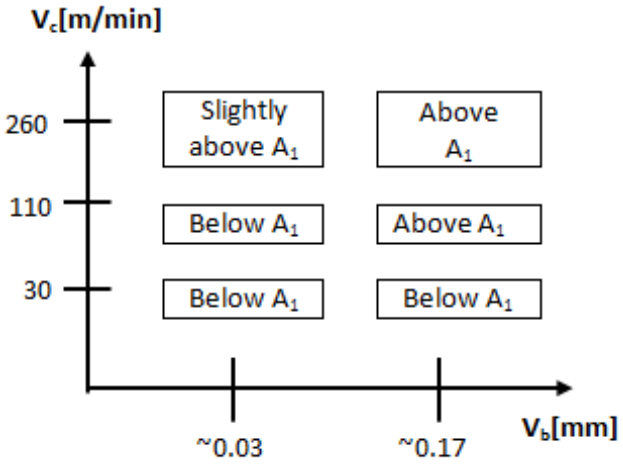

Fig. 10 Estimated temperatures during hard turning

Pressure

The cutting forces were also measured with a piezoelectric dynamometer. As described in section 2.5.2 the passive force F_p is the force acting on the workpiece. After each run the cutting tools were examined to determine the area of the flank wear which coincides with the contact area between

tool and workpiece. A simplified way to determine the contact pressure is to divide the force with the contact area (compare Fig. 11 c).

For practical reasons every simulation was run at 3 different pressure levels, atmospheric pressure, 1 GPa and 4 GPa.

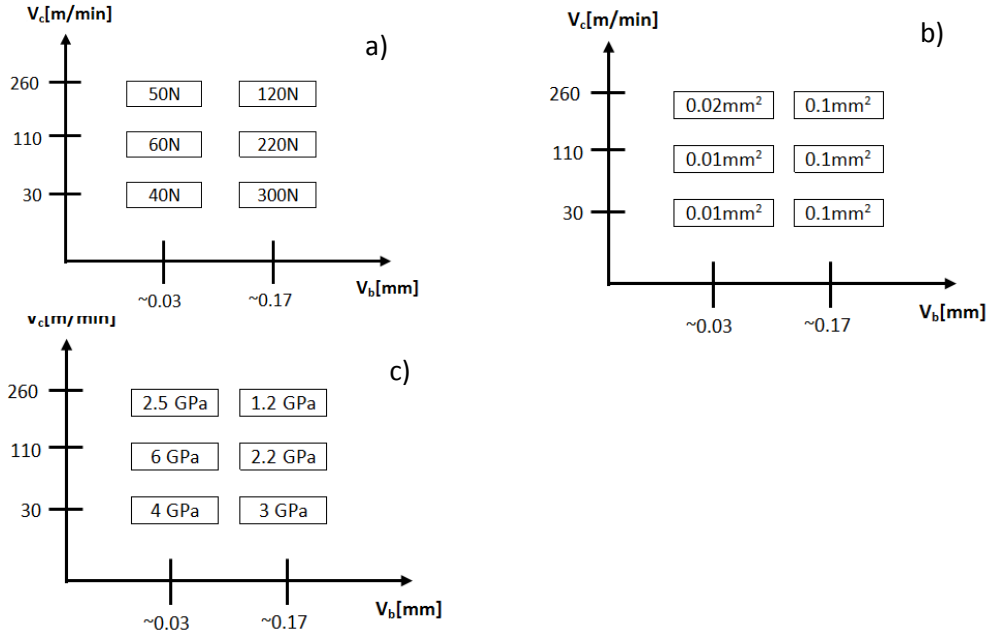

Fig. 11 a) Passive forces F_p measured during machining; b) flank wear/contact area; c) calculated contact pressures

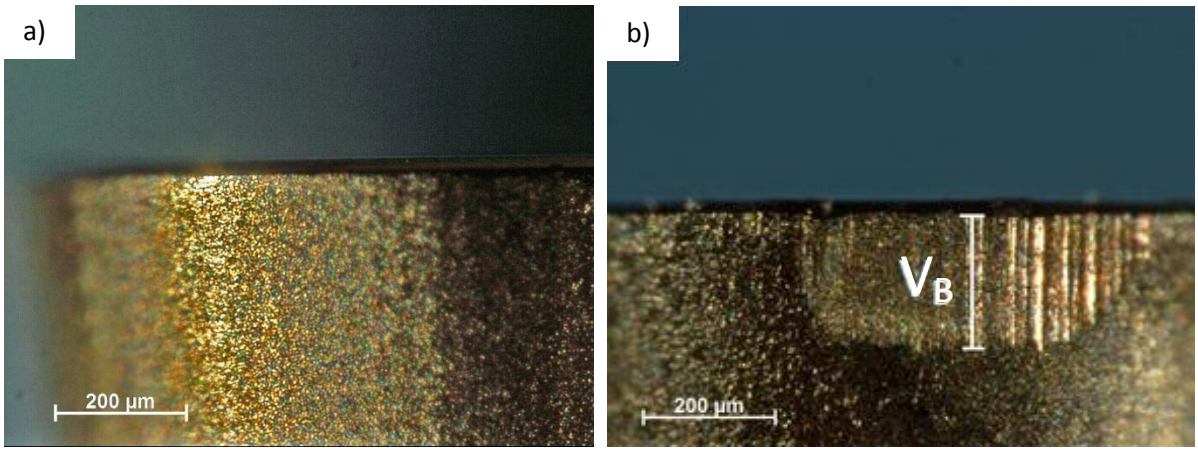

Fig. 12 Optical microscope images showing a new insert a) and a worn insert b).

Simulation Time

The time the material is exposed to increased temperature and pressure depends on the cutting speed and the contact length between the cutting tool and the workpiece. After determining the actual contact time, it was doubled and made into an interval to account for effects the cutting tool has on the material right before and after contact. The contact times for the different cases are provided in Fig. 13.

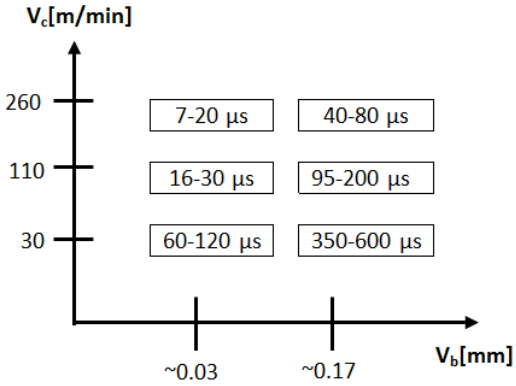

Fig. 13 Contact times for the different samples

A simulation time of 500 µs was used for all simulations except for the one with high wear and slow cutting speed where a simulation time of 1000 µs was chosen.

Carbide and cell sizes

By reviewing the result from the SEM-analysis, three carbide sizes were chosen. The cell sizes were then calculated to adjust the average composition of the simulated system to the alloy composition. The cementite/carbide volume fraction for SAE 52100 with corresponding heat treatment have been approximated to 4-5 vol.% [24]. Knowing this, the cell size can be calculated using the following correlation:

$$r_{tot} = \frac{r_{cem}}{\sqrt[3]{Vf_{cem}}} \qquad \text{(Eq 3.5.1)}$$

where r_{tot} is the radius of the cell r_{cem} is the radius of the carbide Vf_{cem} is the volume fraction of cementite.

Table 3 Carbide diameter, cell diameter and thickness of the austenitic phase used during simulations.

Carbide Diameter [µm]	Cell Diameter [µm]	Thickness of Austenite [µm]
0.50	1.4	0.45
0.25	0.07	0.23
0.20	0.36	0.18

The distance between the carbides was determined by the size of the austenite regions. Those distances were later compared to SEM-analyses to evaluate if the model was a good representation of the material/microstructure.

Composition

The austenite matrix used in the model is assumed to inherit the chemical composition of the prior bainitic and martensitic matrices. They had a carbon content of 0.7 wt.%[24] which results in a chromium content of 1 wt.% in the matrix [11].
The investigated M_3C-carbides are assumed to have a chromium content of 9 wt.% [11].

Evaluation of parameters

Since the designed model during simulation contains only austenite and cementite phases, the simulation results will only be valid for those set of parameters that give access to the respective phase fields in the phase diagram. Therefore, the influence of pressure on the ternary Fe-Cr-C phase

diagram for Fig. 14.a) atmospheric pressure (1 atm), b) 1 GPa, and b) 4 GPa were studied in order to obtain the right process windows prior to the simulation. At the chemical composition used in the system, the temperatures required to enter austenite–cementite phase were i) 740°C at 1 atm, ii) 720°C at 1 GPa and iii) 670 °C at 4 GPa . With this in mind a final test matrix was constructed (Table. 4).

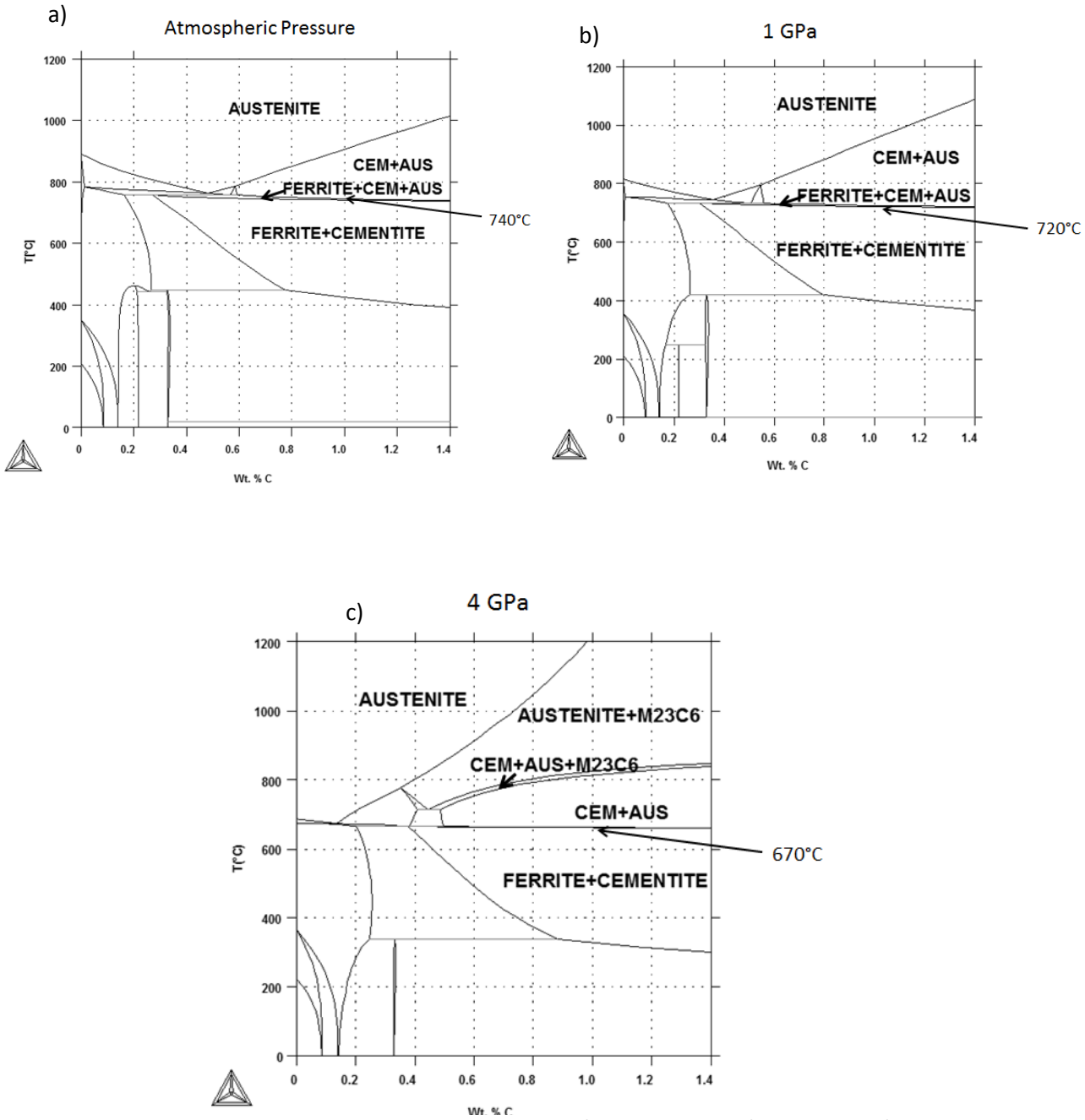

Fig. 14 Ternary phase diagram for the Fe-Cr-C system a) at atm pressure, b) at 1 GPa, and c) at 4 GPa.

Final simulation matrix

Table 4 Final test matrix for DICTRA-simulations

m/min	T[°C]	P	Contact time [µs]	Valid	T[°C]	P	Contact time [µs]	Valid
V_C 260	750	1 atm	7-20	x	1000	1 atm	40-80	x
	750	1 GPa	7-20	x	1000	1 GPa	40-80	x
	750	4 GPa	7-20	x	1000	4 GPa	40-80	x
					950	1 atm	40-80	x
					950	1 GPa	40-80	x
					950	4 GPa	40-80	x
V_C 110	650	1 atm	16-30		900	1 atm	95-200	x
	650	1 GPa	16-30		900	1 GPa	95-200	x
	650	4 GPa	16-30		900	4 GPa	95-200	x
					800	1 atm	95-200	x
					800	1 GPa	95-200	x
					800	4 GPa	95-200	x
V_C 30	450	1 atm	60-120		550	1 atm	350-600	
	450	1 GPa	60-120		550	1 GPa	350-600	
	450	4 GPa	60-120		550	4 GPa	350-600	
mm	**V_B 0.03**				**V_B 0.17**			

CHAPTER 4

Results

The results are divided into two parts. The first one is focusing on the SEM-analysis while the second part is dealing with the material simulations in DICTRA.

SEM analysis

The sample preparation method was optimized to reveal the carbides. Hence, no emphasis was put on enhancing visibility of the bainitic and martensitic structure.
The bulk analysis of the two microstructures showed that the structure of the bulk is similar to the structure at a depth of 18-20 µm.
Visual inspection of all the cross-sections of the surface and subsurface microstructures after hard turning reveals an even distribution of carbides. An example image of the cross-section from each material type is given together with the hard turning conditions in Figs. 15 and 16.
The visual inspection indicates that there was no significant difference in the distribution of the carbides from the surface down to a depth of 20 µm. At the surface as well as at the subsurface both small and large carbides were seen and a detailed distribution of the carbides for each material is shown in Figs. 17 and 18. Furthermore, in samples produced with low cutting speed such as M5/B5 and M6/B6 elongated carbides were observed as shown in Fig. 19. Similar results were observed by plotting carbide aspect ratio greater than 2 versus distance from the machined surfaces as shown in Figs. 20 and 21.
For both microstructures (martensite/bainite) no significant deviation in the mean carbide diameter could be seen except for the bainitic sample machined with high cutting speed and worn tool (B4). For this surface the carbide mean diameter is 0.1 µm lower close to the surface (0-4µm) compared to the mean diameter in the bulk (18-20 µm). For a summary of the mean diameters, see Figs. 22 and 23.

The volume fraction of $(Fe,Cr)_3C$ as a function of distance from surface was plotted for each sample and is provided in Figs. 24 (martensite samples) and 25 (bainite samples), respectively. The technique used for estimation of the volume fraction of $(Fe,Cr)_3C$ is considered to have a measurement error of ±0.5 vol.% [25].

The martensitic samples show a trend: Regardless of flank wear, the samples with the lowest cutting speed show a low volume fraction (≈2.7 vol.%) in the very top layer (0-2 µm). However, it should be emphasized that those surfaces have not reached a temperature above the A1-line for the material.

For the bainitic samples no significant trend indicating lower volume fraction of $(Fe,Cr)_3C$ near the surface is seen.

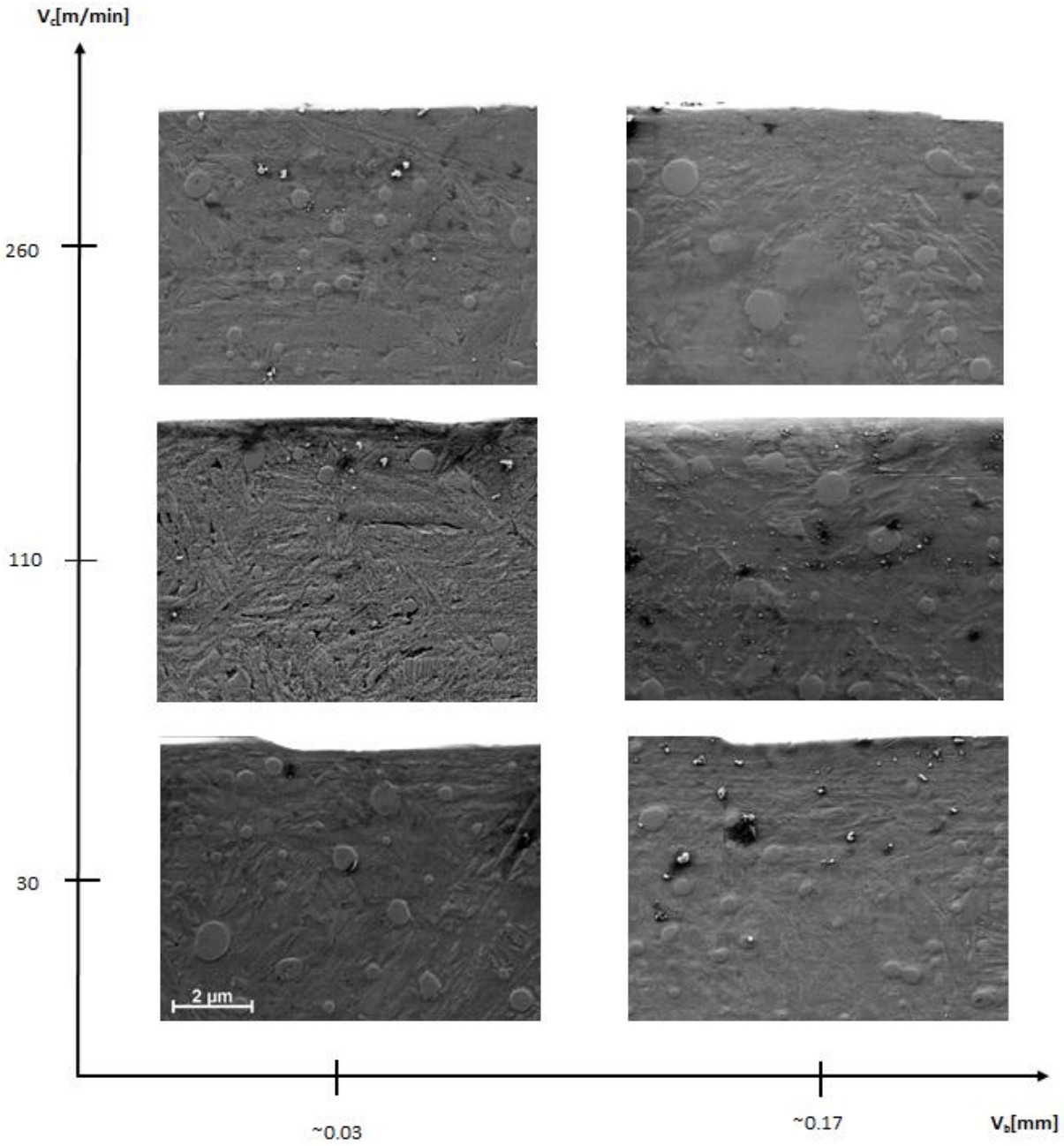

Fig. 15 Microstructures of the 6 martensitic samples. (The scale bar in the lower left image applies for all images)

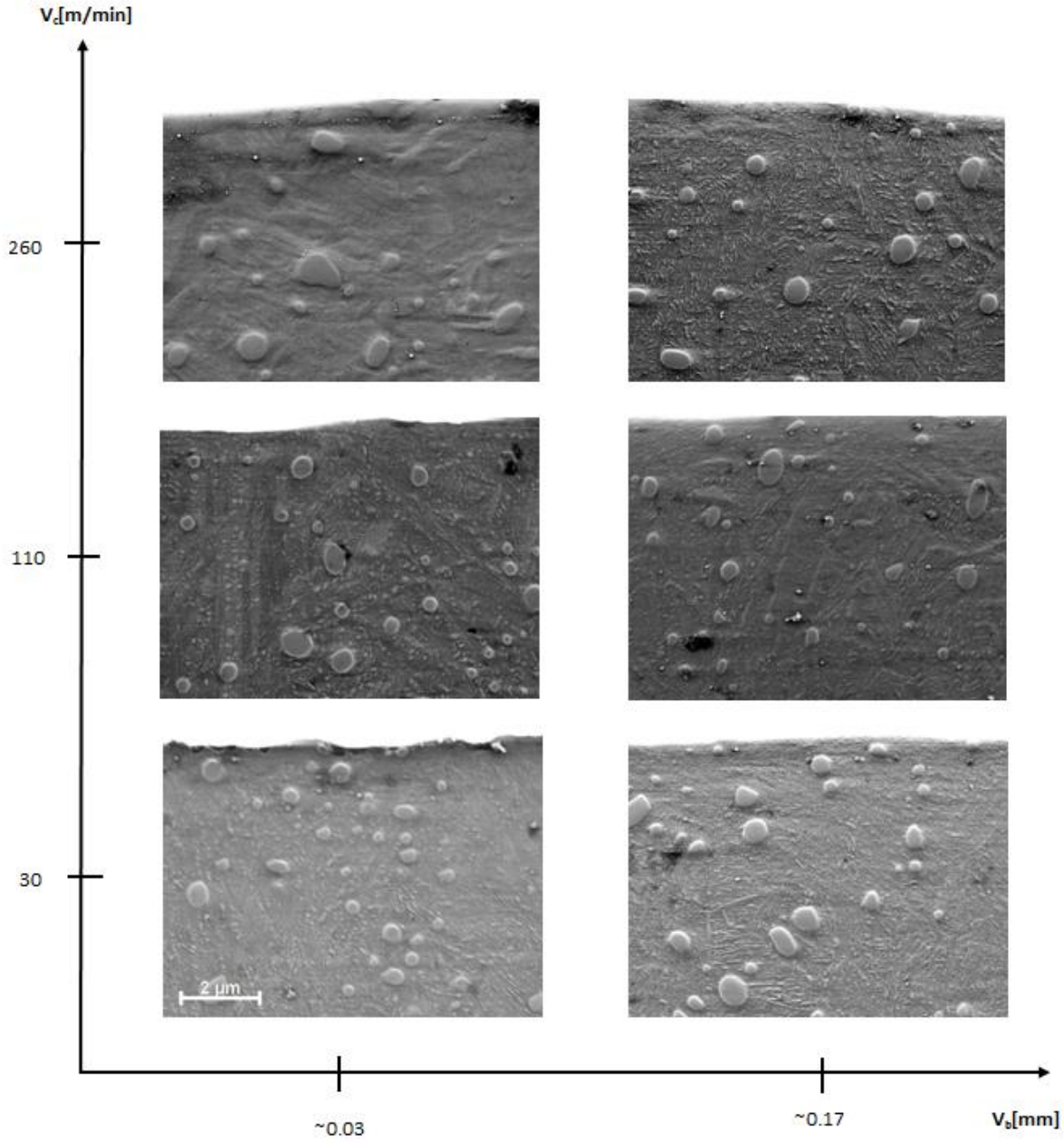

Fig. 16 Example of microstructure of the 6 bainitic samples. (The scale bar in the lower left image applies for all images)

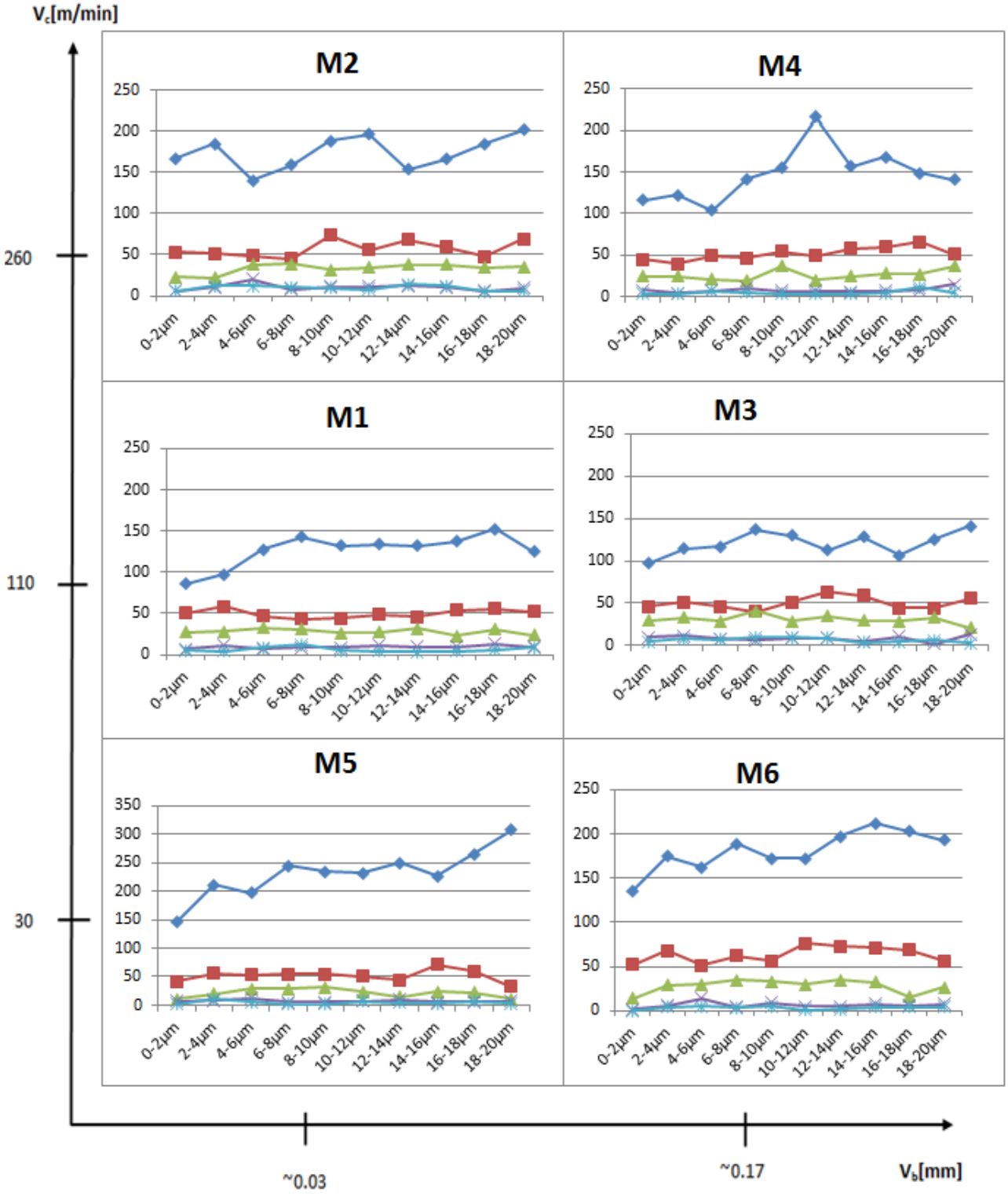

Fig. 17 Graphs showing amount of carbides of different sizes as a function of distance from the machined surface with each line representing an interval of diameter size as follows 0.1-0.36 µm 0.36-0.51 µm 0.51-0.688 µm 0.688-0.830 µm >0.830 µm

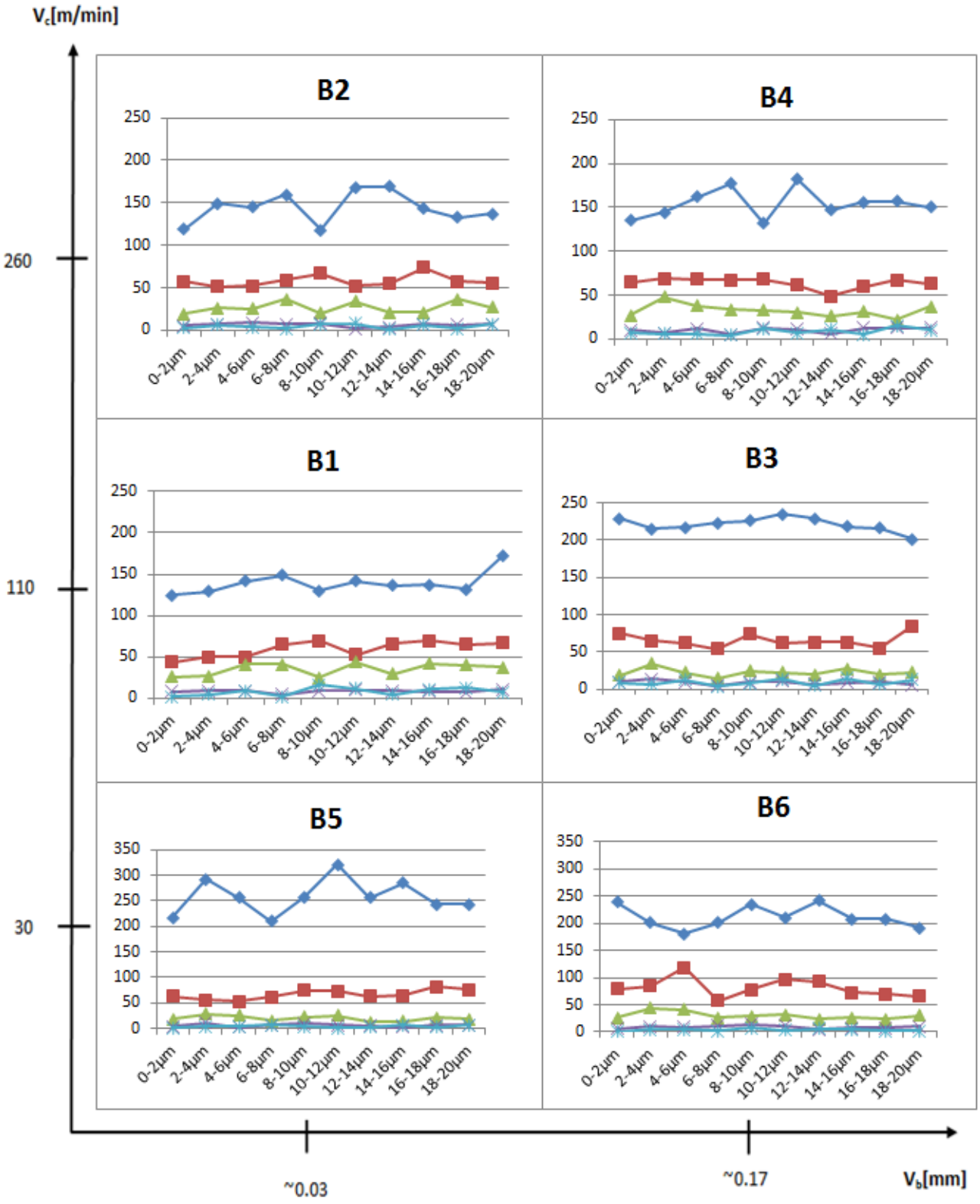

Fig. 18 Graphs showing amount of carbides of different sizes as a function of distance from the machined surface with each line representing an interval of diameter size as follows 0.1-0.36 µm, 0.36-0.51 µm, 0.51-0.688 µm, 0.688-0.830 µm, >0.830 µm

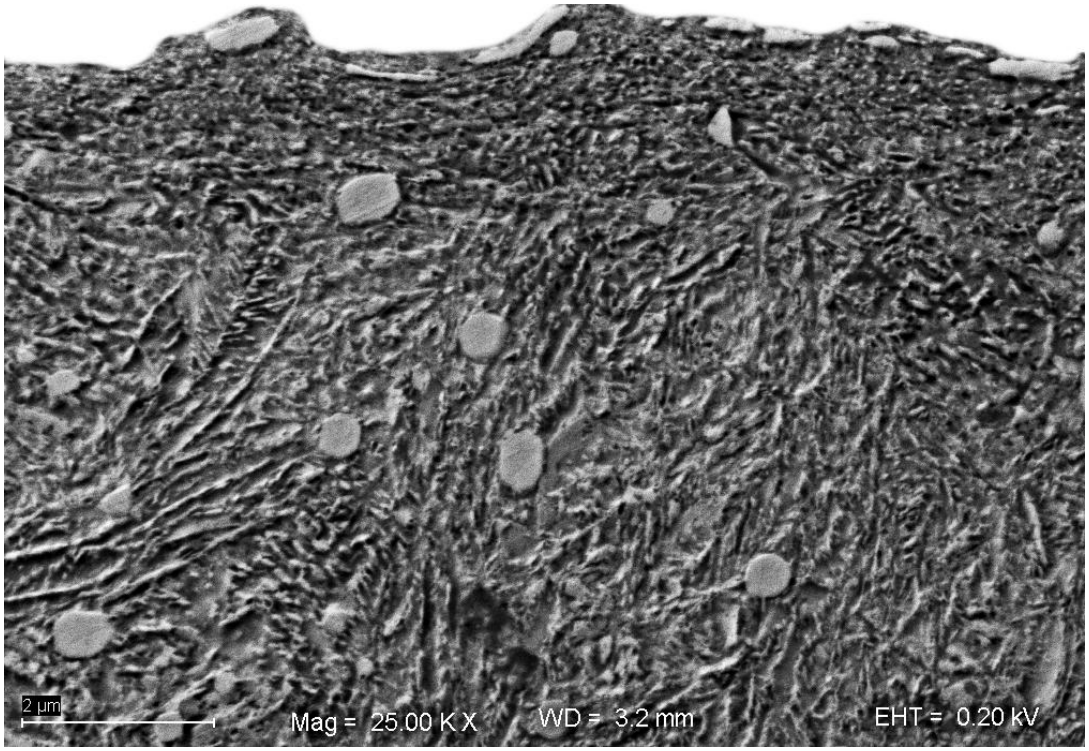

Fig. 19 Examples of elongated carbides near surface, image taken from sample B6.

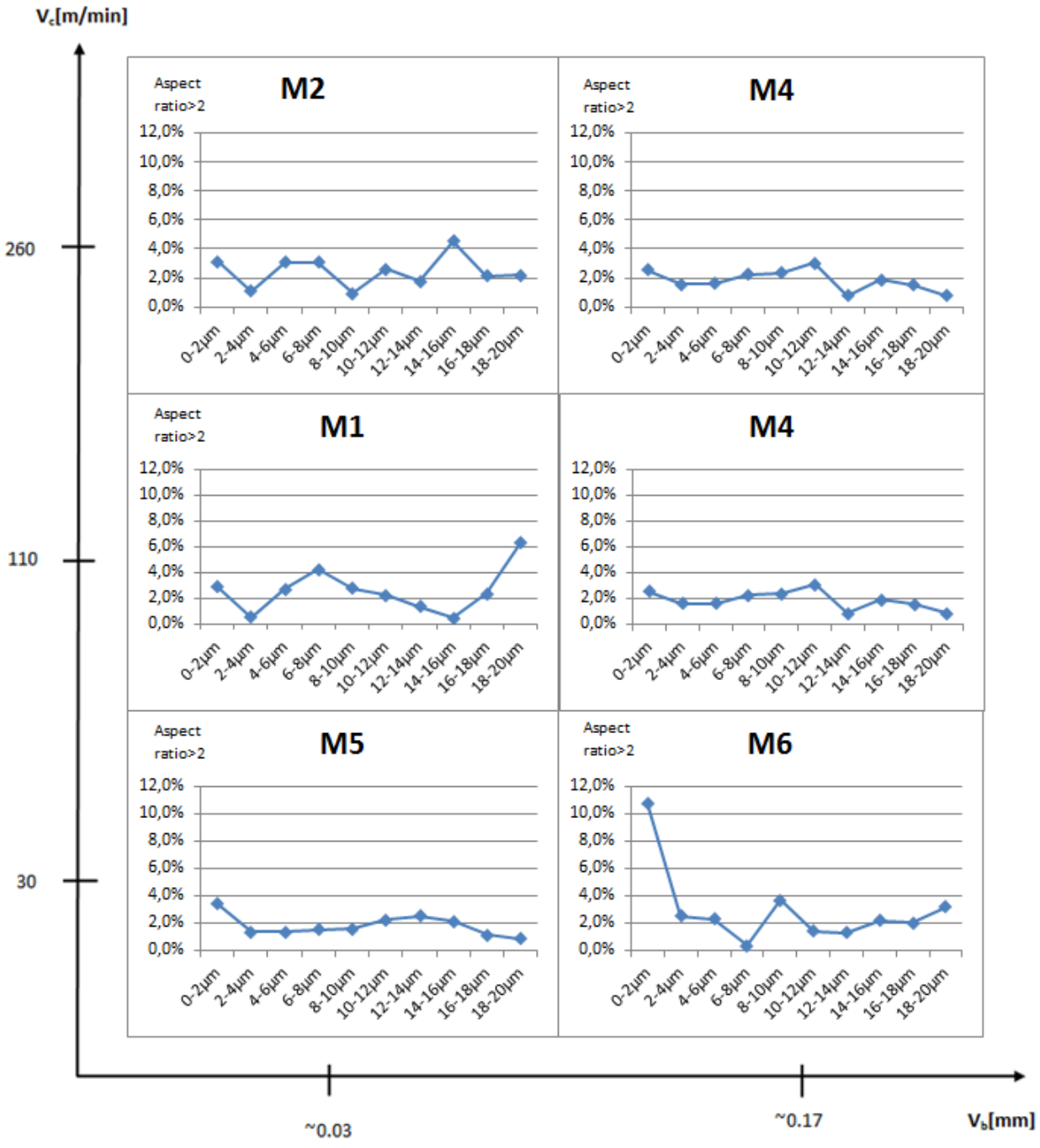

Fig. 20 Percentage of carbides with an aspect ratio>2 as a function of distance from the machined surface for the martensitic samples.

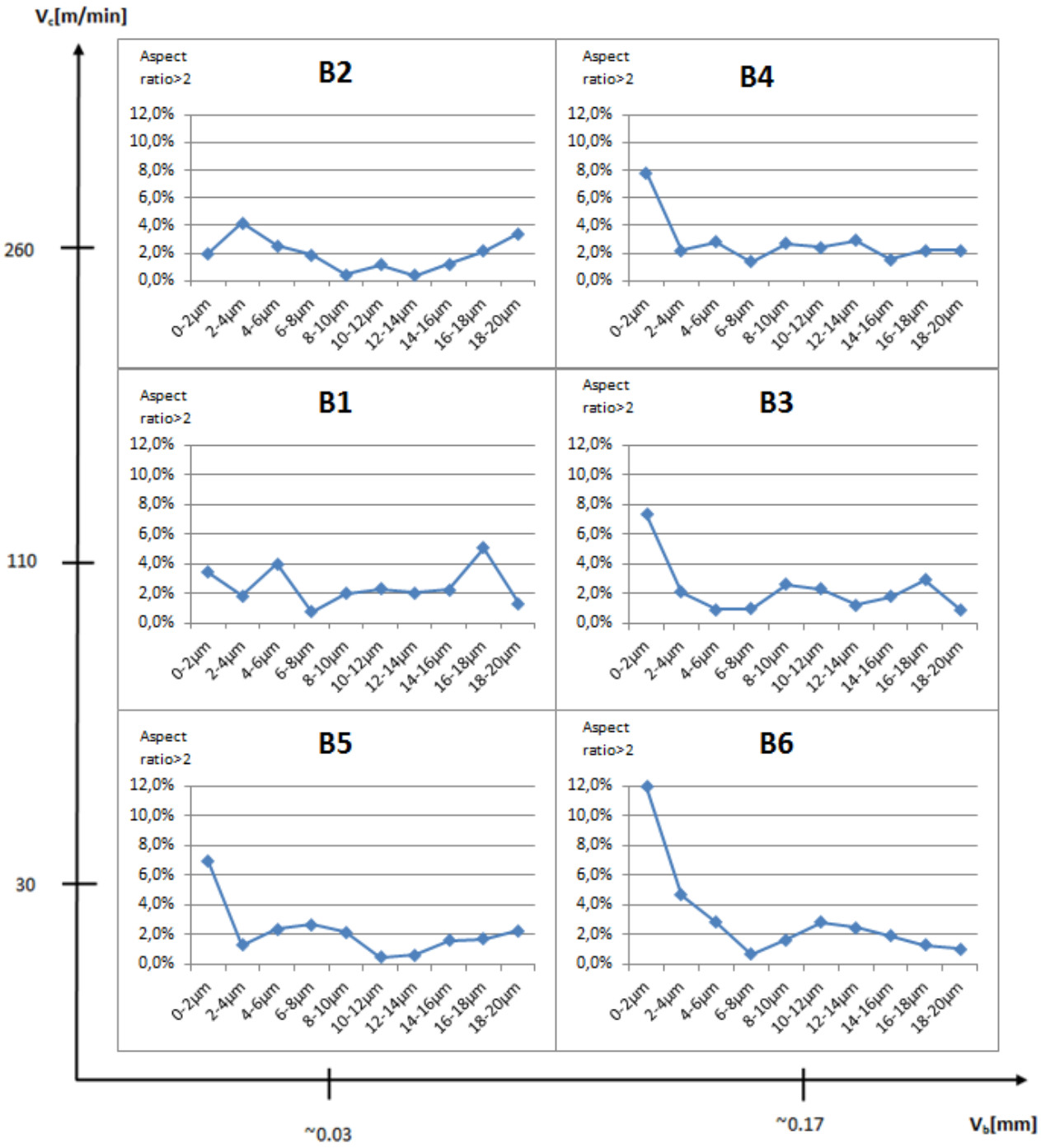

Fig. 21 Percentage of carbides with an aspect ratio>2 as a function of distance from the machined surface for the bainitic samples.

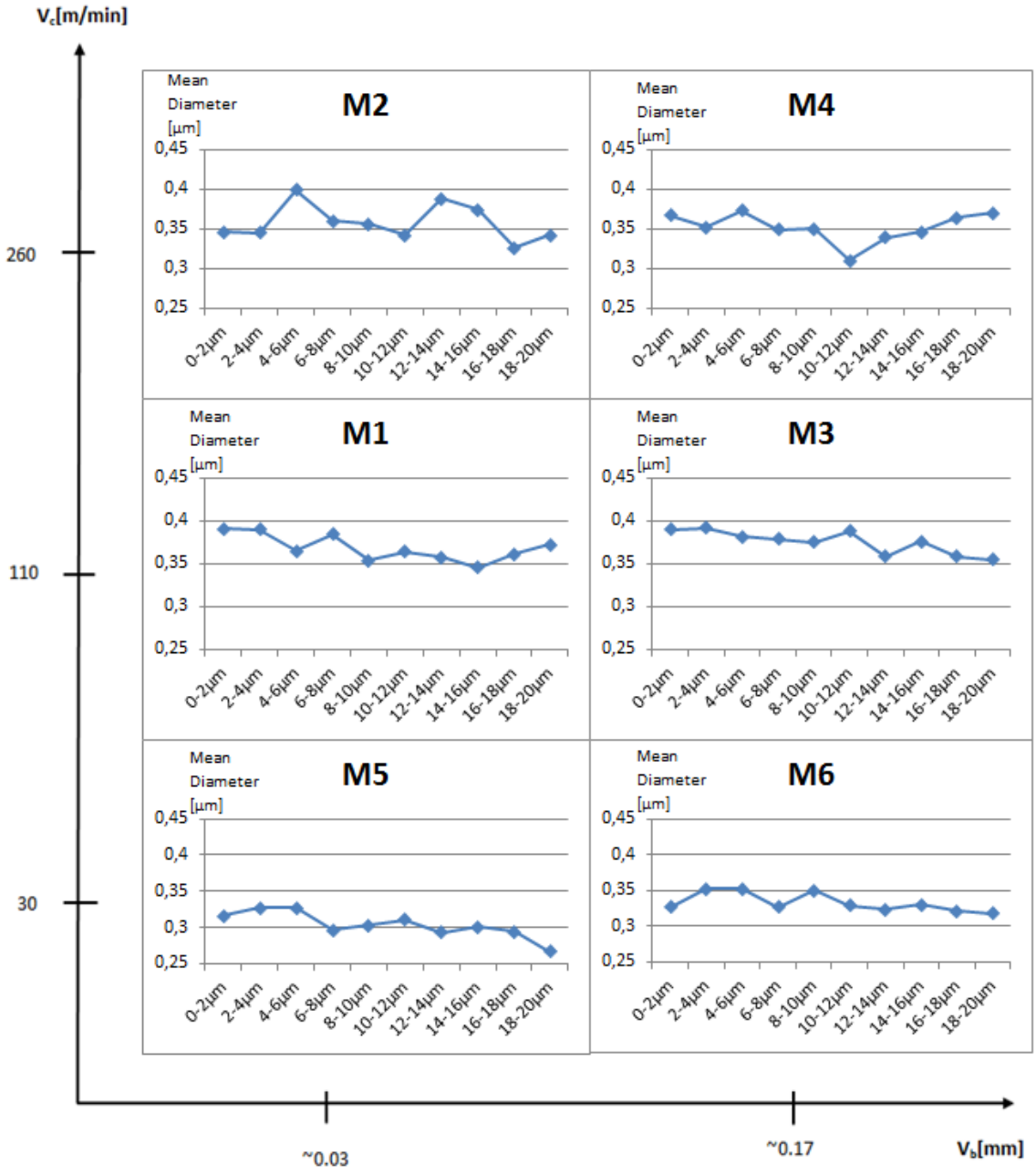

Fig. 22 Mean diameter plotted as a function of distance from the surface for the martensitic samples.

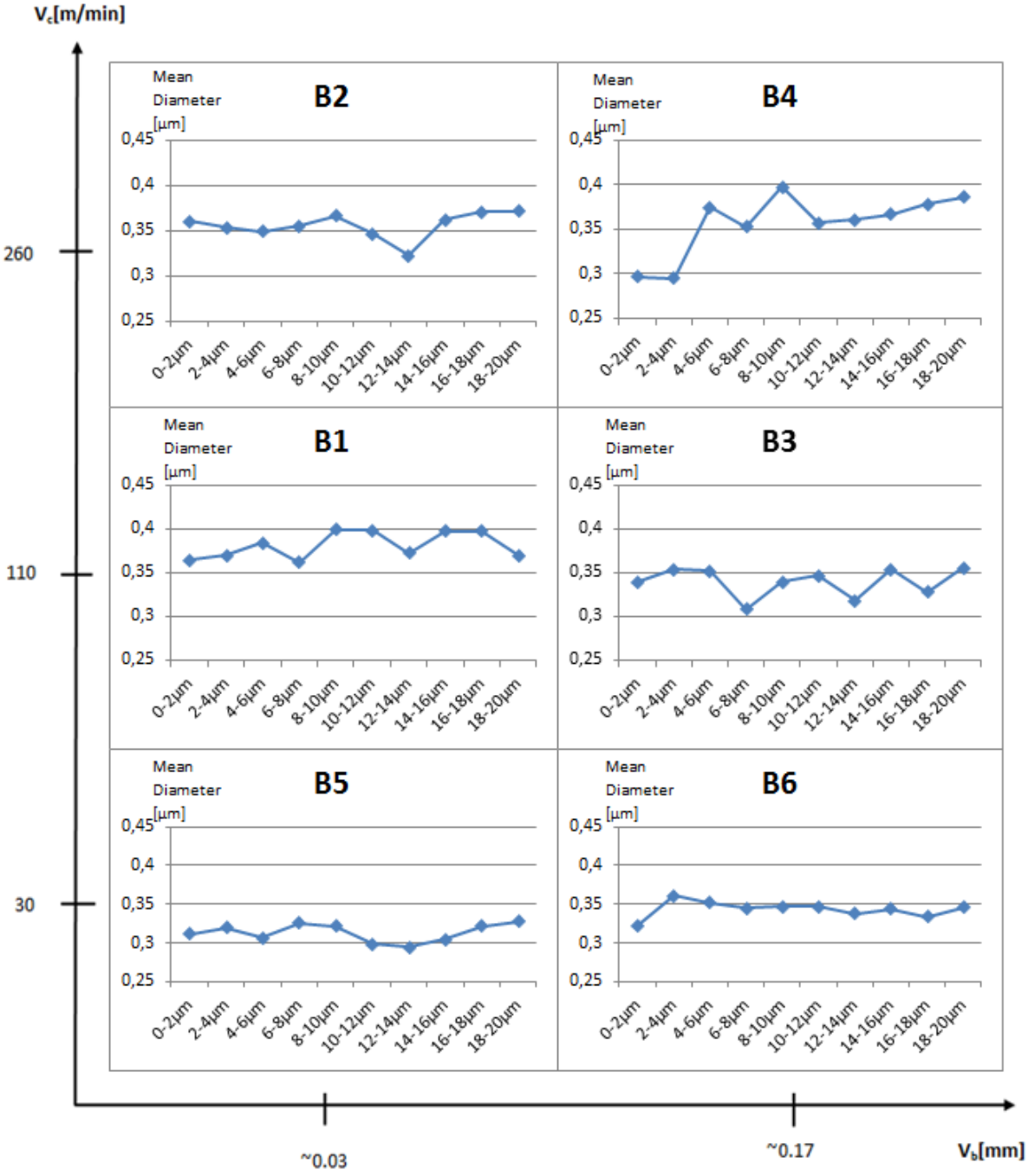

Fig. 23 Mean diameter plotted as a function of distance from the surface for the bainitic samples.

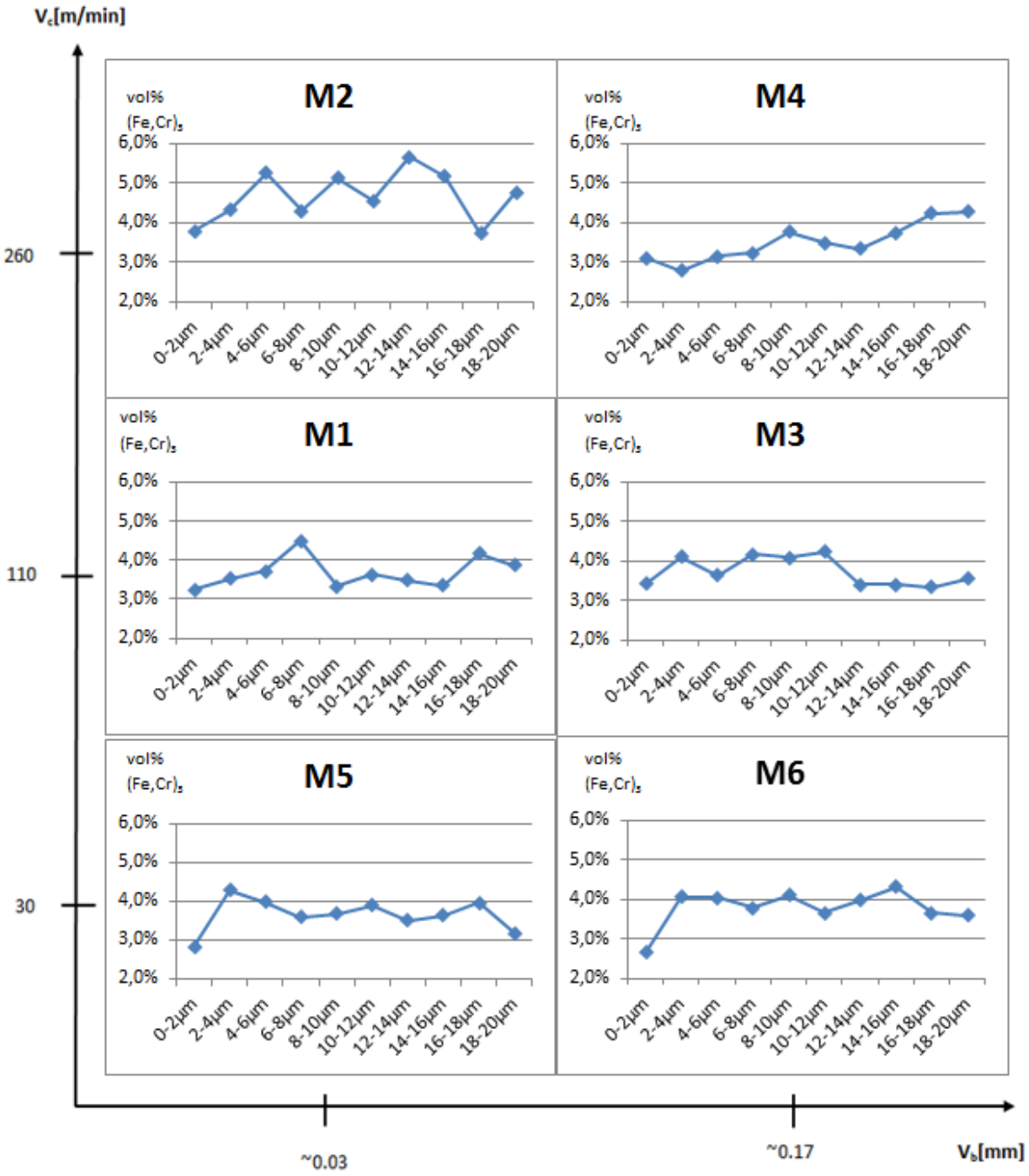

Fig. 24 Volume percentage of carbides as a function of distance from the surface for the martensitic samples.

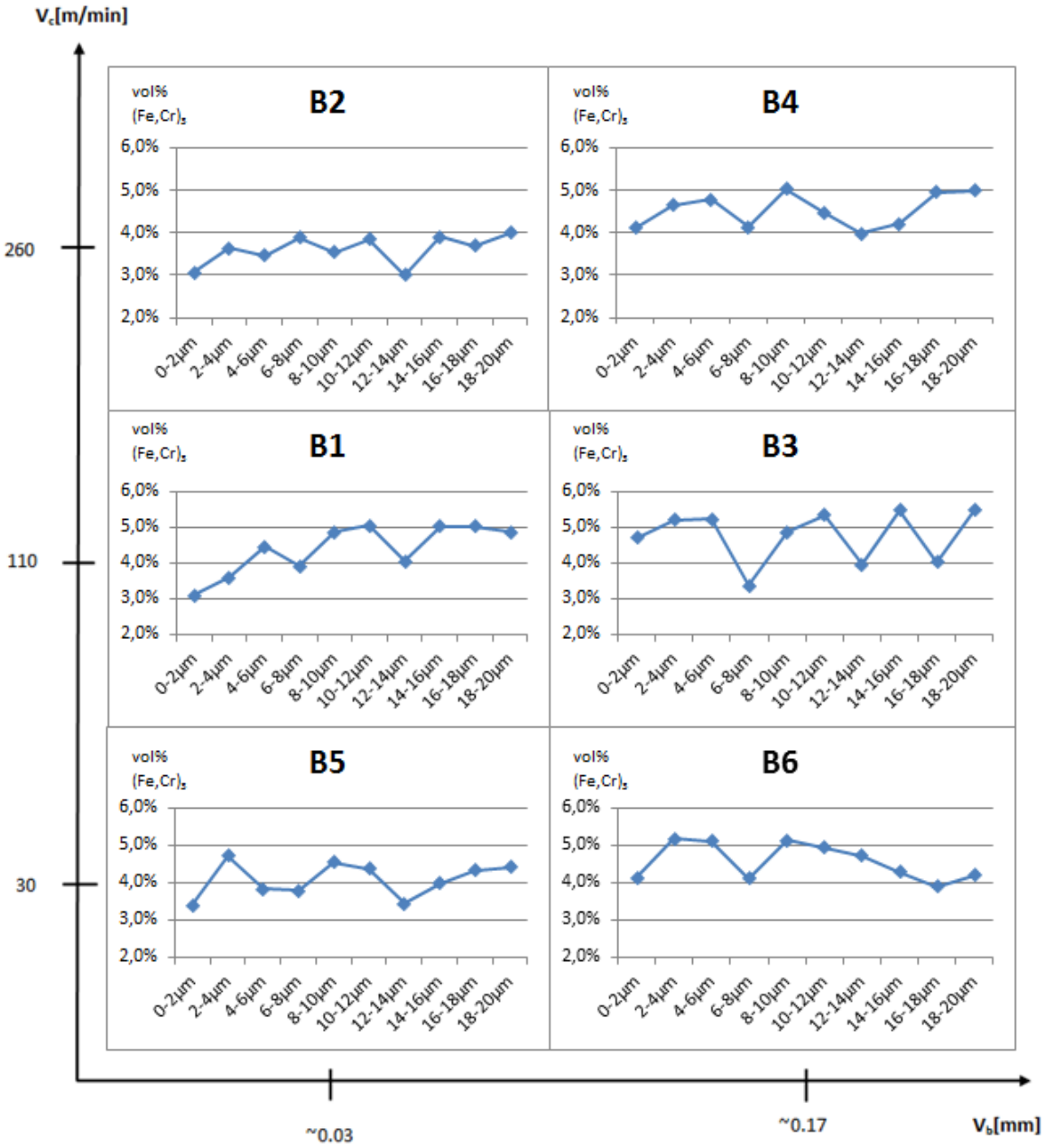

Fig. 25 Volume percentage of carbides as a function of distance from the surface for the bainitic samples.

Due to the temperature values, only three out of six cutting conditions for each material type can be considered during material simulation. Since the calculation of the carbide dissolution or growth starts when the austenization temperature is reached, no difference is made in the base material between bainite and martensite. Here, it is worth keeping in mind that the chemical composition of both microstructures was similar as well as the spherodizing step. The austenitization temperature during heat treatment was also similar for both microstructures resulting in comparable carbide morphology. Therefore the difference in the microstructure prior to the DICTRA simulation is not believed to have a significant role.
During the DICTRA simulation, a number of parameters are to be varied for studying how the carbides are affected and what role the pressure has during simulation of carbide dissolution/growth. The simulations are considering the effect of i) temperature, ii) pressure and iii) temperature and pressure combined. As mentioned earlier, the contact times in hard turning are rather short. Therefore, it is of great importance to study the behavior of the carbides within that time the material experiences an elevated temperature. However, due to the preheating of the workpiece material in hard turning the heating time is multiplied by two in order to consider this effect. For a complete list of the results from the DICTRA simulations see Appendix A. All DICTRA codes are provided in Appendix B.

Generally, the DICTRA simulations indicate an insignificant change in the diameter of the carbides during the short thermal cycles caused by the hard turning. The largest change was recorded for the surfaces machined with the highest cutting speed and highest tool flank wear, where the diameter of the carbides was reduced less than 1nm. However, for the surfaces machined with the highest cutting speed and a new tool the simulations showed that the diameter of the carbide should actually increase. The results from the DICTRA simulation show rather insignificant dissolution of the cementite and the highest loss in carbide diameter was 0.7 nm obtained for parameters related to high cutting speed and worn tool. For high cutting speed and new tool, the simulations show a growth of the carbides. For a summary see Fig. 26.

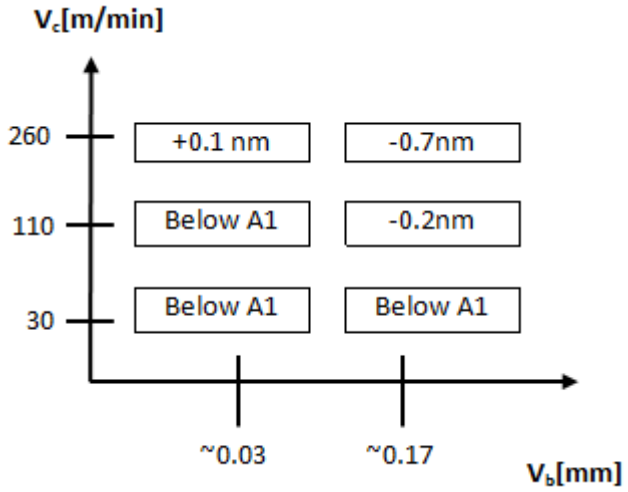

Fig. 26 Change in diameter obtained during simulations. Parameters used: (260/0.03=750°C 1 GPa 20 µs medium carbide); (260/0.17=1000°C 1 GPa 80 µs medium carbide); (110/0.17=900° 1GPa 200 µs medium carbide).

Influence of Pressure

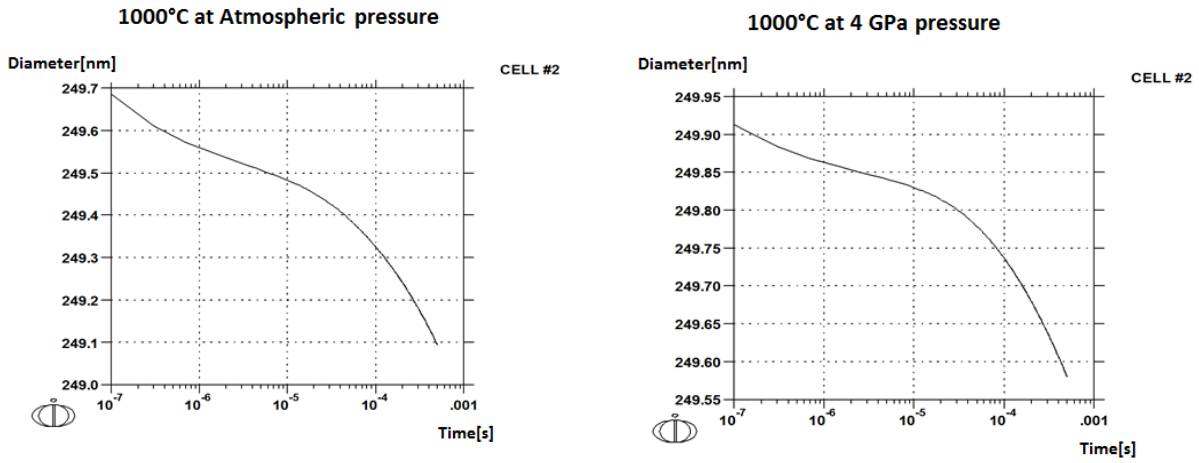

Fig. 27 Diameter change of medium carbide at 1000°C and a) atmospheric pressure and at b) 1GPa

Increased pressure (1-4 GPa) with constant temperature showed a decrease in carbide dissolution. For the case of 1000°C, Fig. 27 a) shows the change in diameter of the medium carbide (Cell#2) to be approx. 1nm after 500 µs while Fig. 27 b) shows clearly that once a pressure of 4 GPa is added, the carbide diameter is reduced by only 0.5 nm after 500 µs. This clearly indicates that the carbide dissolution/change in carbide size is significantly suppressed. The same behavior is noted for all the carbide sizes.

Highest dissolution

During carbide dissolution simulations in DICTRA, the largest dissolution (diameter change) was noted for those surfaces exposed to highest temperatures and atmospheric pressures. The largest reduction in size was recorded for the carbide with largest (500 nm) initial diameter (CELL #1) but the largest change in percent was recorded for the medium carbide with an initial diameter of 250 nm. The change in the carbide diameter is shown in Table 5 and 6.

Carbon and chromium profiles

The chromium profile for the largest carbide exerted to 1000°C and atmospheric pressure shows a buildup (19 wt.% Cr) in the carbide/austenite interface and an enrichment of approx. 1 wt.% Cr in the matrix within an 4 nm radius of the initial interface as shown in Fig. 28 a)

The carbon profile in Fig. 28 b) shows a buildup (0.1 wt.% C) in the interface and an enrichment of 0.1 wt.% C in the matrix within an 2 nm radius of the initial interface.

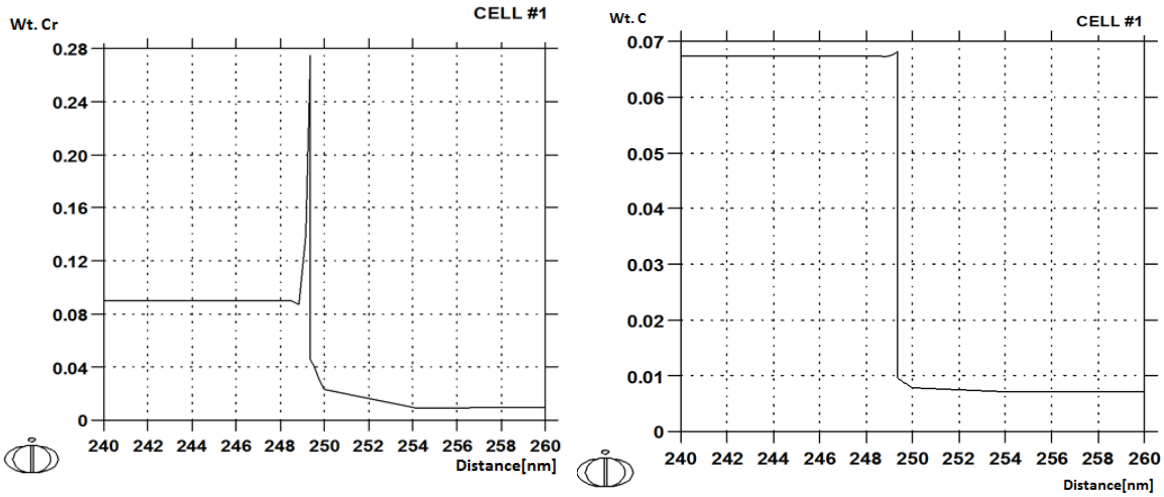

Fig. 28 Chromium a) and Carbon b) concentration plotted versus distance from carbide center after 100 µs.

Influence of initial carbide size

The highest decrease in carbide diameter is found in the largest carbide. The results are summarized in Table 5 and 6.

Table 5 Diametrical change after 500 µs

Initial diameter[nm]	After 500 µs[nm]	Decrease[nm]	Decrease[%]
500	498.8	1.2	0.24%
250	249.1	0.9	0.36%
200	199.2	0.8	0.4%

Table 6 Diametrical change after 100 µs

Initial diameter[nm]	After 100 µs[nm]	Decrease[nm]	Decrease[%]
500	499	1	0.2%
250	249.3	0.7	0.28%
200	199.4	0.6	0.3%

Lowest dissolution

For the simulations resembling the surfaces machined with the highest cutting speed and a new tool where the temperature was estimated to be above the A1-line (T≥750˚C) and the contact pressure was estimated to be in the order of 4 GPa, the simulation showed an increase in the diameter of the carbides. The growth of the medium carbide is shown in Fig. 29.

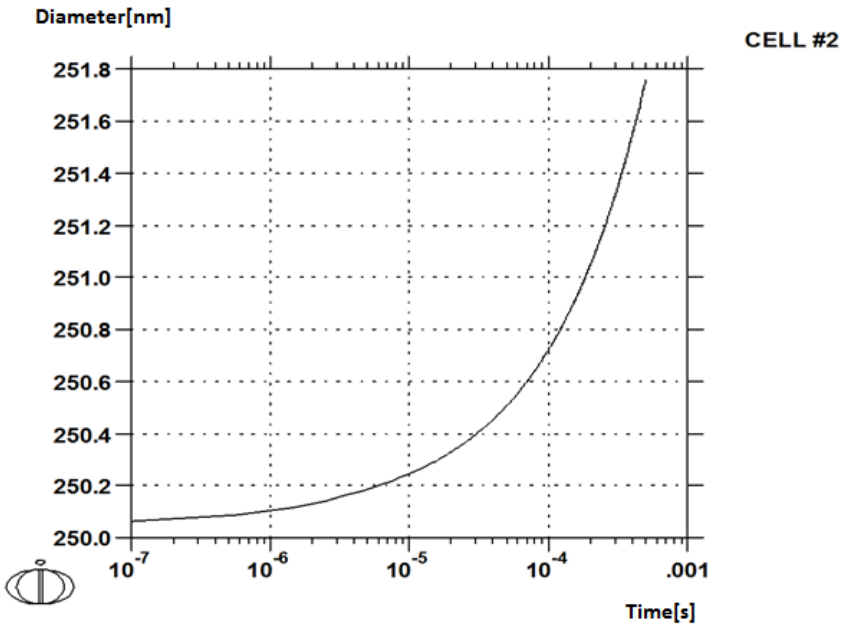

Fig. 29 Change in diameter versus time for medium carbide at 750°C and 4 GPa.

Table 7 Change in diameter after 500 µs

Initial diameter[nm]	After 500 µs[nm]	Increase[nm]	Increase[%]
500	501.61	1.61	0.322%
250	251.78	1.78	0.712%
200	201.75	1.75	0.875%

Table 8 Change in diameter after 100 µs

Initial diameter[nm]	After 100 µs[nm]	Increase[nm]	Increase[%]
500	501.61	1.61	0.322%
250	251.78	1.78	0.712%
200	201.75	1.75	0.875%

Carbon and chromium profiles

As shown in Figs. 30 a) and b), the chromium profile from DICTRA shows a small buildup at the carbide/austenite interface which causes a depletion of chromium in the austenite matrix.

However, the carbon profile does not show any buildup behavior at the interface of the carbide while a small depletion zone of the carbon within the austenite could be found. The depletion of the carbon in the austenite reaches a distance of approx. 4 nm from the initial carbide/austenite interface.

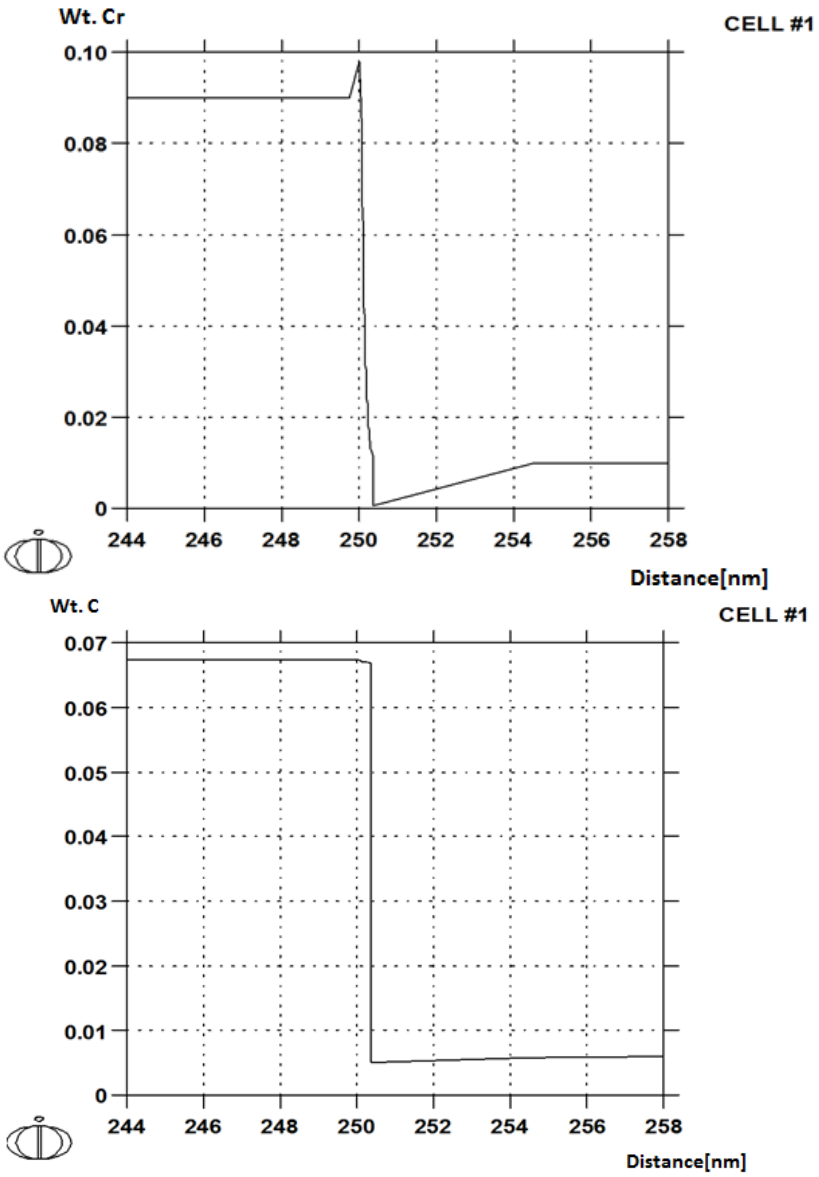

Fig. 30 Chromium a) and carbon b) content plotted versus distance from carbide center after 100µs

CHAPTER 5

Discussion

5.1 SEM

The scanning electron microscopy investigation of the M_3C carbides of the SAE 52100 through-hardened steels after hard turning revealed that there was no significant difference in the mean carbide diameter near the surface compared to the bulk material. The deviation in volume fraction is within the measurement error [25] in all cases except for the martensitic surfaces machined with the lowest cutting speed where a lower volume fraction of carbides in the top layer is found. This indicates that the carbide dissolution in these cases is not controlled by temperature since the surface temperature for these samples was well below the A_1-line. Therefore, other mechanisms must take place at the surface during machining with low cutting speed (30 m/min). Carbide refinement due to mechanical work is a possible mechanism which has been suggested by Turley [14]. This is also supported by the fact that elongated carbides were found near the surface in samples machined with low cutting speed (M5/B5 and M6/B6). The reason why the lower volume fraction is only observed in the martensitic samples and not in the bainitic is not clear. However, as shown by Hosseini et al [22], there is also a difference in the amount of retained austenite at the surface after hard turning of bainitic and martensitic materials. Generally, the martensitic surfaces containing white layer had higher volume fraction of retained austenite compared to bainitic samples machined with similar cutting conditions implying that the two microstructures react differently to the hard turning process.

5.1.1Source of errors

There have been a number of factors that can have an impact on the results during carbide analyses such as the etching procedure, SEM-analyses and finally the quantification of the carbides in the software AxioVision.

Etching can affect the results by a misrepresentation of the microstructure. By etching the matrix to reveal the carbides, matrix material is removed which favors the carbide volume leading to a possible overestimation of the volume fraction of carbides [25].
However, since this study is more concerned with registering trends within the surface layer than to determine true volume fractions, an overestimation of the volume fraction of the carbides can be tolerated since same errors will apply to all the samples.

The same etching method (OP-S for 30 min) was used for both martensitic and bainitic microstructures. The etching method worked very well for the bainitic samples but not fully as satisfying for the martensitic samples and perhaps a modification of the etching procedure for the martensitic would render better results.

There is a possibility that those carbides which were slightly larger than 100 nm have been affected to the extent that they after hard turning had a diameter less than 100 nm and thereby they have not

been considered in the analyses. Despite the high magnification selected for the SEM studies, carbides less than 100 nm where not easily observed.

As described earlier the auto-detect (auto-measure) function in the image analysis software (AxioVision Version 4.8.2.0) could not be applied as the contrast difference between the matrix and the carbides was too low. Therefore, all images were processed manually which can affect the final results.

During hard turning, the surfaces will have a certain roughness which will have an influence on the SEM images and thereby on the final results regarding the volume fraction of the carbides the first 2 µm. An example is given in Fig. 31.

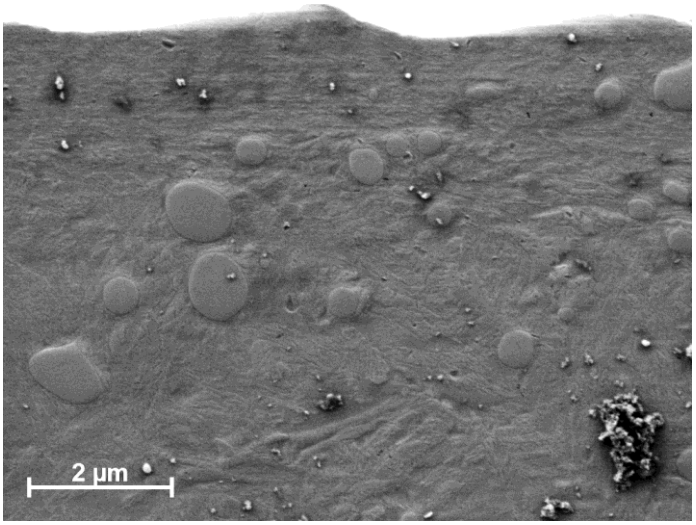

Fig. 31 Example of rough surface which can affect the volume fraction calculation.

5.2 DICTRA

The very low dissolution values received from the DICTRA calculations suggest that thermal and pressure based diffusion kinetics is not sufficient to describe the differences seen in the SEM-analyses. The plastic deformation induced during hard turning may increase the carbide dissolution rate by shearing of the austenitic phase as well as it may introduce defects and vacancies which can act as high-diffusivity paths [8]. The DICTRA software can treat this as well, but that requires additional investigation of the material which was not possible during this study. Furthermore, the mechanism proposed by Turley [14] for the refinement of carbides is also not considered in the model, which can be another factor playing an important role in describing the mechanisms of carbide dissolution.

Besides the temperature effect, the pressure added in the DICTRA simulations showed a decrease in dissolution of the carbides. When studying the ternary phase diagram for Fe-Cr-C, the A_1-temperature line is lowered while the A_3-temperature line is increased when the pressure is increased. The pressure influence on the A_3-line is more significant than the influence on the A_1-line, resulting in a stabilization of the cementite-carbides.

The carbon and chromium profiles for the high cutting speed and worn tool showed that the short process time of hard turning is sufficient to build up a deposit of chromium at the interface (although very thin) which could only allow a short diffusion distance of not more than 4 nm into the matrix. Considering the results from DICTRA, the carbide dissolution seems to be controlled by the diffusion of chromium in the austenitic matrix.

The simulation results from DICTRA simulations showed that the largest carbides had a higher dissolution rate for larger carbides compared to the smaller ones, implying that the dissolution rate is controlled by the larger carbides. Prior to the final simulations some test simulations were performed with single carbides. They showed a higher rate of dissolution than the cell model containing three carbides suggesting that the system of carbides in our case stabilizes each other and reduces the dissolution rate. In all simulations the three carbides either all grew or dissolved. None of the simulations showed carbide shrinkage on expense of a growing carbide.

Simulations representing high cutting speed with new tool (B2/M2) showed carbide coarsening. This was not expected but can be explained by widening of the field between the A_1 and A_3-line (Fig. 32) stabilizing the carbides and even promoting their growth. The carbon and chromium profile for this cutting condition shows that both chromium and carbon diffuses into the carbide leaving the surrounded matrix depleted.

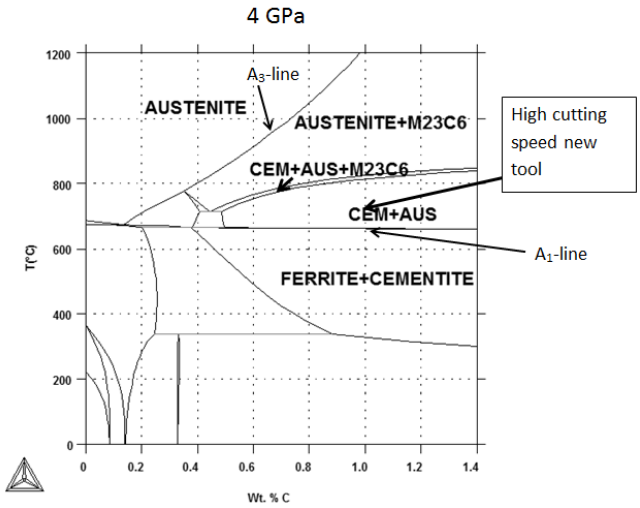

Fig. 32 Phase diagram showing the position of the cutting condition of high cutting speed and new tool.

CHAPTER 6

Conclusion

When investigating what effect hard turning has on the carbides it is evident that not only one parameter such as carbide mean diameter is sufficient, instead a combination of several parameters is needed to give a full picture:

- According to the DICTRA-simulations no significant dissolution of the carbides will occur during the short process time of hard turning when only considering pressure and temperature.

- Elongated carbides are observed in the samples with low cutting speed and worn tool. These are believed to have been deformed during the hard turning process.

- The SEM-analysis shows a limited dissolution of carbides in the martensitic surfaces machined with low cutting speed.

- According to DICTRA-simulations, an applied pressure seems to stabilize the carbides and to lower the dissolution rate.

CHAPTER 7

Future work & Recommendations

To be able to do more accurate simulations and to evaluate the results, more information about the chemical composition of the carbides and the carbon and chromium profiles are needed both before and after hard turning. This could be done by the means of STEM.

Also, to be able to refine the simulation model by introducing effects from the plastic deformation such as shearing of the austenitic phase and increased diffusivity along defects and vacancies, information about the dislocation density in both the studied microstructures is needed.

References

[1] B.J Griffiths, "White layer formation at machined surfaces and their relationship to white layer formation at worn surfaces", J. Tribol 107, pp. 165-170,1985

[2] G. Poulachon *et al.,* "An experimental investigation of work material microstructure effects on white layer formation in PCBN hard turning" ,*International Journal of Machine Tools & Manufacture 45,* pp. 211–218, 2005.

[3] B. Zhang, W. Shen, Y. Liu, X. Tang, Y. Wang, "Microstructures of surface white layer and internal white adiabatic shear band" *Wear 211*, pp. 164-168, 1997.

[4] Cho *et al*, "Adiabatic shear band formation during dynamic torsional deformation of an HY-100 steel", *Acta metal. Mater.,* Vol. 41, No. 3, pp.923-932, 1993.

[5] C.O. Mybokwere, S.R. Nutt, J. Duffy, "Shear band formation in 4340 steel: A TEM study", *Mech. Mater. 17*, pp. 97–110, 1994.

[6] X. Sauvage a, J.M. Le Breton , A. Guillet , A. Meyer, J. Teillet "Phase transformations in surface layers of machined steels investigated by X-ray diffraction and Mössbauer spectrometry" Materials Science and Engineering A362, pp.181–186, 2003.

[7] Y.K. Chou, C.J. Evans, "White layers and thermal modeling of hard turned surfaces", *Int. J. Mach. Tools Manufact. 39*, pp. 1863–1881, 1999.

[8] J. Barry, G. Byrne, "TEM study on the surface white layer in two turned hardened steels", *J. Mater. Sci. Eng. A325,* pp.356–364, 2002.

[9] J.C. Jaeger, "Moving sources of heat and the temperature of sliding contacts", *J. Proc. R. Soc,* NSW 76, pp.203–224, 1943.

[10] H.K.D.H Bhadeshia, R.W.K Honeycombe, "Steels- Microstructure and properties", 2006

[11] J.M. Beswick, "The Effect of Chromium in High Carbon Bearing Steels".

[12] Frank V. Nolfi, Jr., Paul G. Shewmon, James S. Foster, "The Dissolution Kinetics of Fe_3C in Ferrite", *Metallurgical and Materials Transactions B Volume, 1 Number 4*, pp. 789-800, 1970.

[13] Z. Zurecki, R. Ghosh, J.H. Frey, "Investigation of white layers formed in conventional and cryogenic hard turning steels", *ASME International Mechanical Engineering Congress and Exposition, Washington, DC, USA, IMECE Proceedings, November vol. xx,* pp. 16–21, 2003.

[14] D.M. Turley, Mater. Sci. Eng. 19, pp. 79-86, 1975.

[15] W. Grzesik, "Advanced machining processes of metallic materials: theory, modelling and applications", 2008.

[16] K. Philip Varghese "Machining of Compacted Graphite Iron (CGI) and Spheroidal Graphite Iron (SGI): A fundamental study of tribological issues and progressive cutting tool wear", Doctoral Thesis/Dissertation, 2008.

[17] N.A. Abukhshim, P.T. Mativenga, M.A. Sheikh Heat generation and temperature prediction in metal cutting: A review and implications for high speed machining, *International Journal of Machine Tools and Manufacture Volume 46, Issues 7–8,* pp. 782–800*,* 2006.

[18] L. Onsager, *Phys. Rev* , Vol. 37, pp. 405-26; 1931, and Vol. 38, pp. 2265-79, 1931.

[19] A. Borgenstam, A. Engström, L. Höglund, and J. Ågren: "DICTRA, A Tool for Simulation of Diffusional Transformations in Alloys", *J. Phase Equilibria*, *21*(3), pp. 269–80, 2000.

[20] L. Kaufman and H. Bernstein, "Computer Calculations of Phase Diagrams", 1970.

[21] J.-O. Andersson, J. Ågren, "Models for Numerical Treatment of Multicomponent Diffusion in Simple Phases", *J. Appl. Phys, Vol.72*, pp. 1350-55, 1992.

[22] J. Ågren, *Iron Steel Inst. Jpn. Int.*, Vol 32, pp. 291-96,1992.

[23] Z.-L. Liu, L. Höglund, B. Jönsson, and J. Ågren,"An Experimental and Theoretical Study of Cementite Dissolution in an Fe-Cr-C Alloy", *Metall. Trans. A*, 1991, Vol. 22A, pp. 1745-52, 1991.

[24] S.B. Hosseini, K. Ryttberg, J.Kaminski, U.Klement, " Characterization of the Surface Integrity by Hard Turning of Bainitic and Martensitic AISI 52100 Steel", 2012.

[25] Patrik Ölund "Etching technique to determine the true volume fraction of cementite in through hardening hardening ball bearing steel" Technical report TBL 119/96, 1996.

Appendix A

750°C 1 atm

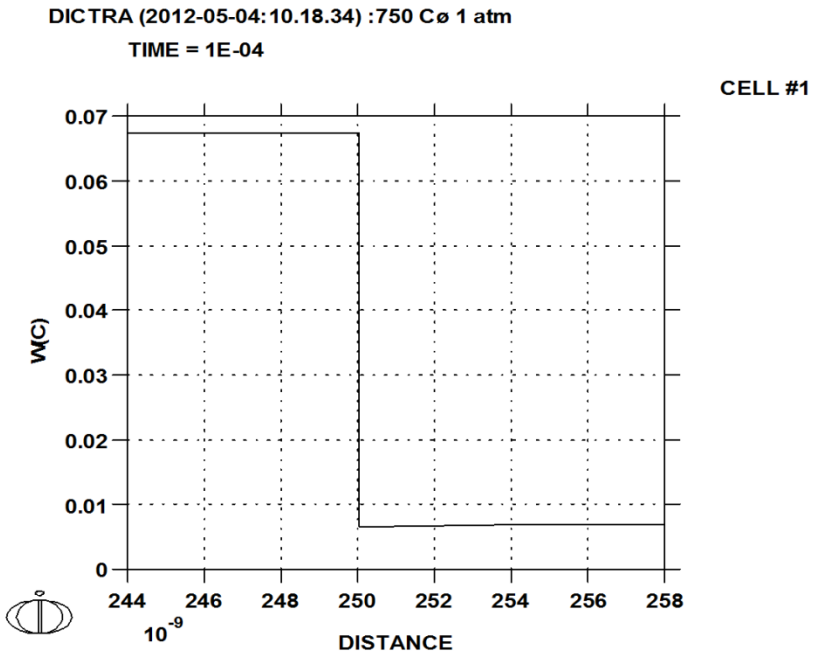

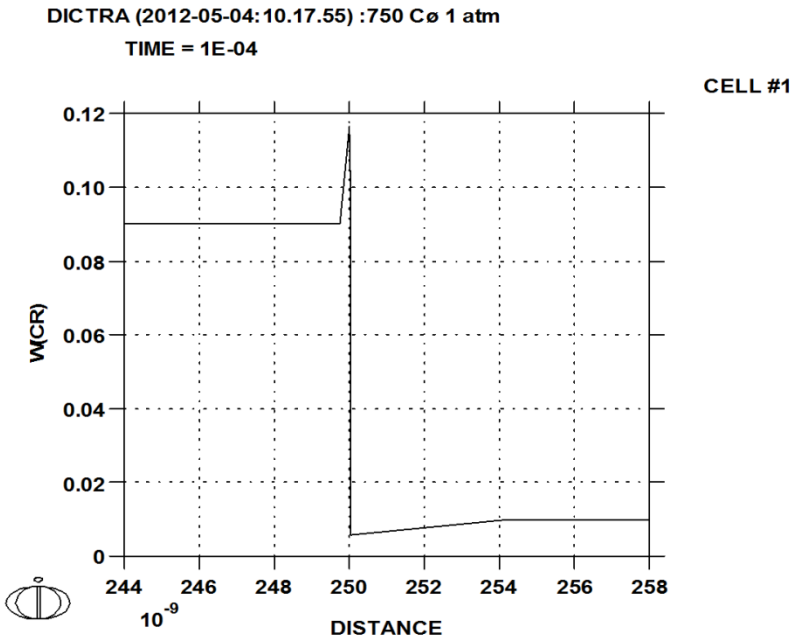

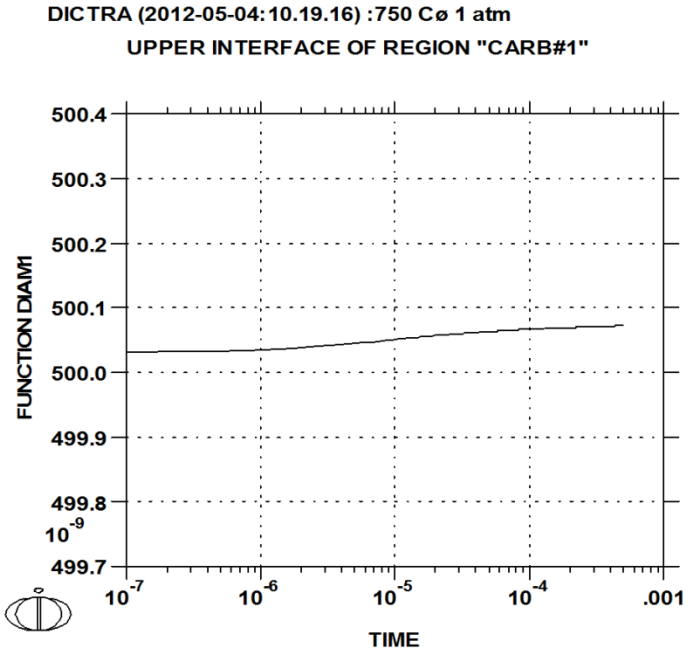
DICTRA (2012-05-04:10.19.16) :750 Cø 1 atm
UPPER INTERFACE OF REGION "CARB#1"
CELL #1
500.4
500.3
500.2
500.1
500.0
499.9
499.8
10-9
499.7
FUNCTION DIAM1
10-7
10-6
10-5
10-4
.001
TIME
2012-05-04 10:19:16.31 output by user rictahlq from MATM40

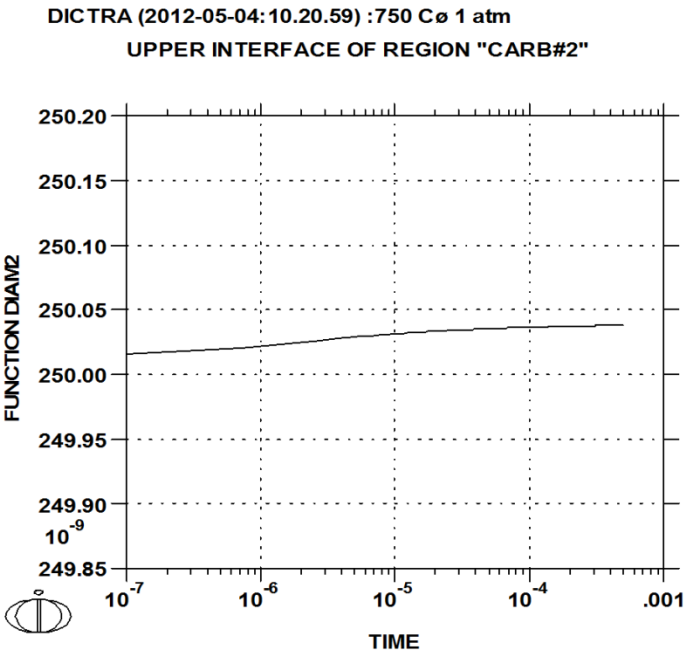
DICTRA (2012-05-04:10.20.59) :750 Cø 1 atm
UPPER INTERFACE OF REGION "CARB#2"
CELL #2
250.20
250.15
250.10
250.05
250.00
249.95
249.90
10-9
249.85
FUNCTION DIAM2
10-7
10-6
10-5
10-4
.001
TIME
2012-05-04 10:20:59.77 output by user rictahlq from MATM40

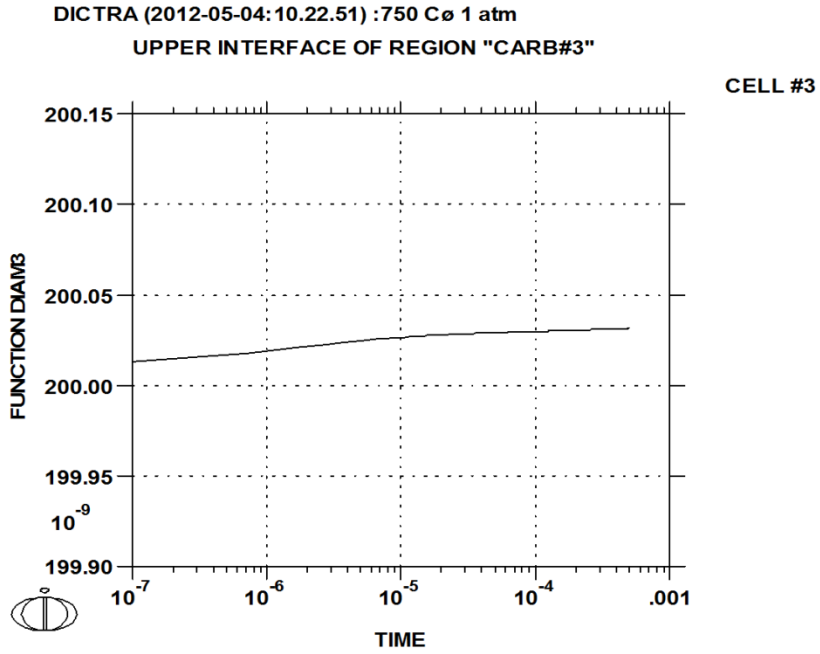

750°C 1 GPa

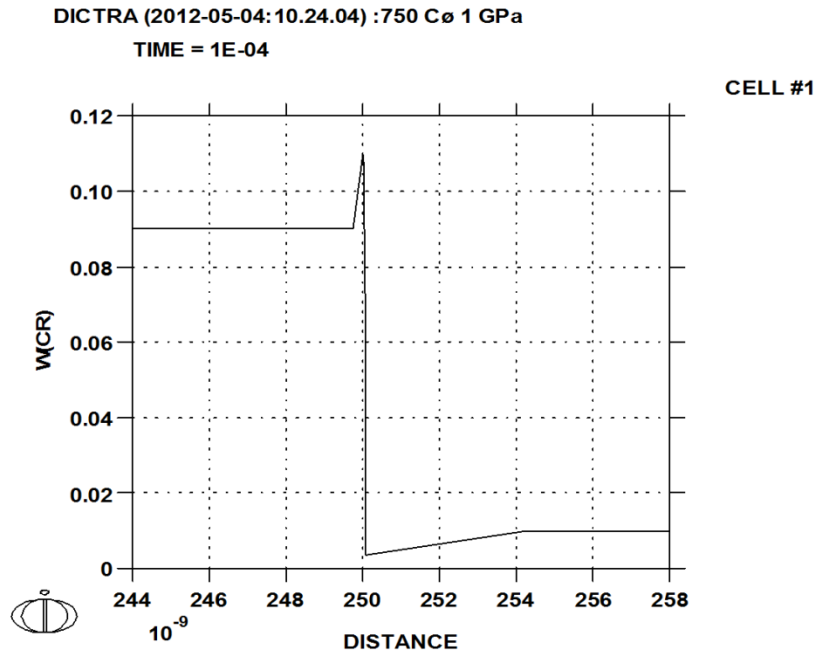

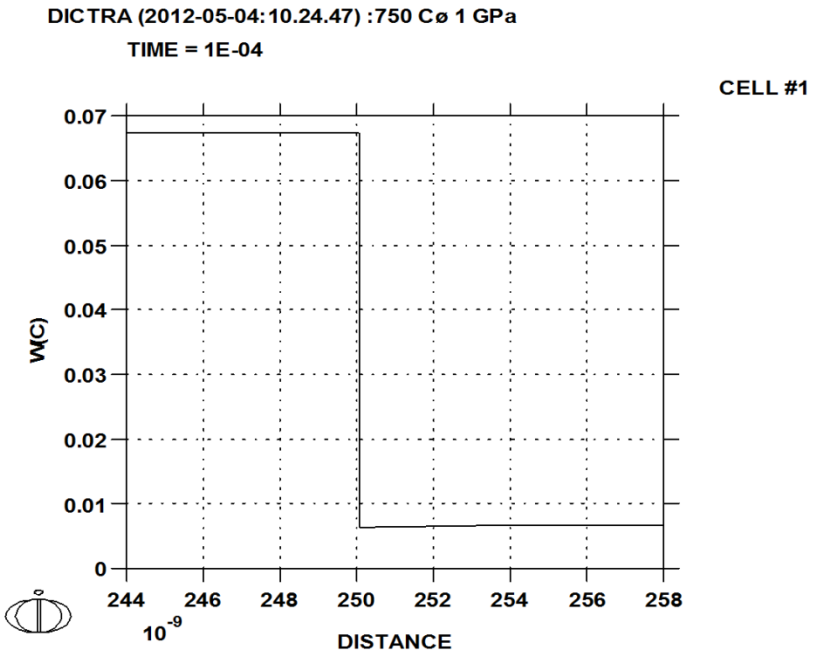

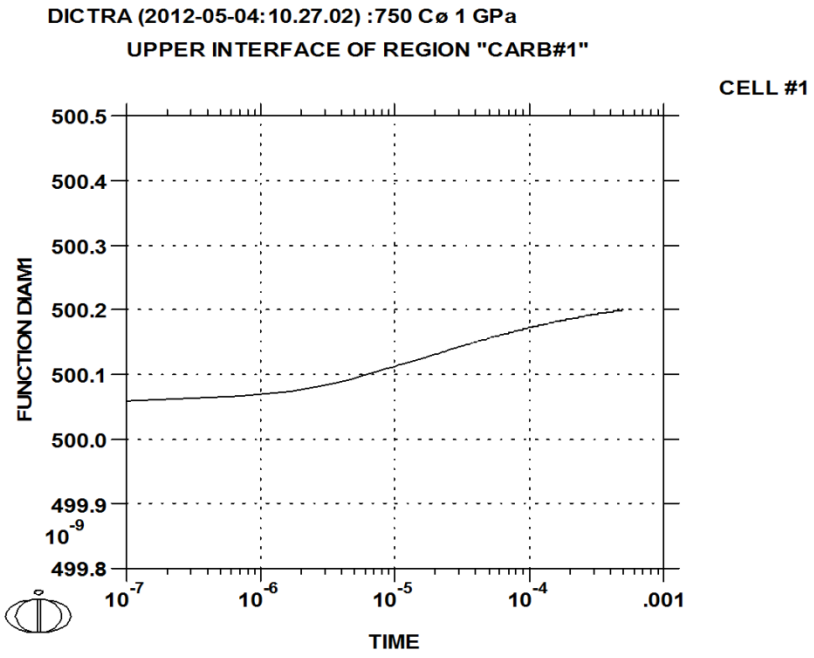

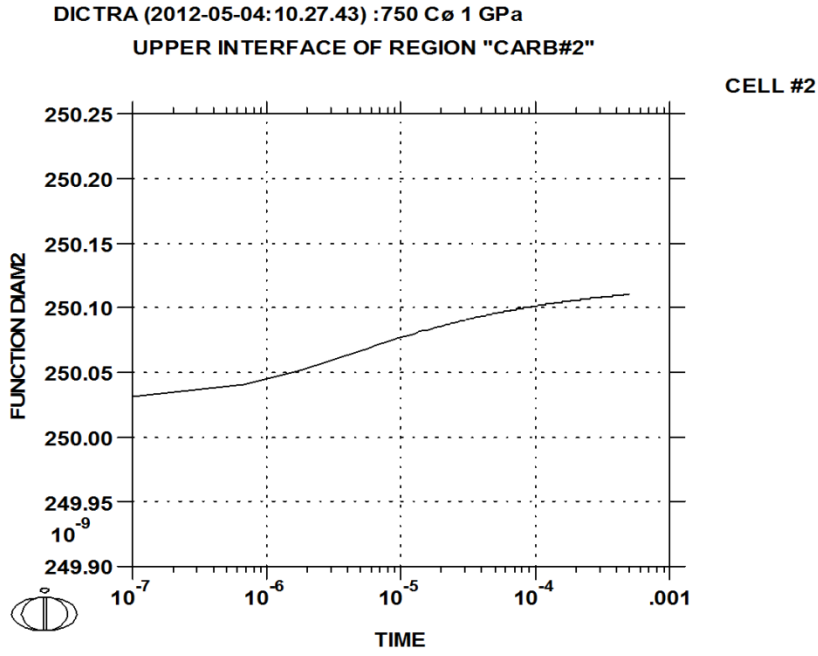

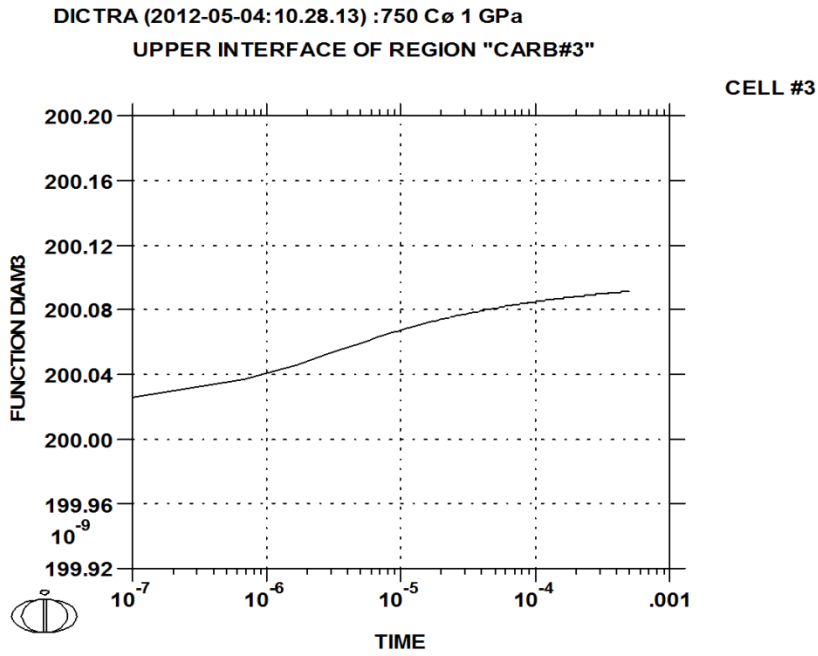

750°C 4 GPa

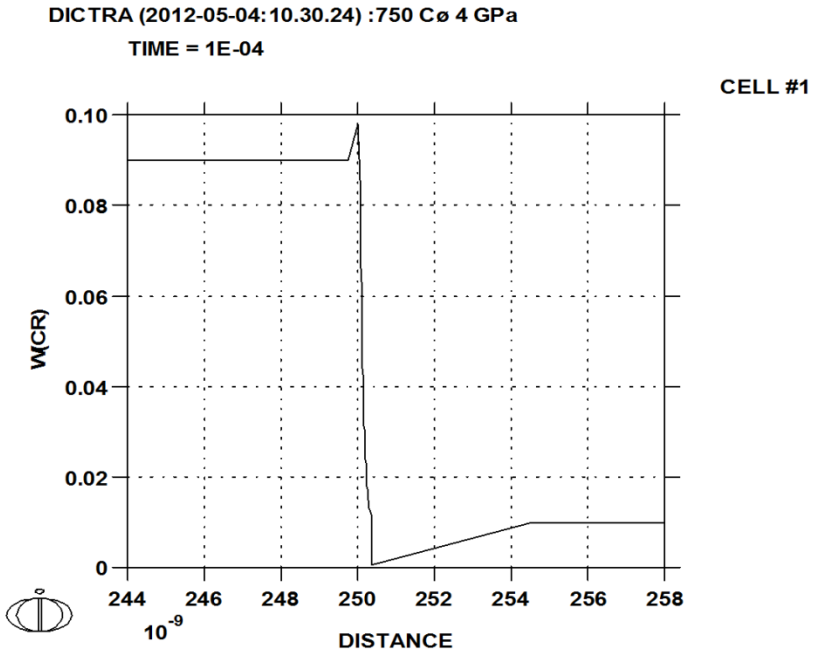

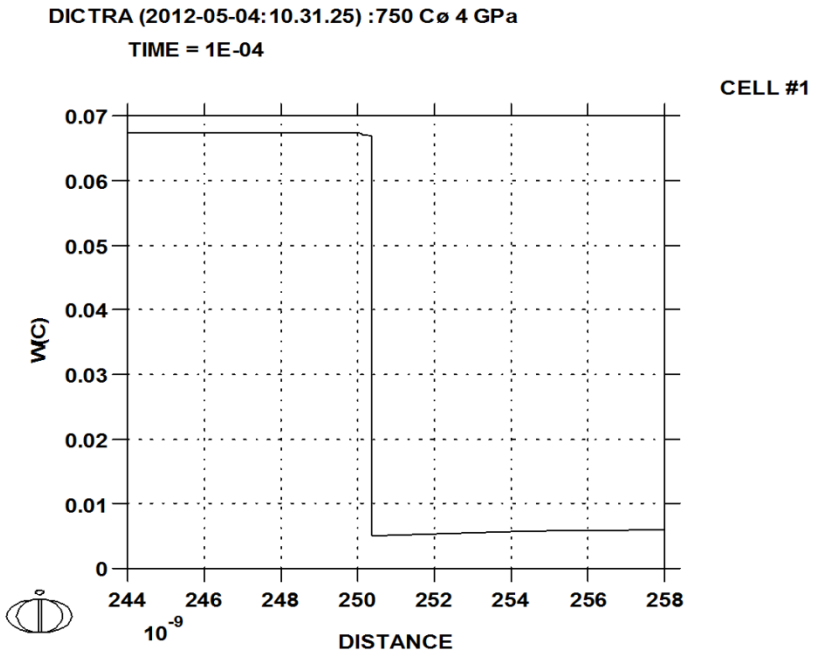

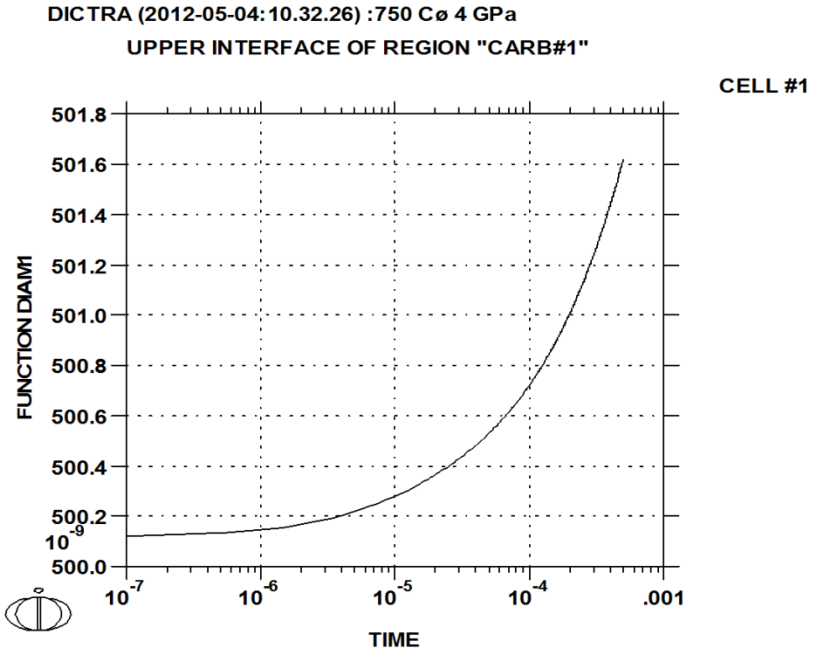

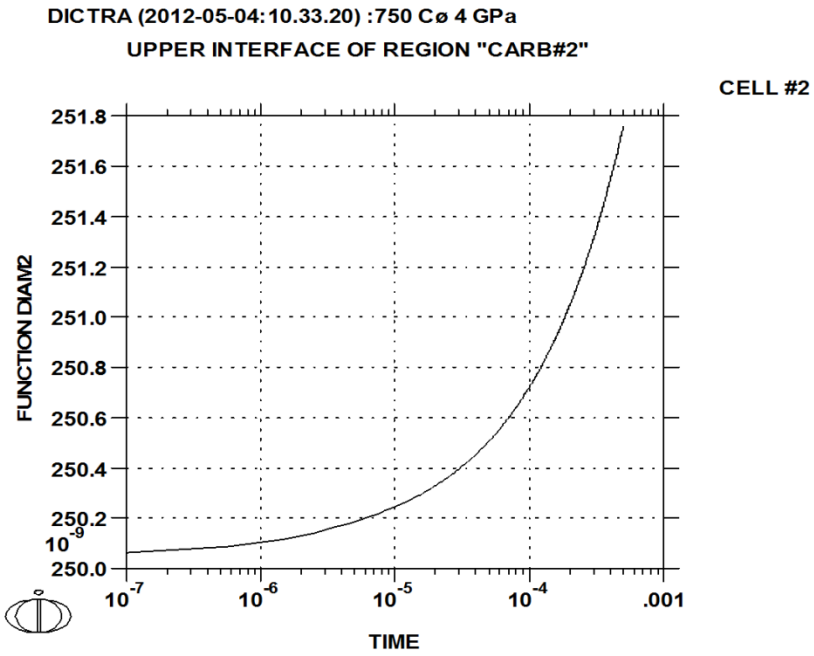

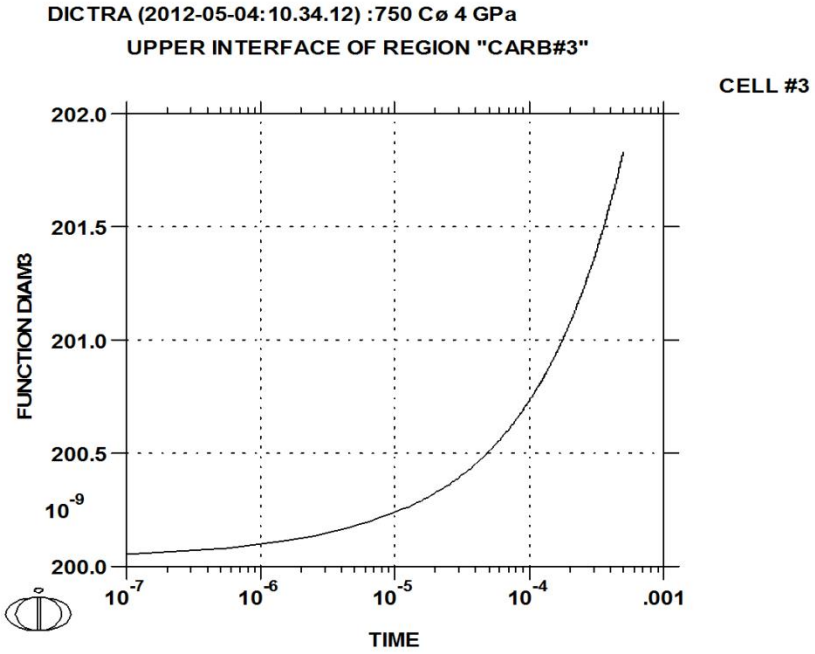

800°C 1 GPa

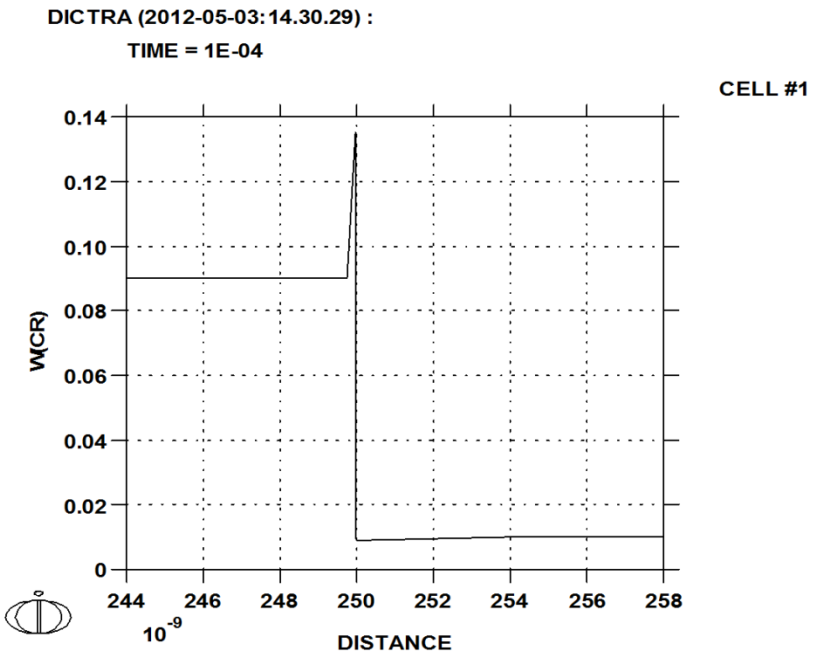

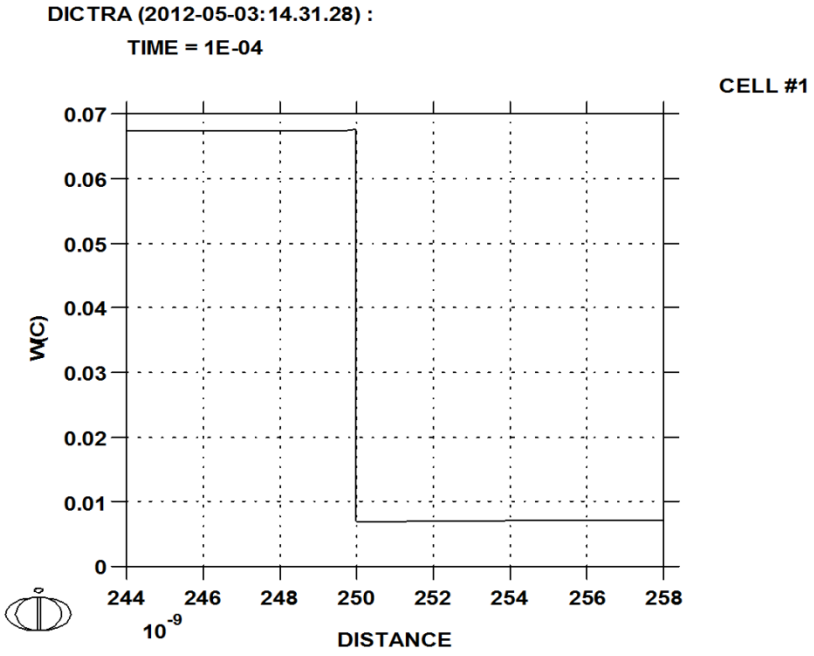

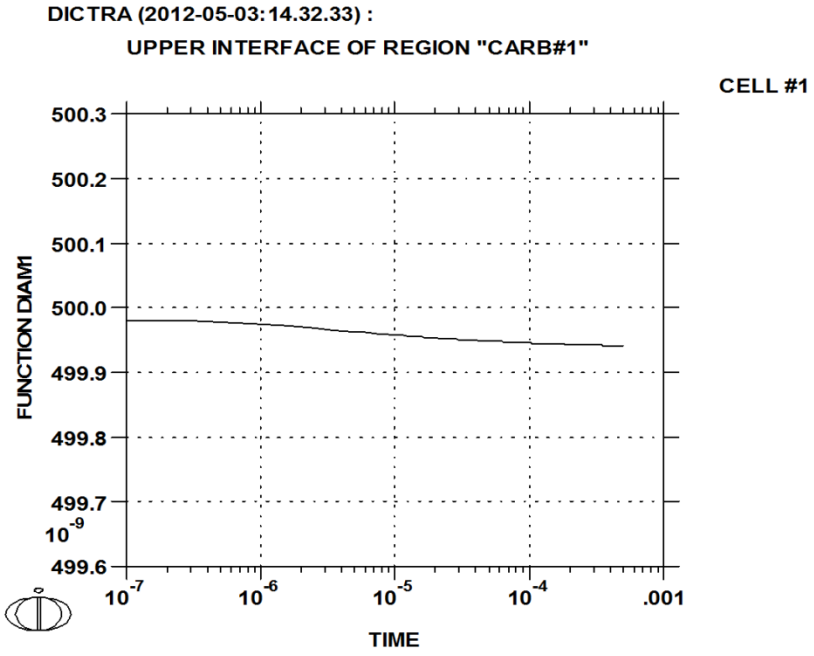

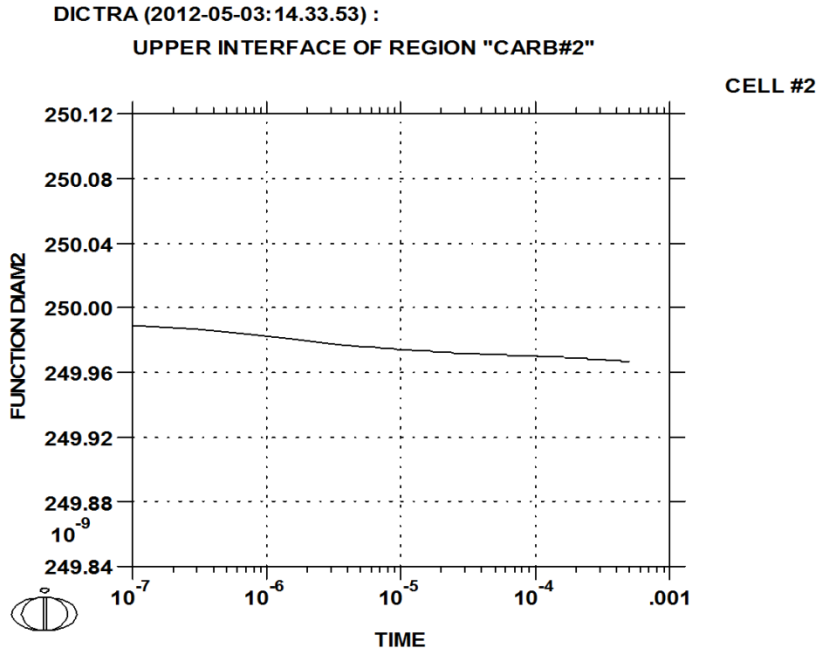
DICTRA (2012-05-03:14.33.53) :
UPPER INTERFACE OF REGION "CARB#2"
CELL #2
250.12
250.08
250.04
250.00
249.96
249.92
249.88
249.84
FUNCTION DIAM2
10-9
10-7
10-6
10-5
10-4
.001
TIME
2012-05-03 14:33:53.02 output by user rictahlg from MATH40

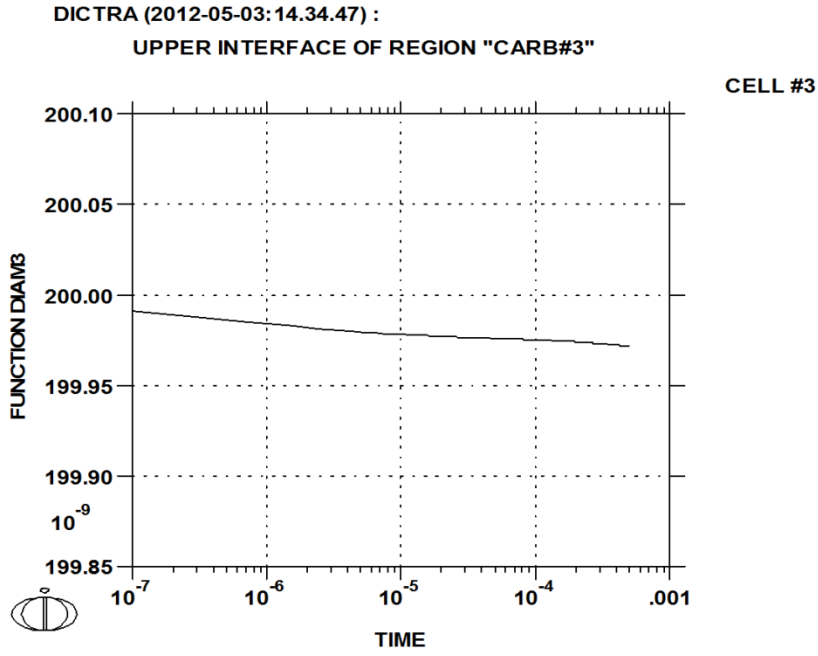
DICTRA (2012-05-03:14.34.47) :
UPPER INTERFACE OF REGION "CARB#3"
CELL #3
200.10
200.05
200.00
199.95
199.90
199.85
FUNCTION DIAM3
10-9
10-7
10-6
10-5
10-4
.001
TIME
2012-05-03 14:34:47.23 output by user rictahlg from MATH40

800°C 1 GPa

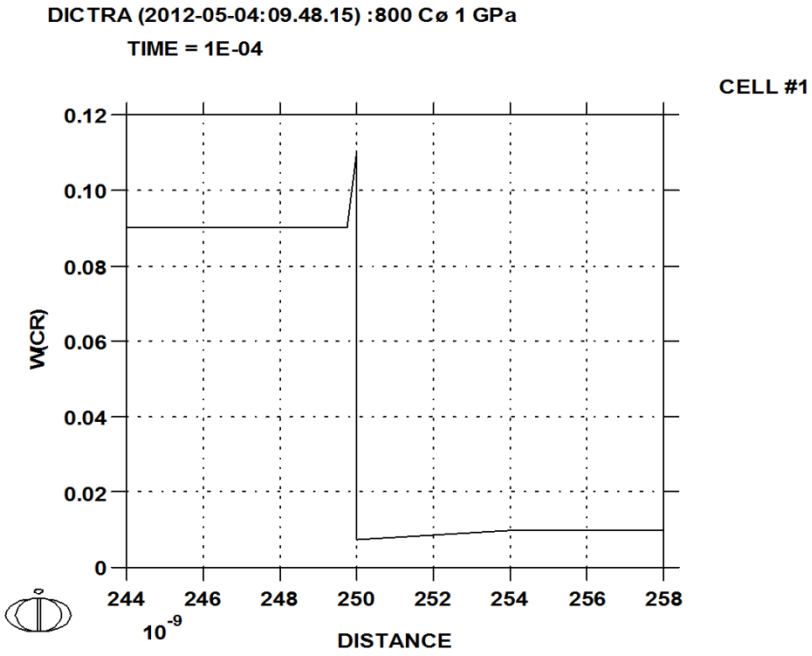

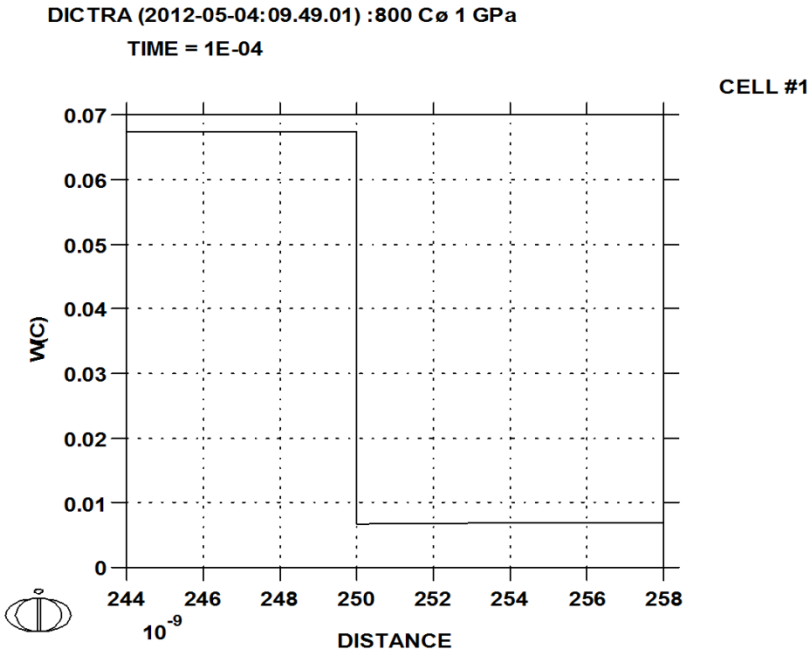

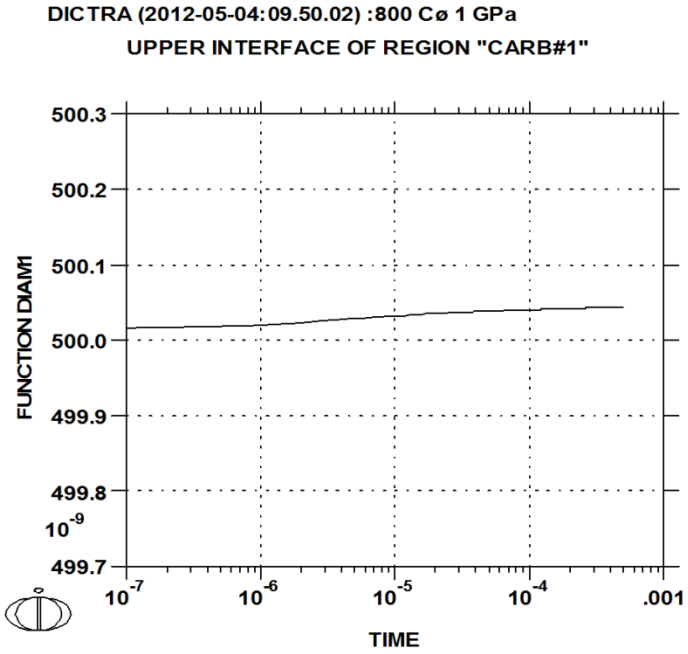

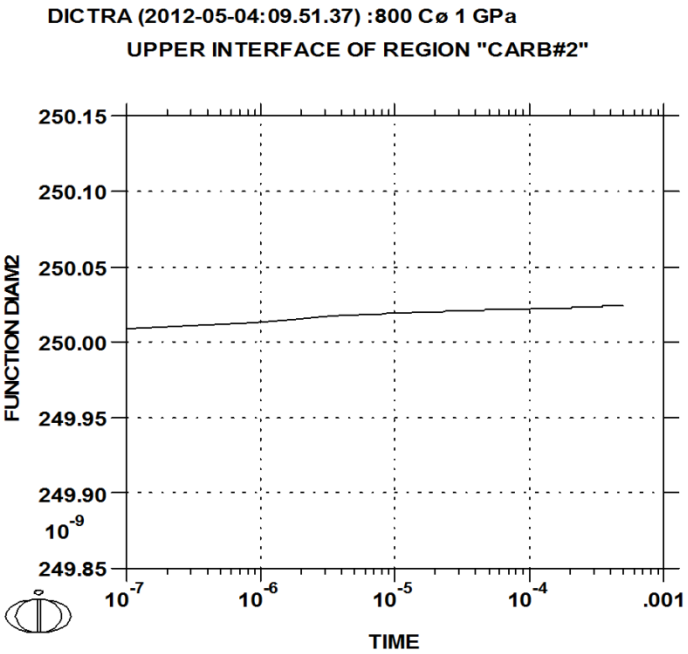

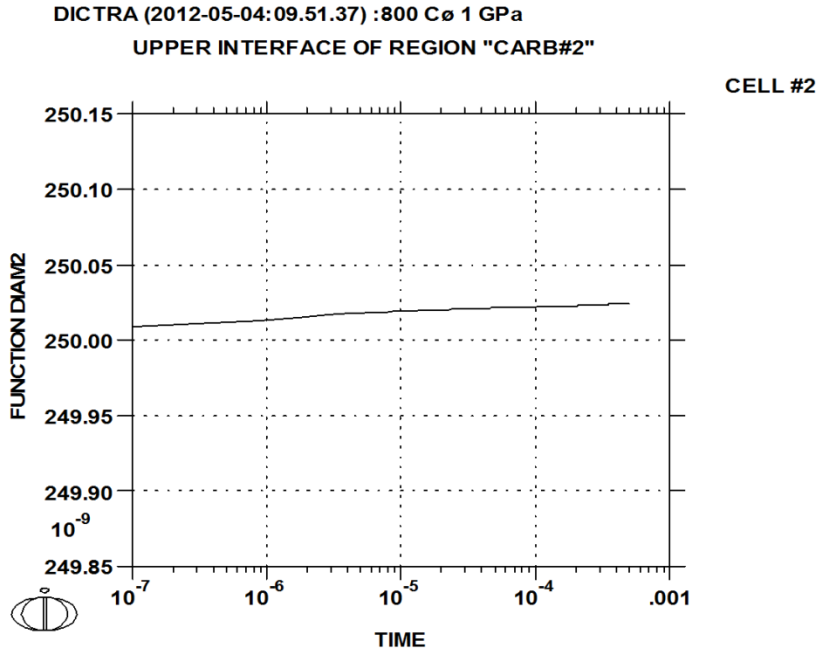

800°C 4 GPa

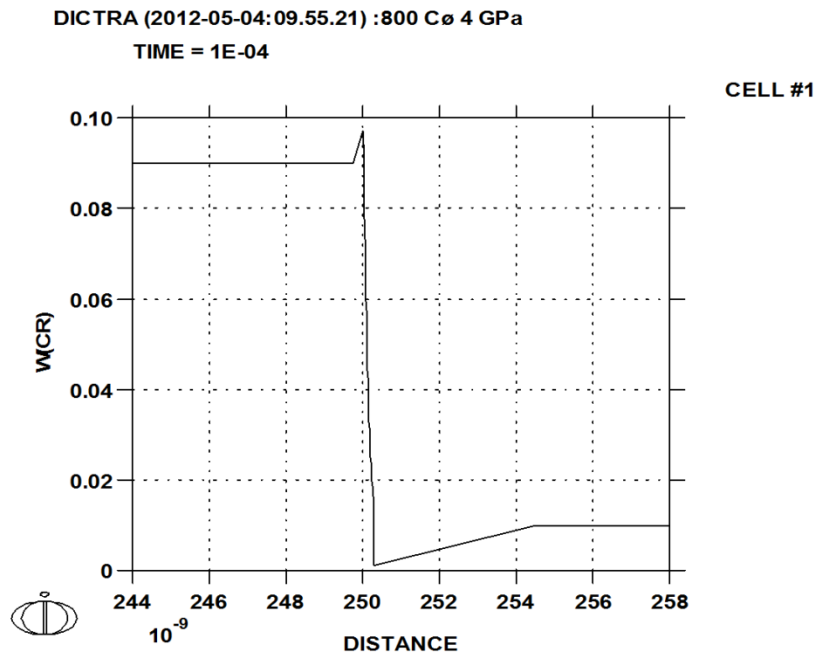

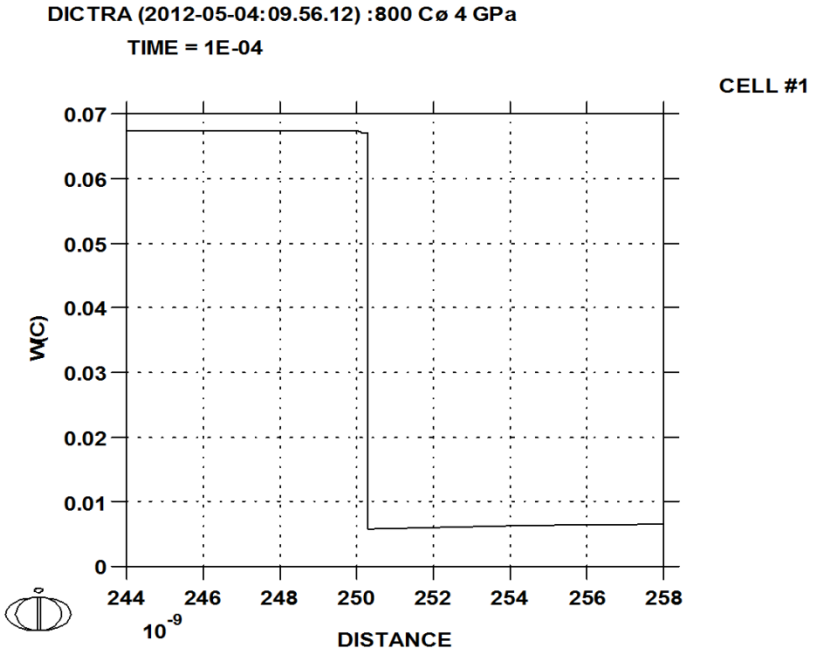

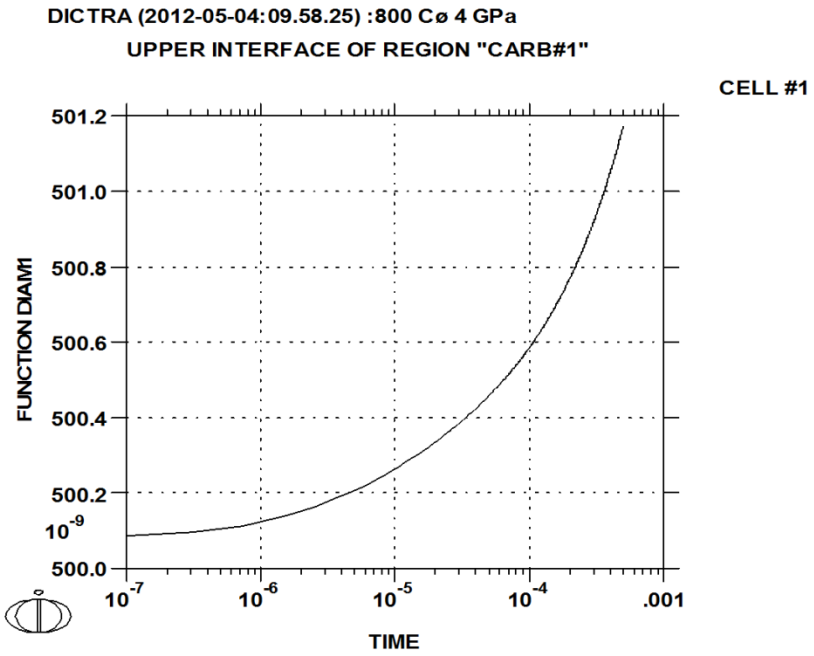

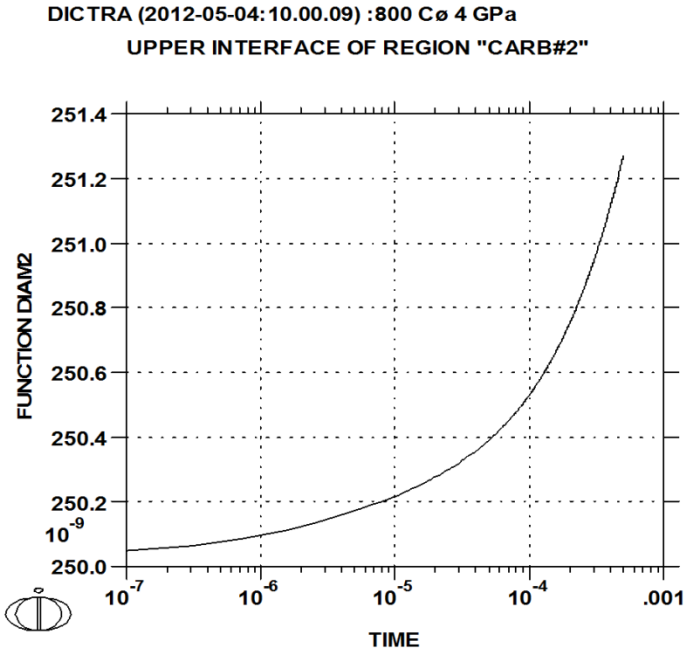

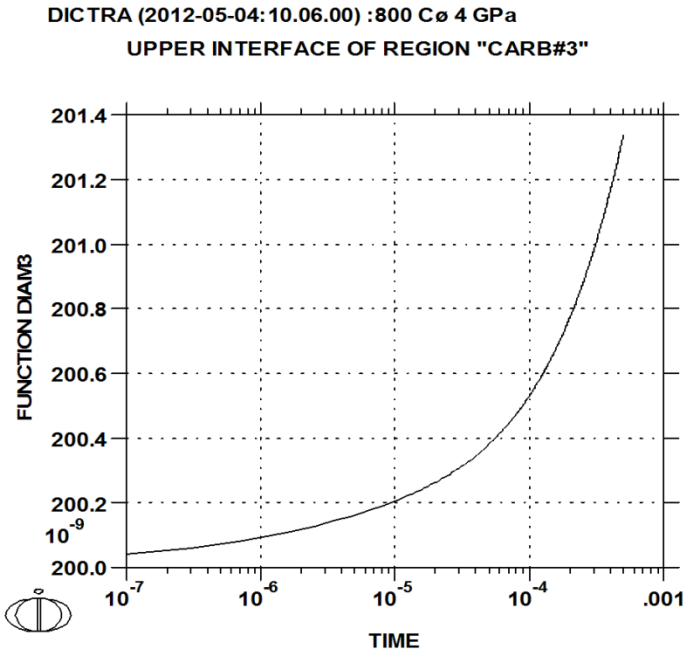

900°C 1 atm

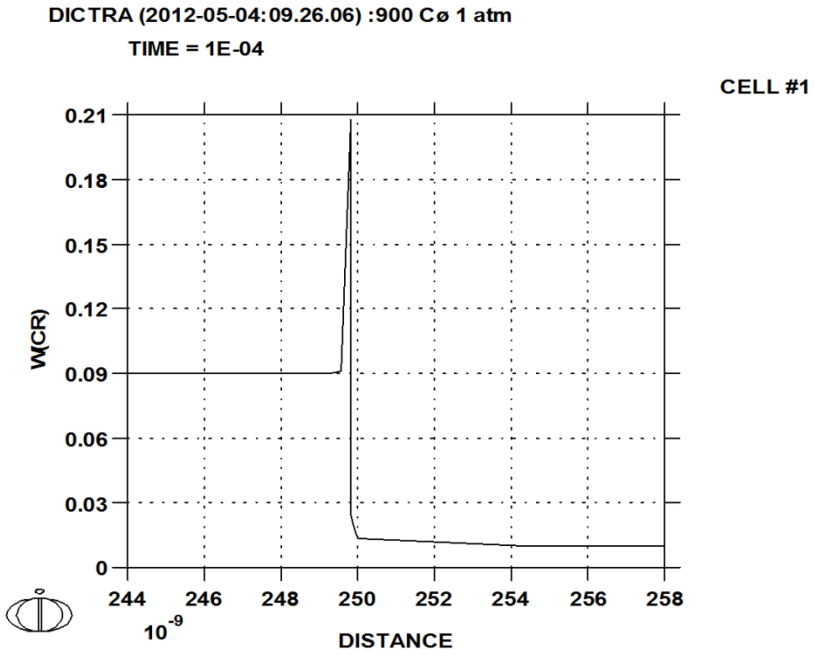

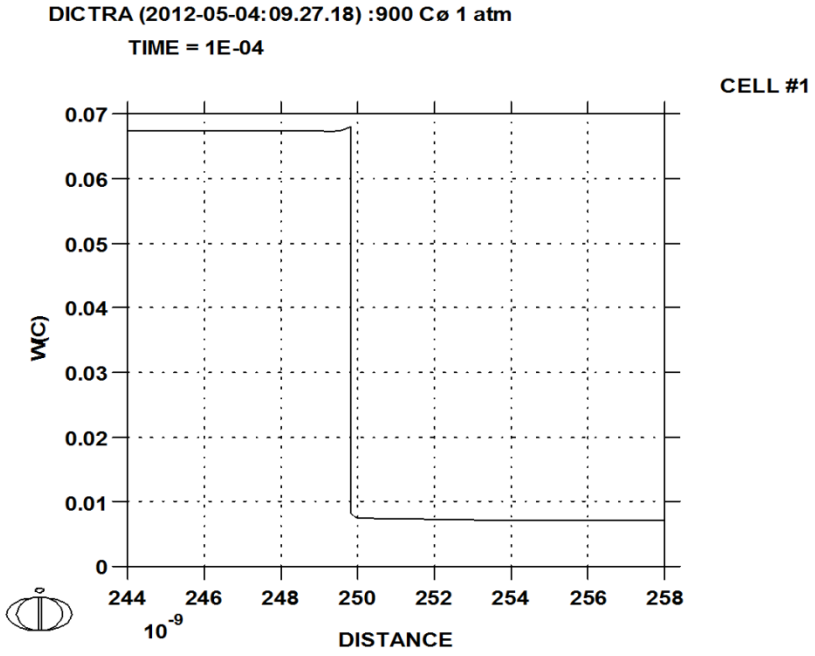

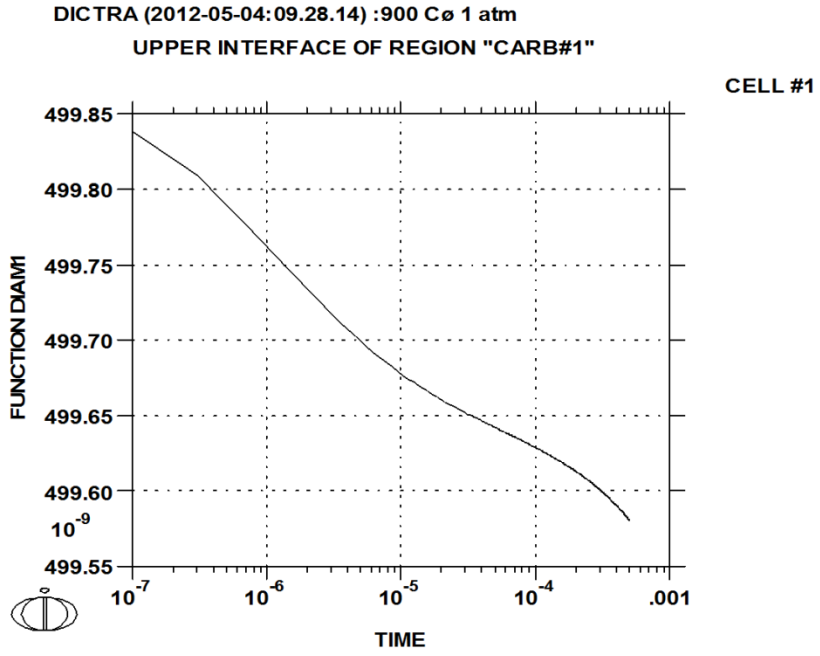

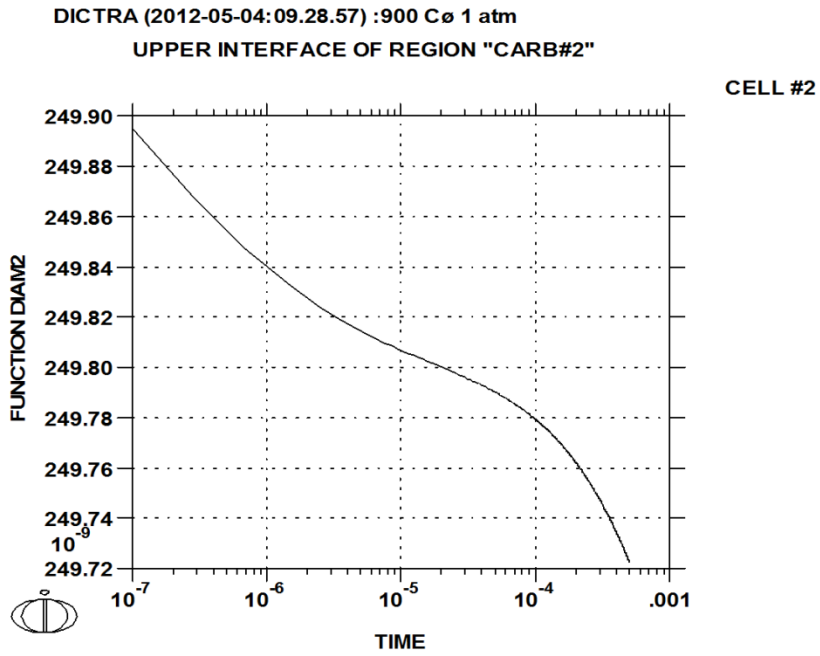

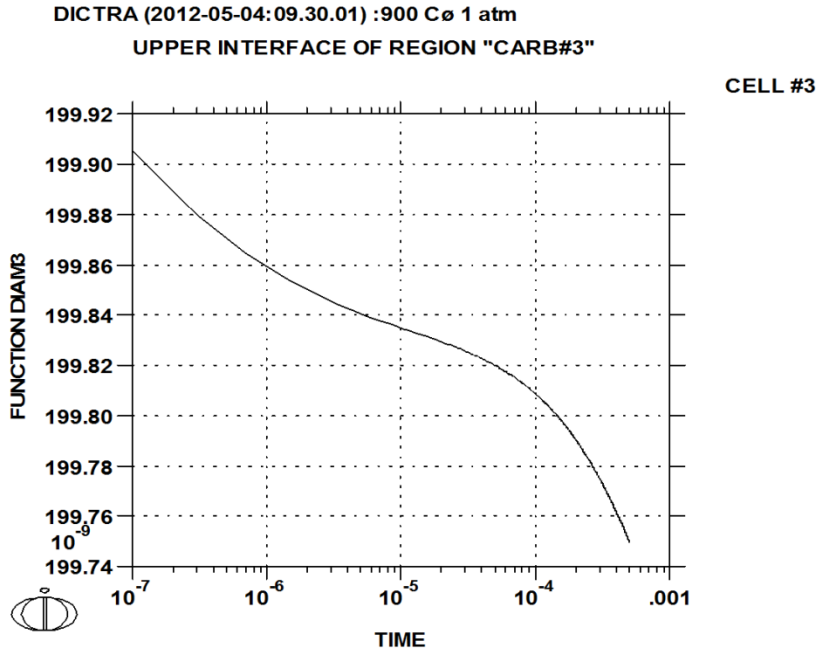

900°C 1 GPa

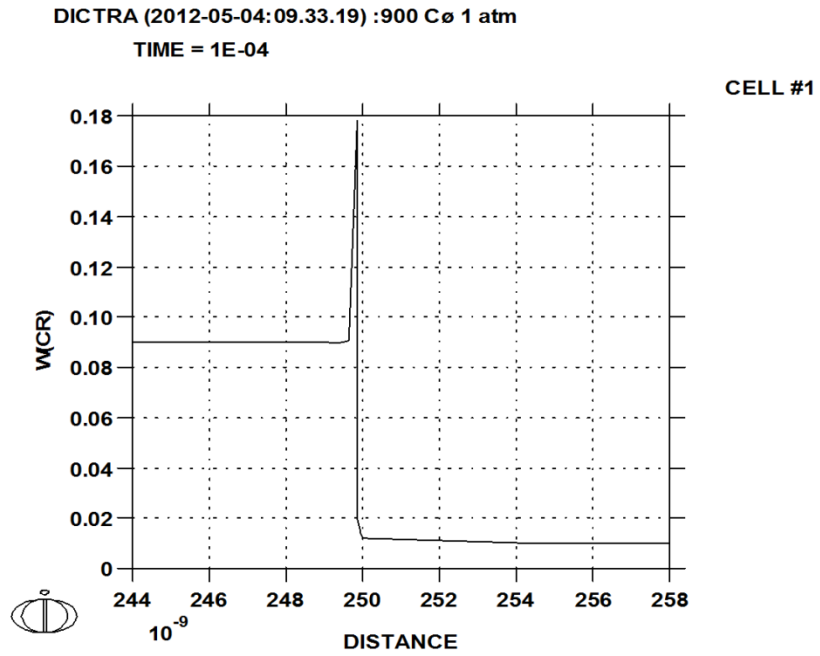

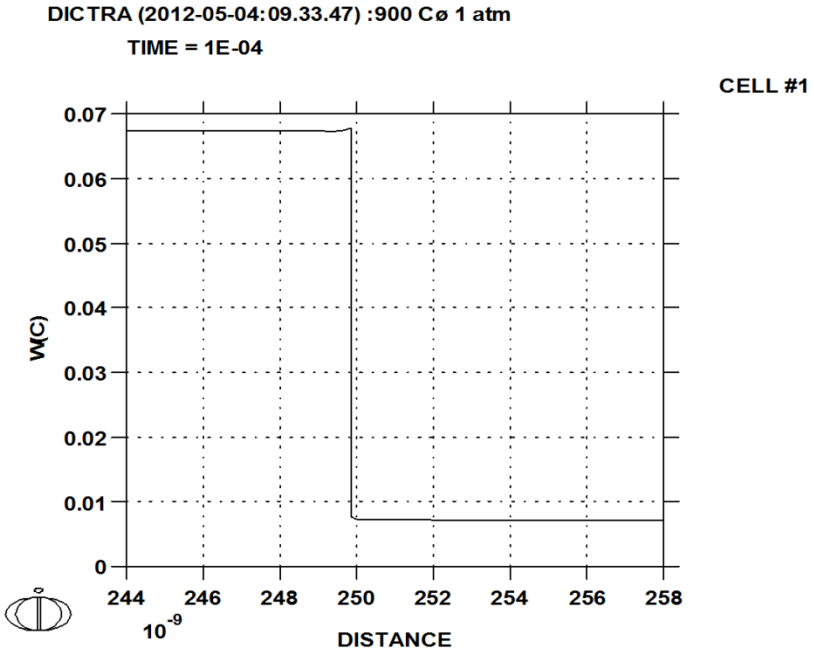

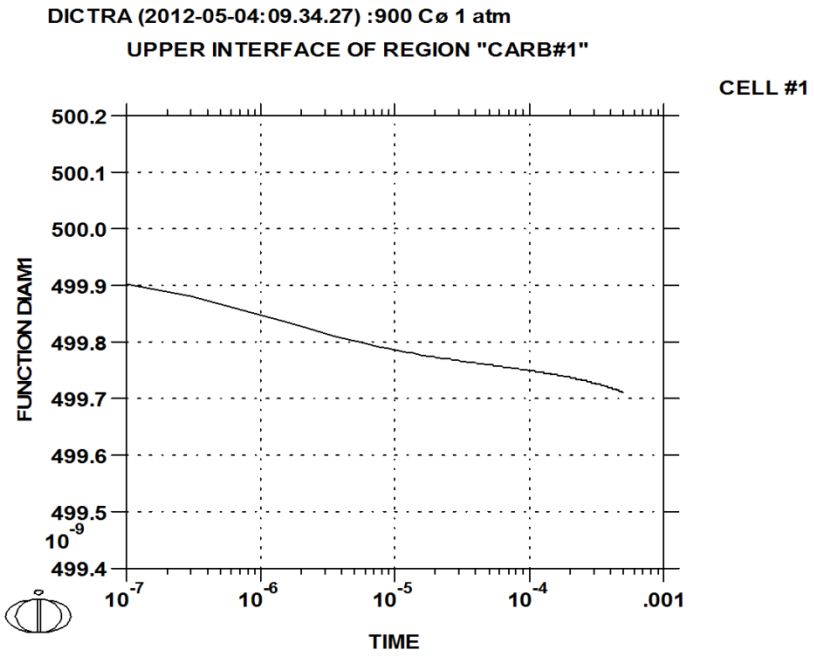

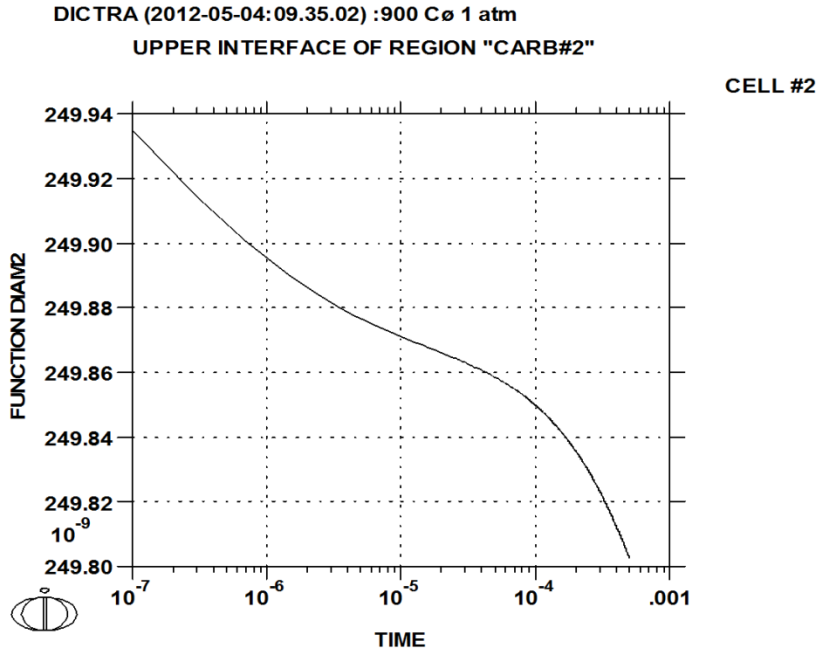

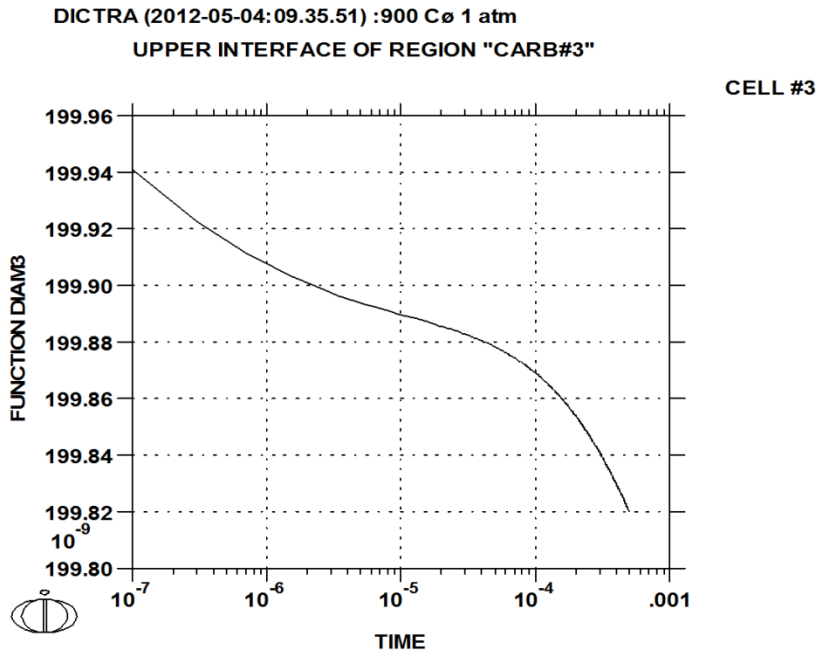

900°C 4 GPa

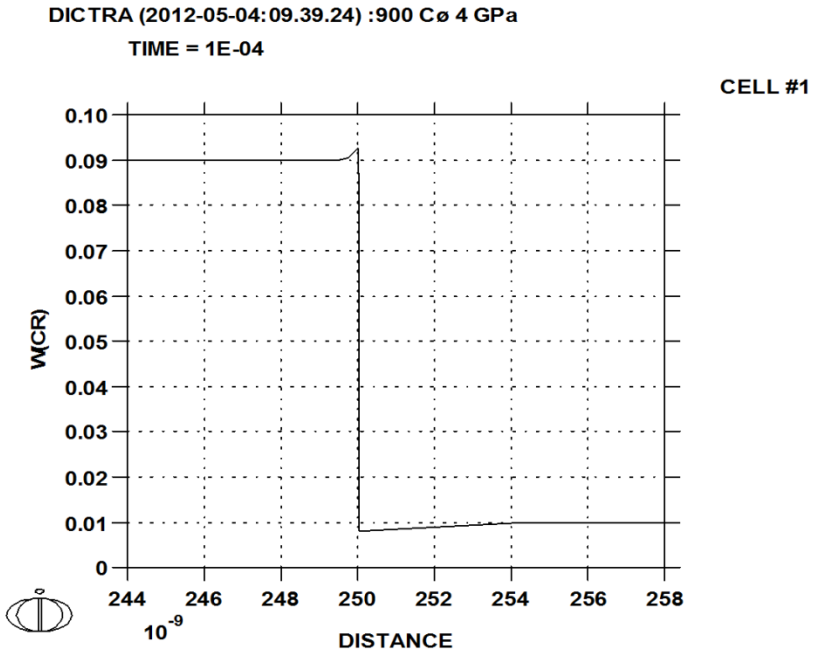

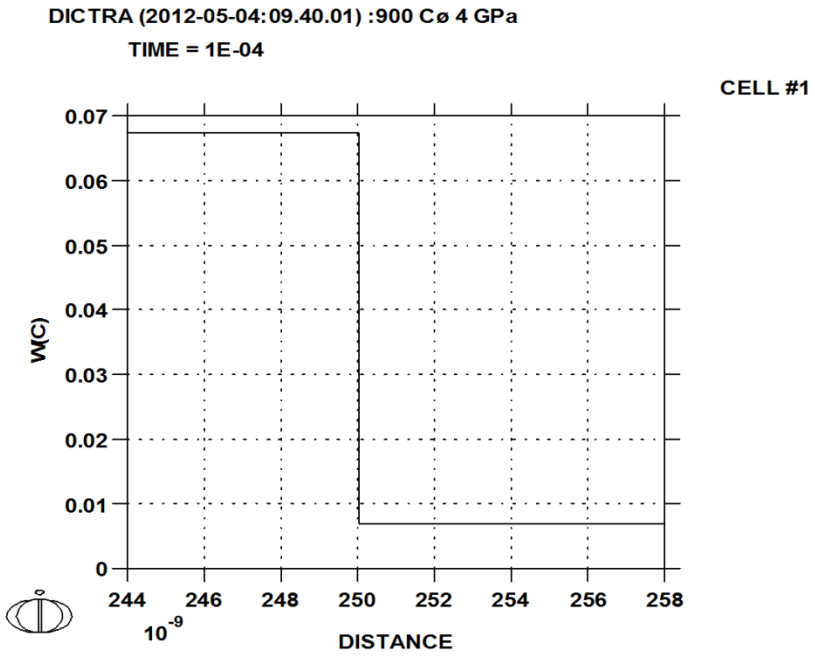

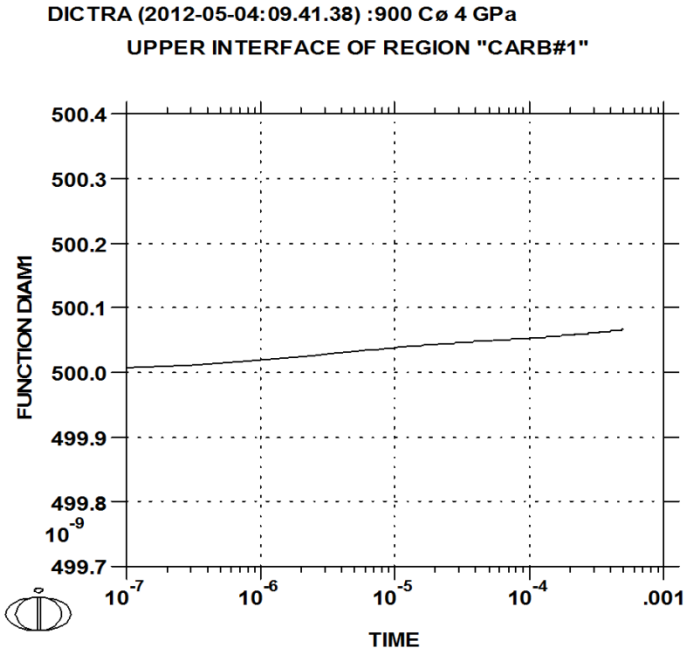

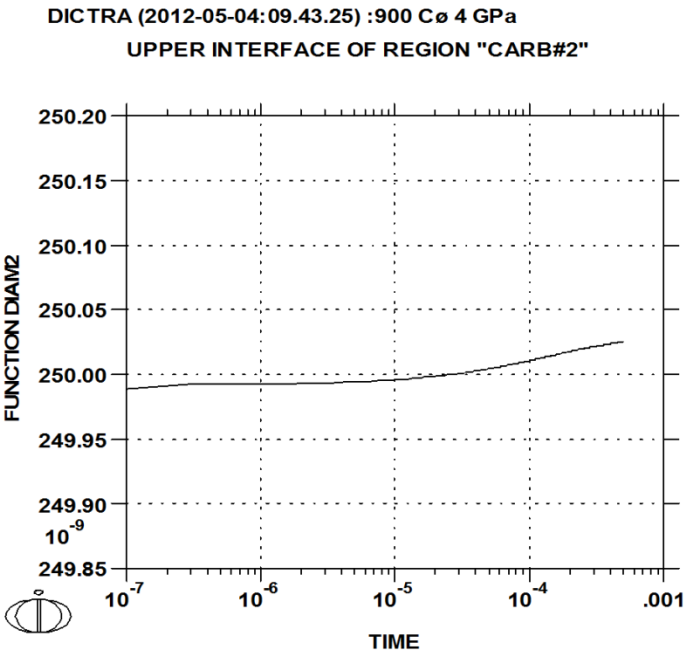

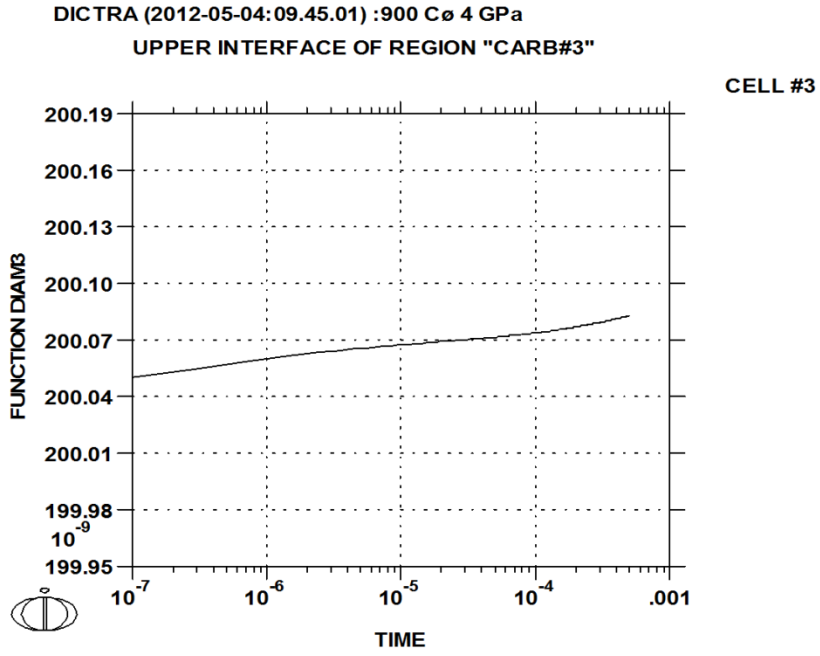
DICTRA (2012-05-04:09.45.01) :900 Cø 4 GPa
UPPER INTERFACE OF REGION "CARB#3"
CELL #3
FUNCTION DIAM3
200.19
200.16
200.13
200.10
200.07
200.04
200.01
199.98
10-9
199.95
10-7
10-6
10-5
10-4
.001
TIME
2012-05-04 09:45:01.35 output by user rickahlg from MAT048

950°C 1 atm

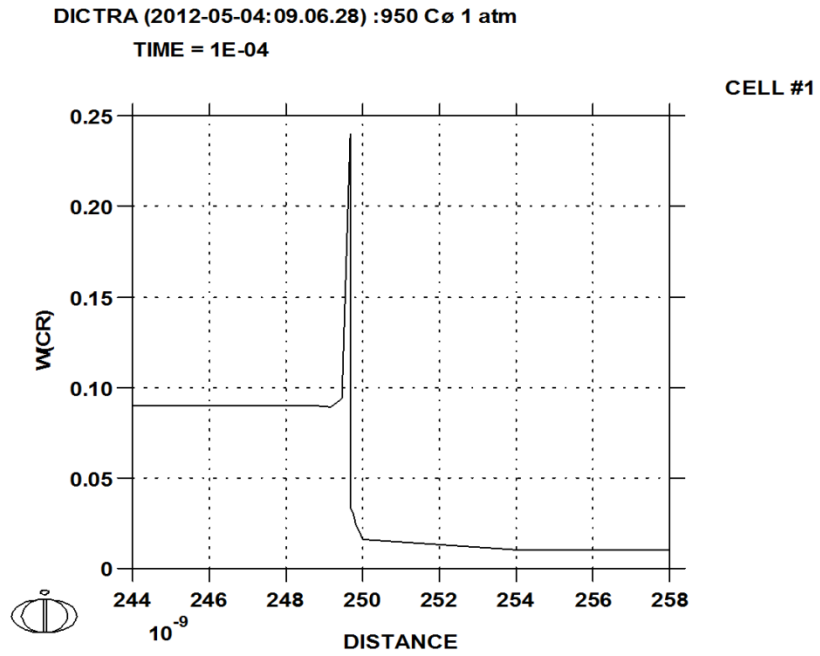
DICTRA (2012-05-04:09.06.28) :950 Cø 1 atm
TIME = 1E-04
CELL #1
W(CR)
0.25
0.20
0.15
0.10
0.05
0
244
246
248
250
252
254
256
258
10-9
DISTANCE
2012-05-04 09:06:28.04 output by user rickahlg from MAT048

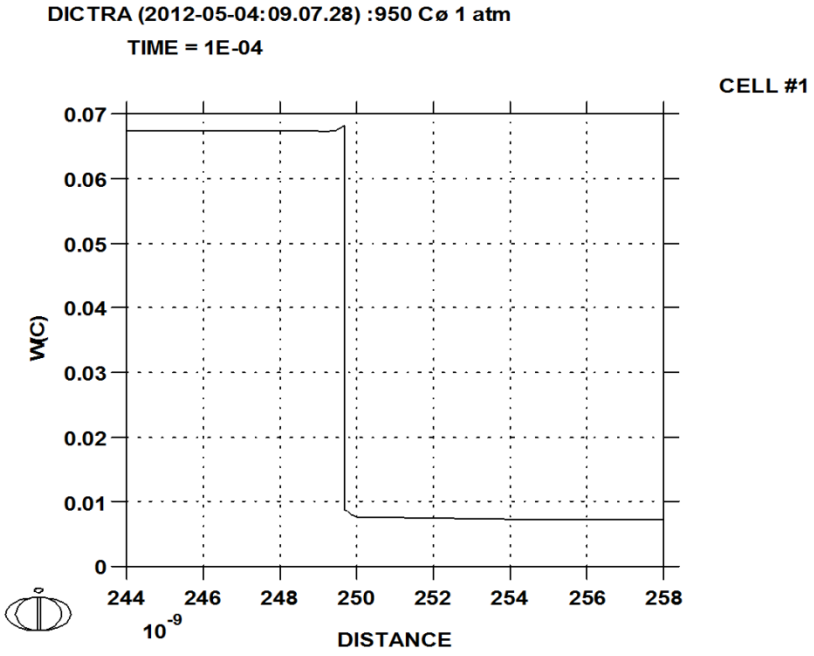

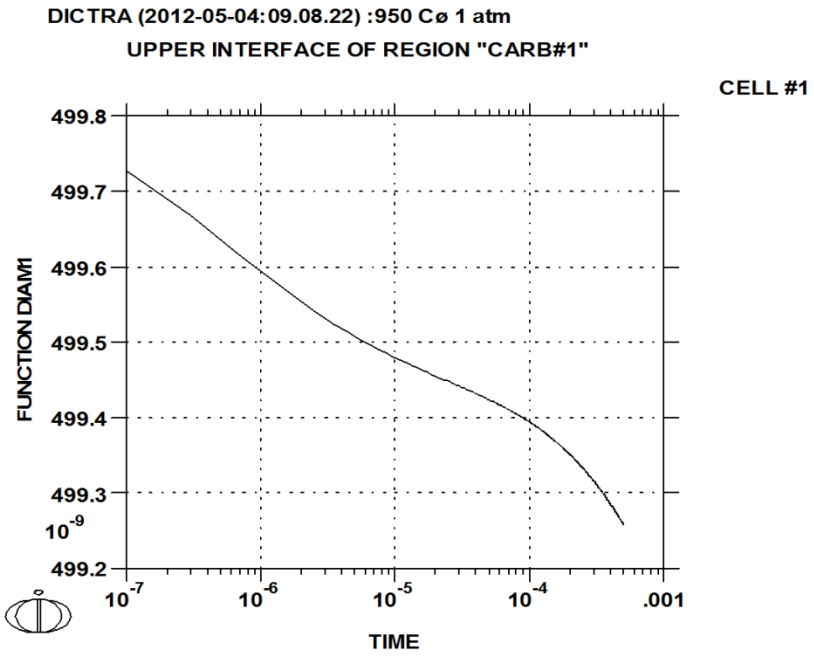

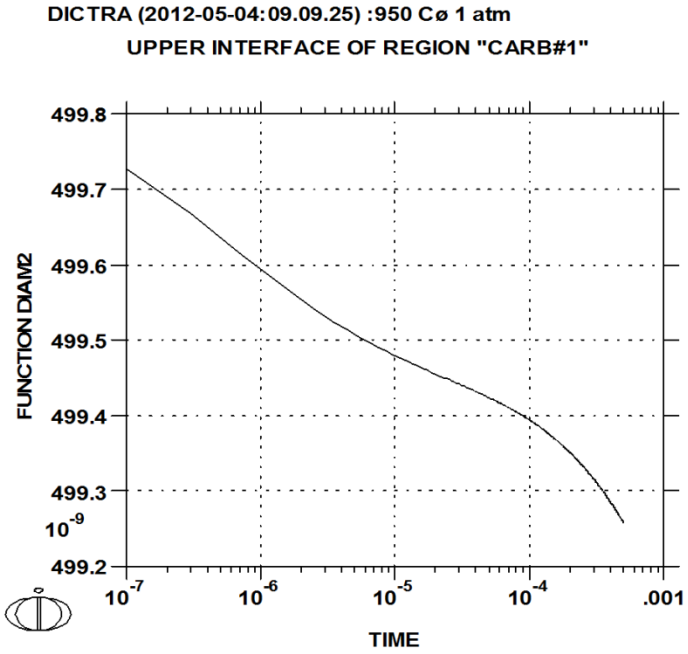

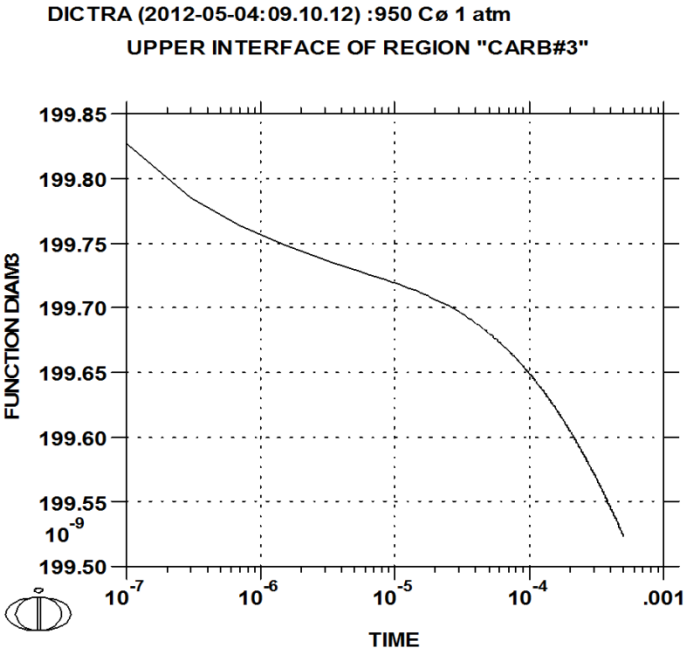

950°C 1 GPa

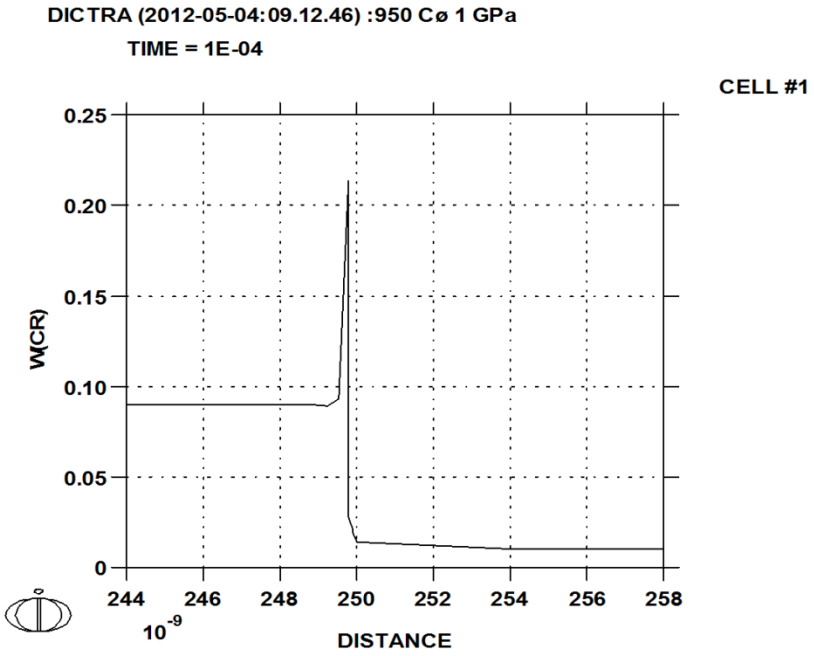

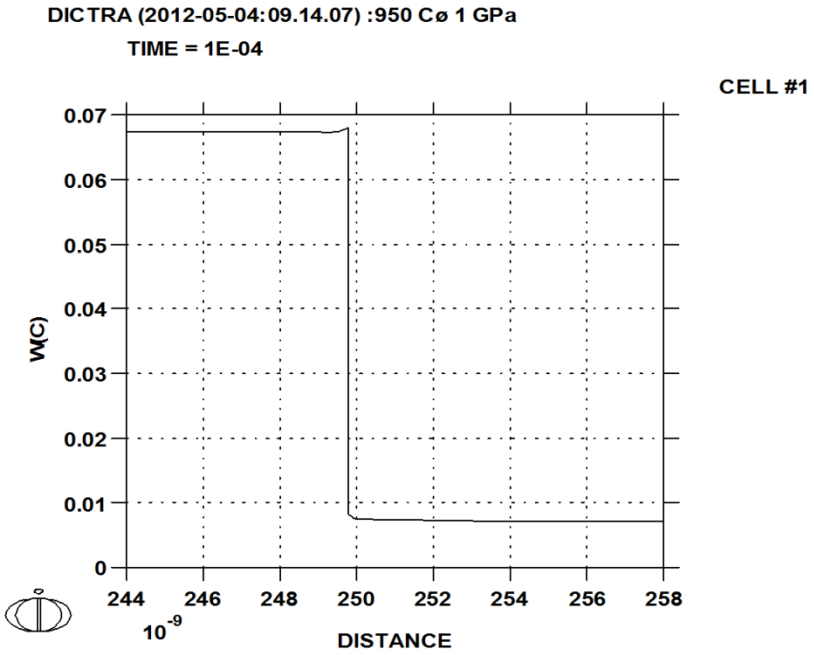

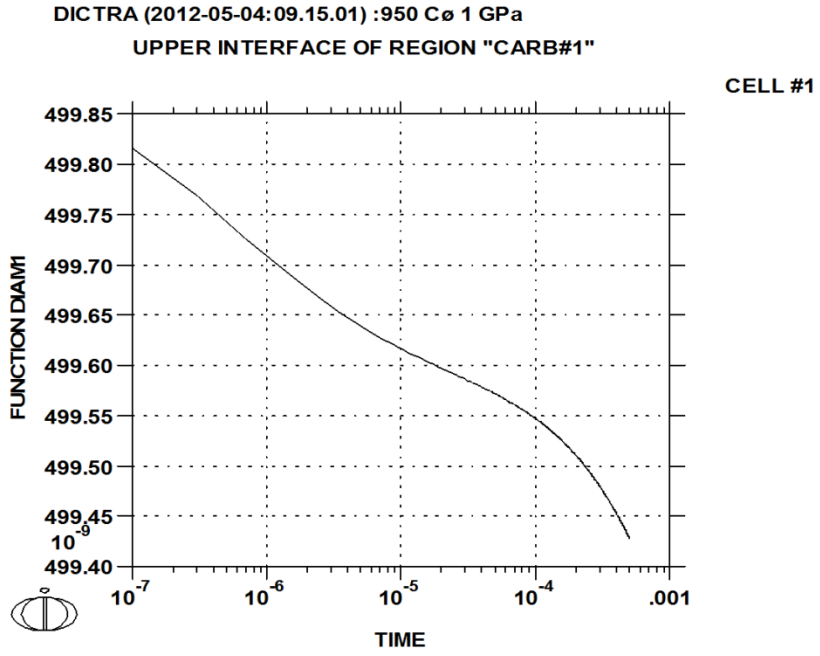

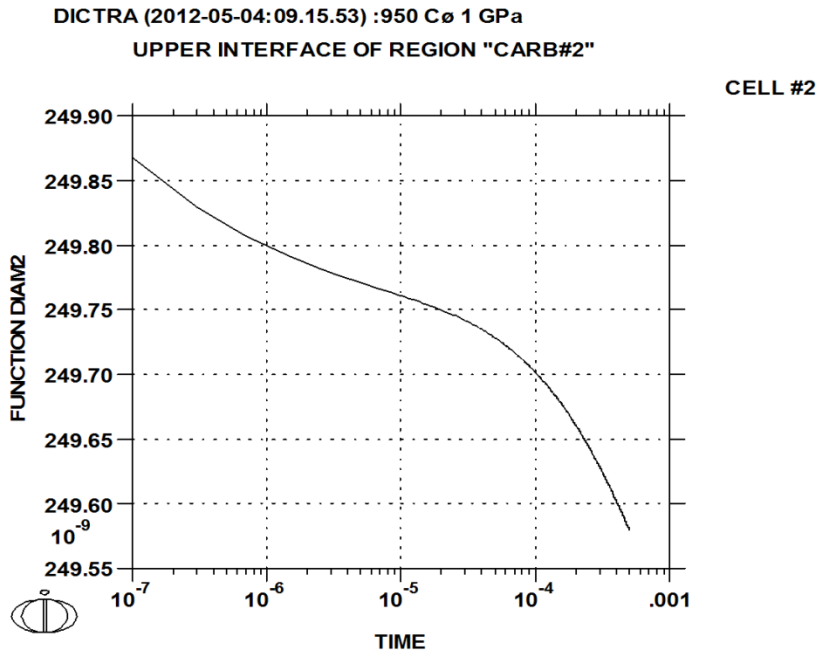

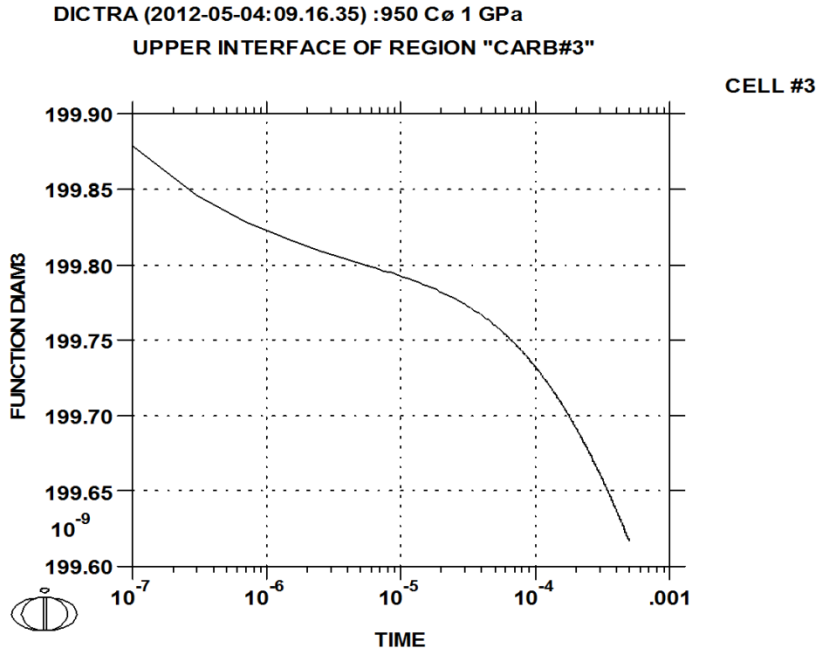

950°C 4 GPa

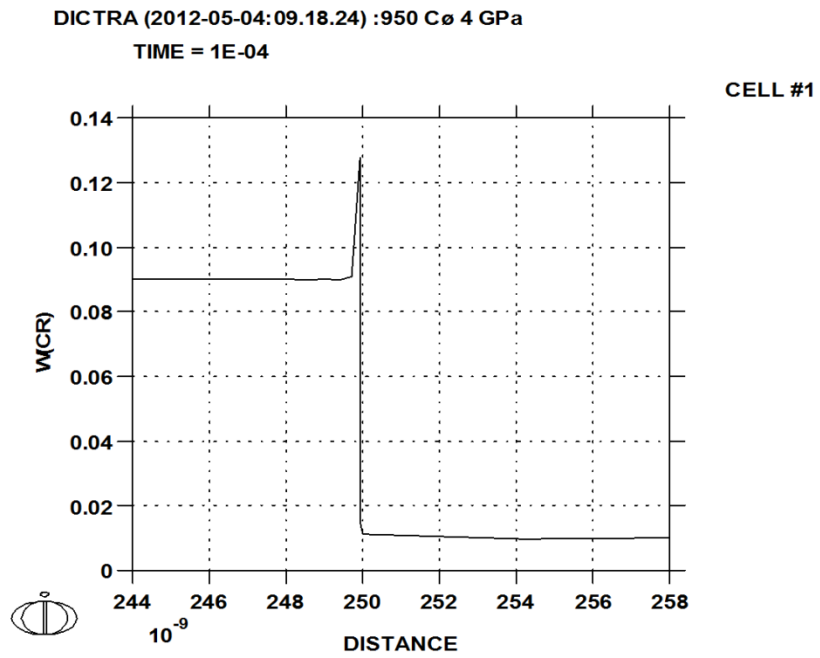

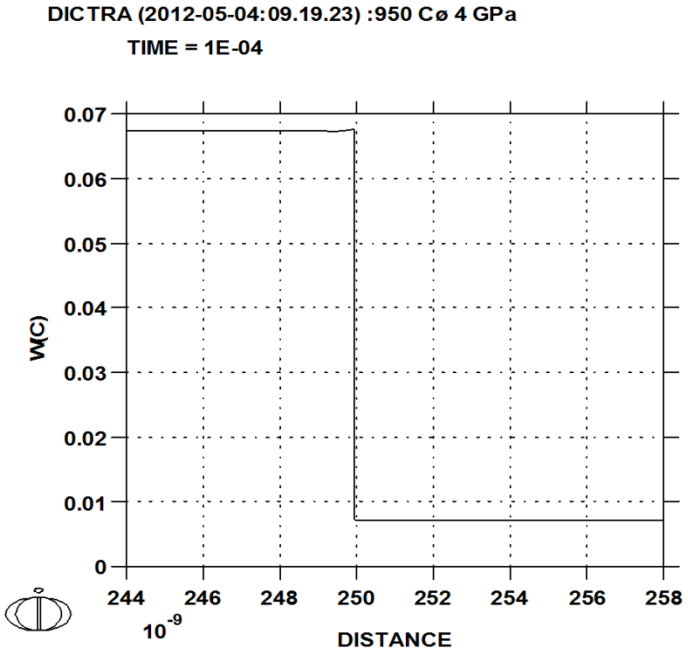

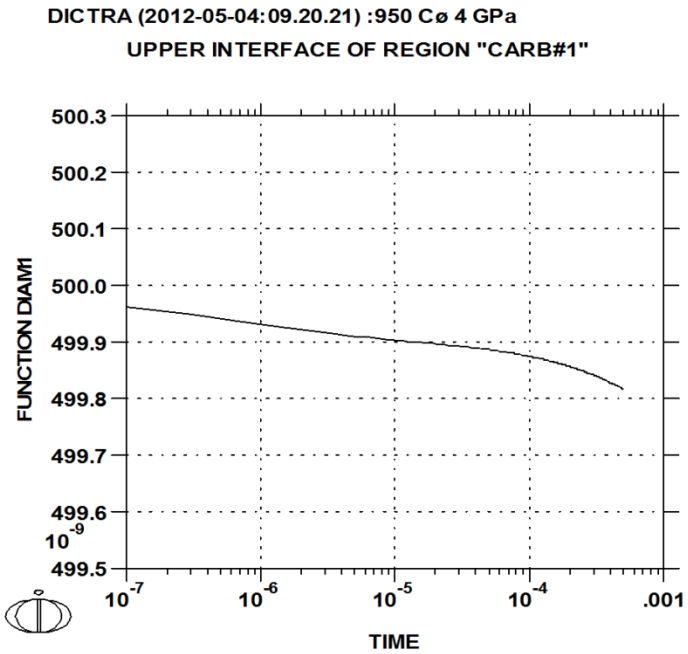

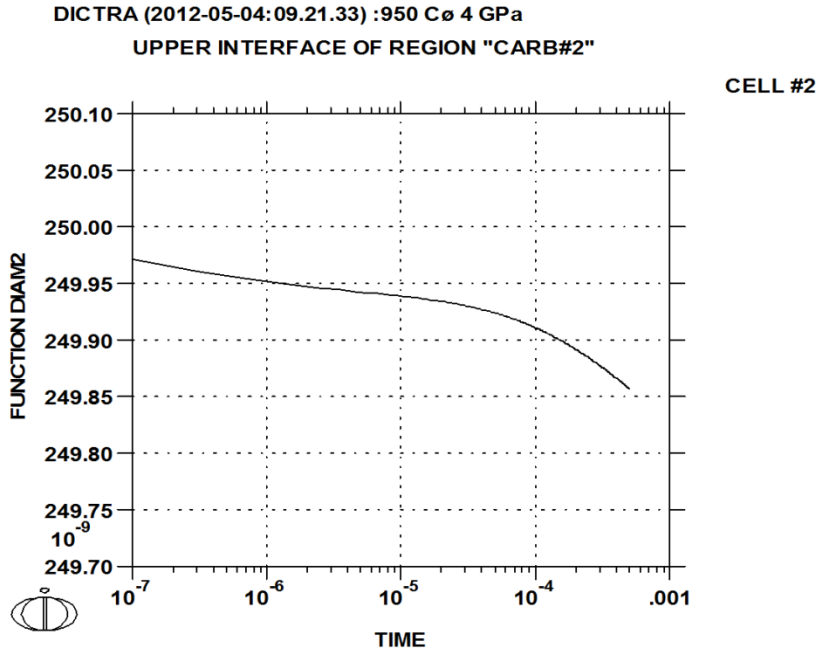

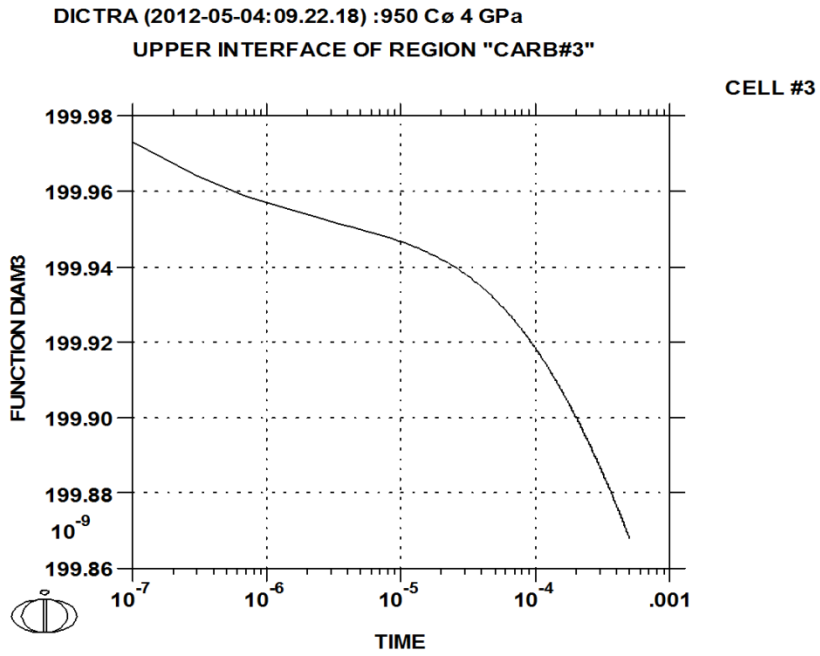

1000°C 1 atm

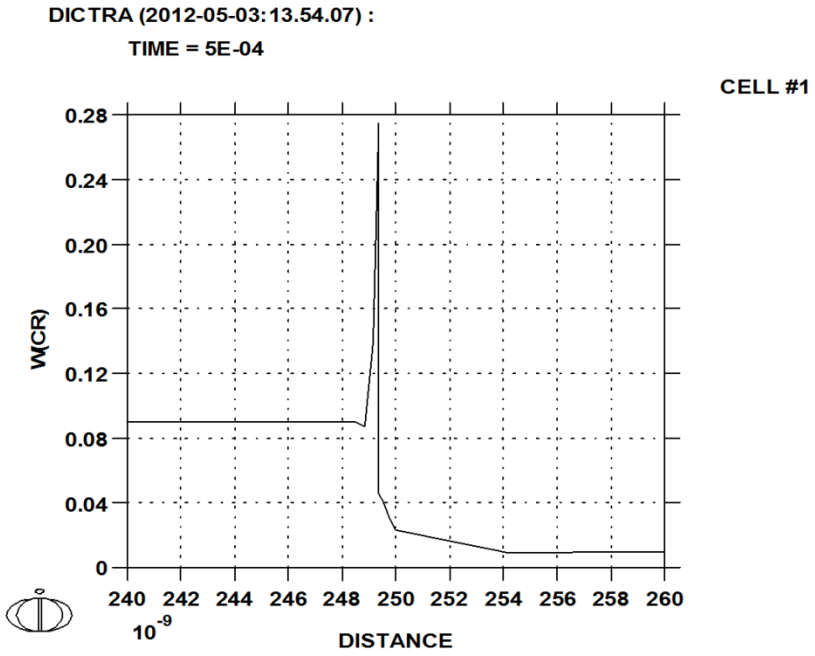

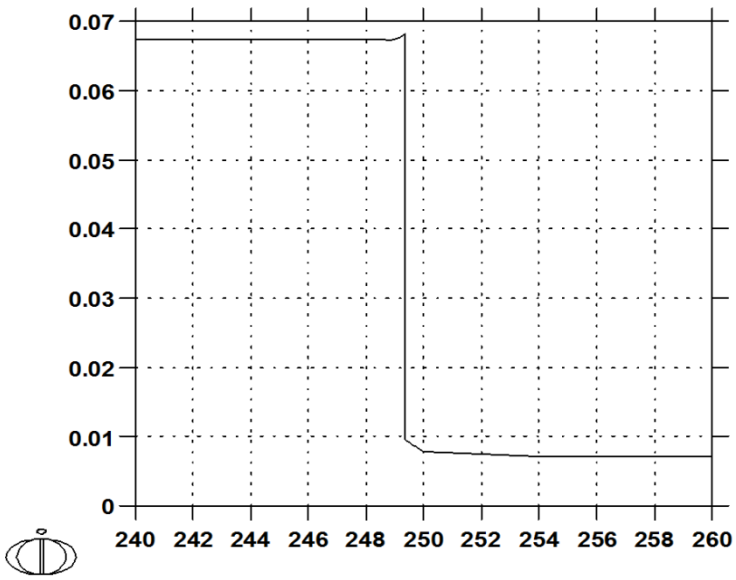

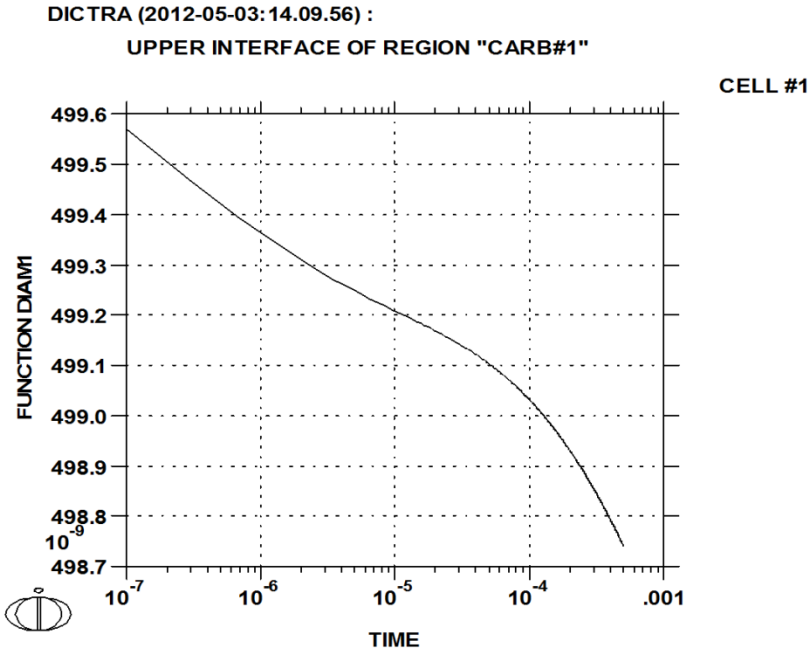
DICTRA (2012-05-03:14.09.56) :
UPPER INTERFACE OF REGION "CARB#1"
CELL #1
FUNCTION DIAM1
499.6
499.5
499.4
499.3
499.2
499.1
499.0
498.9
498.8
10-9
498.7
10-7
10-6
10-5
10-4
.001
TIME
2012-05-03 14:09:56.13 output by user rictahlg from MATH40

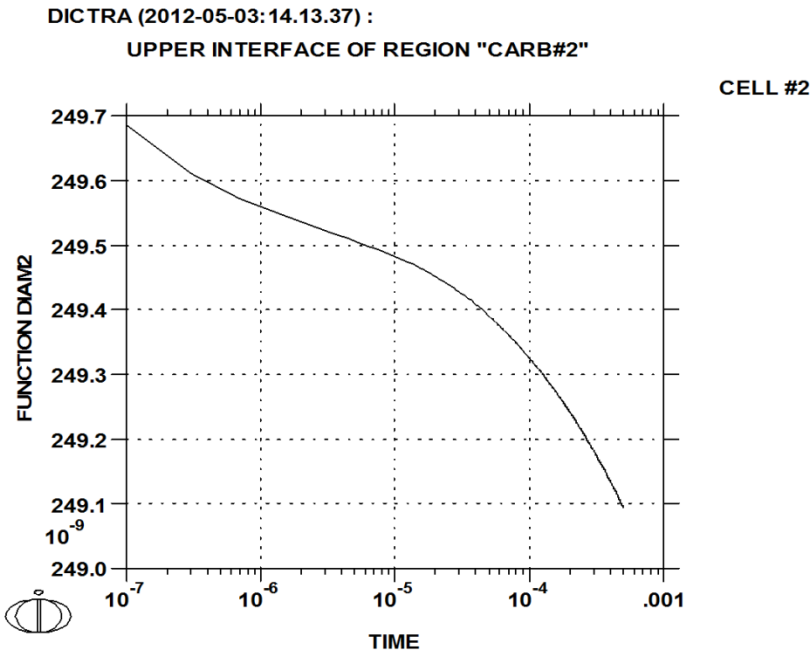
DICTRA (2012-05-03:14.13.37) :
UPPER INTERFACE OF REGION "CARB#2"
CELL #2
FUNCTION DIAM2
249.7
249.6
249.5
249.4
249.3
249.2
249.1
10-9
249.0
10-7
10-6
10-5
10-4
.001
TIME
2012-05-03 14:13:37.10 output by user rictahlg from MATH40

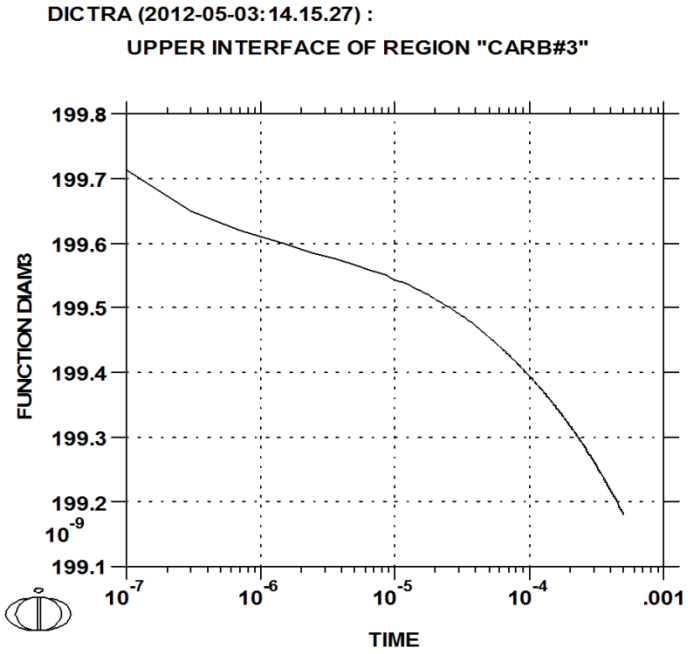

1000°C 1 GPa

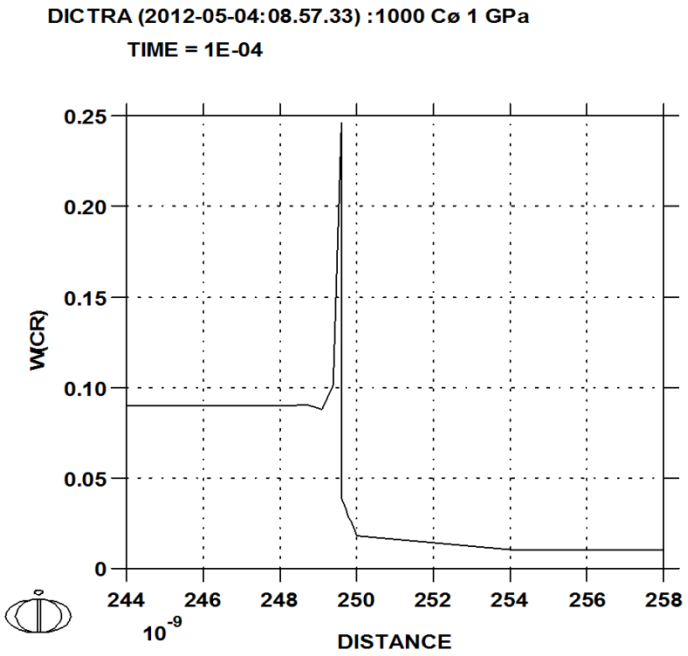

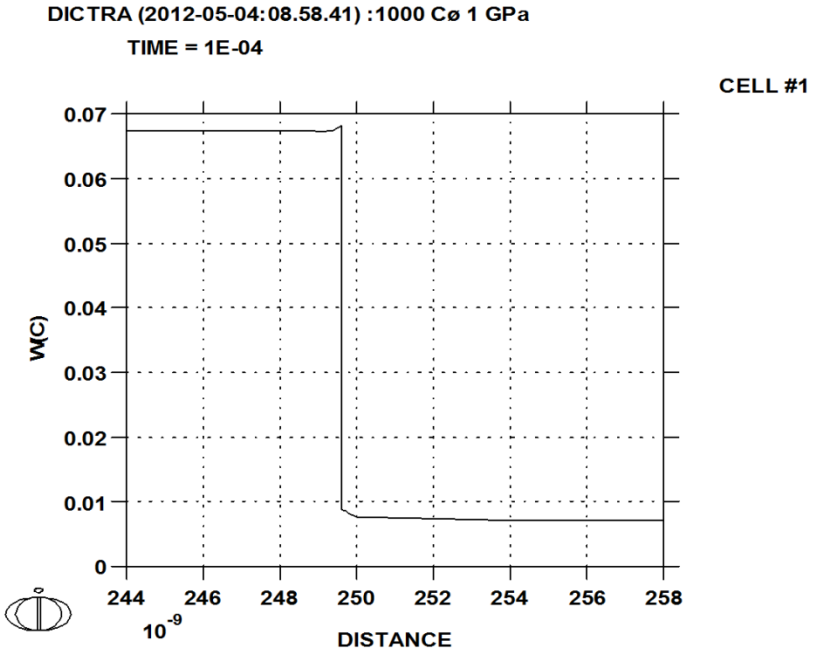

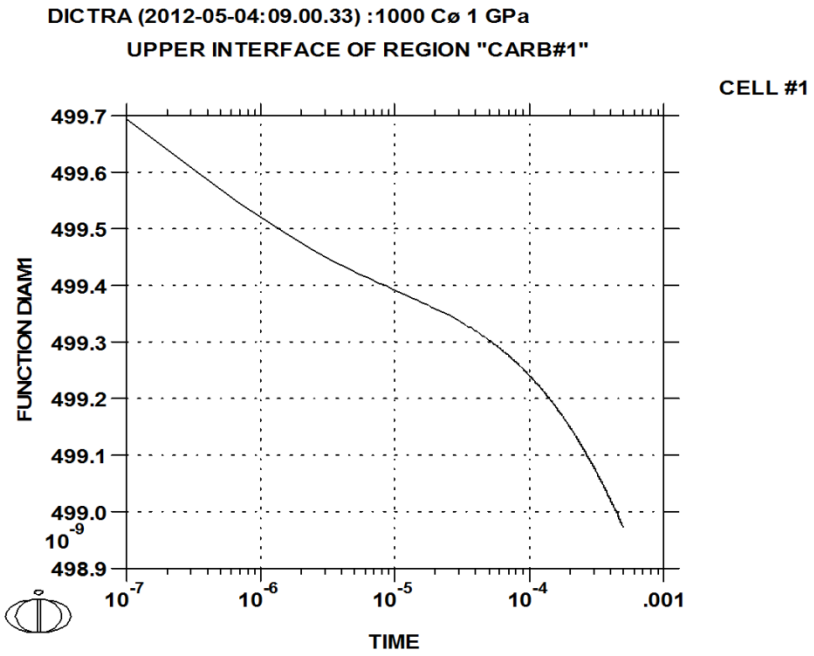

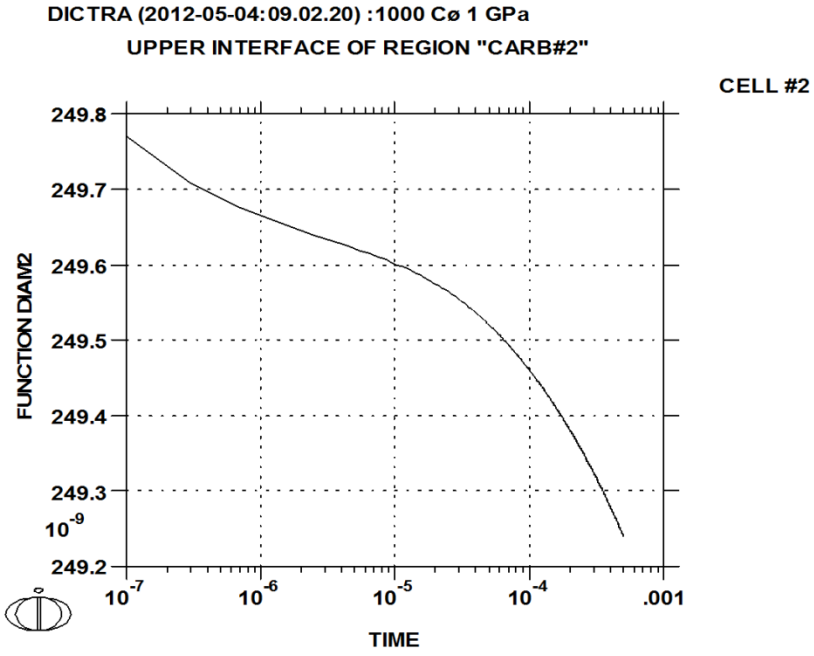

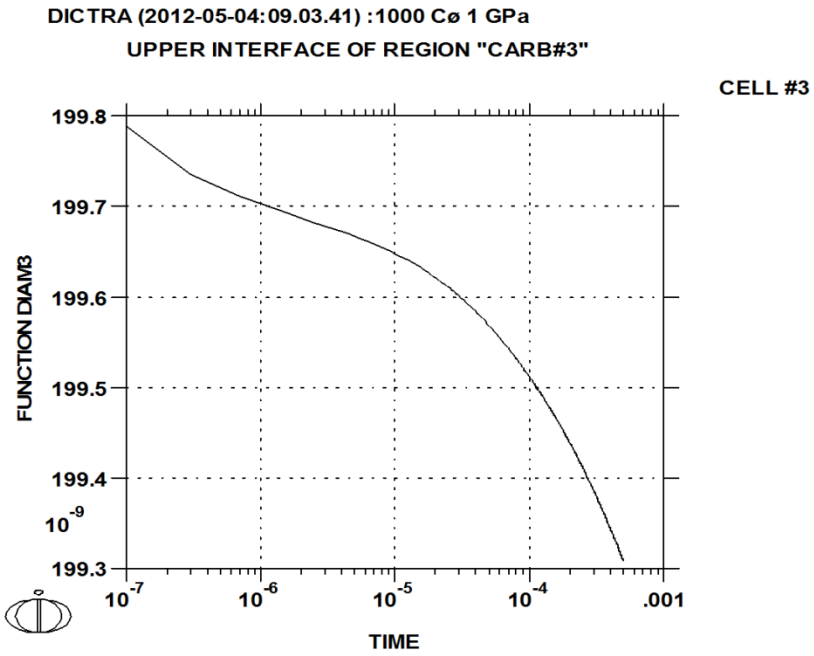

1000°C 4 GPa

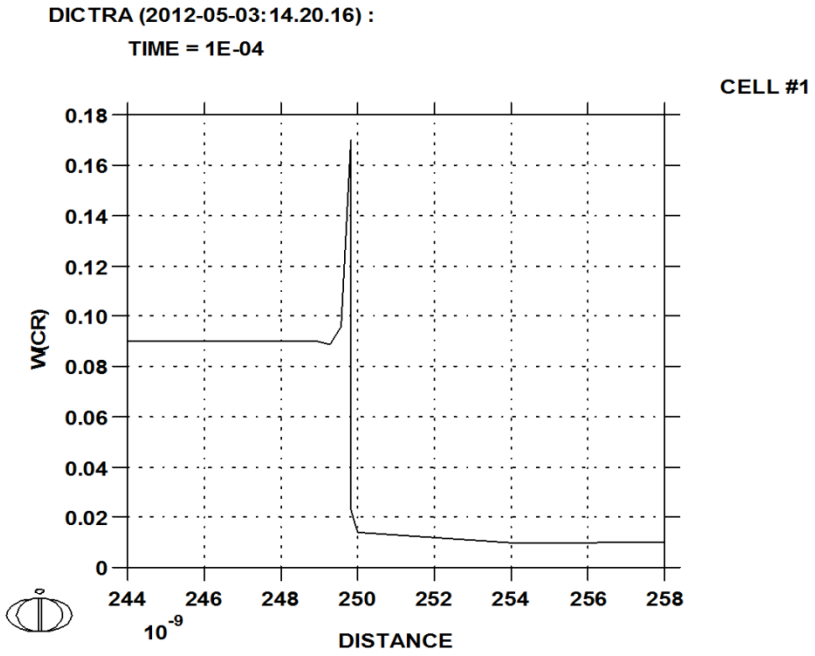

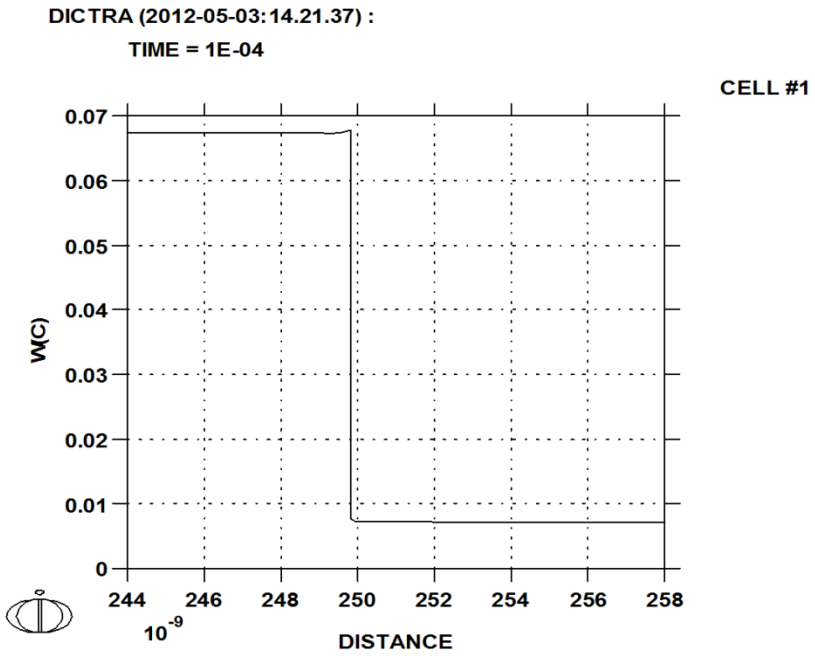

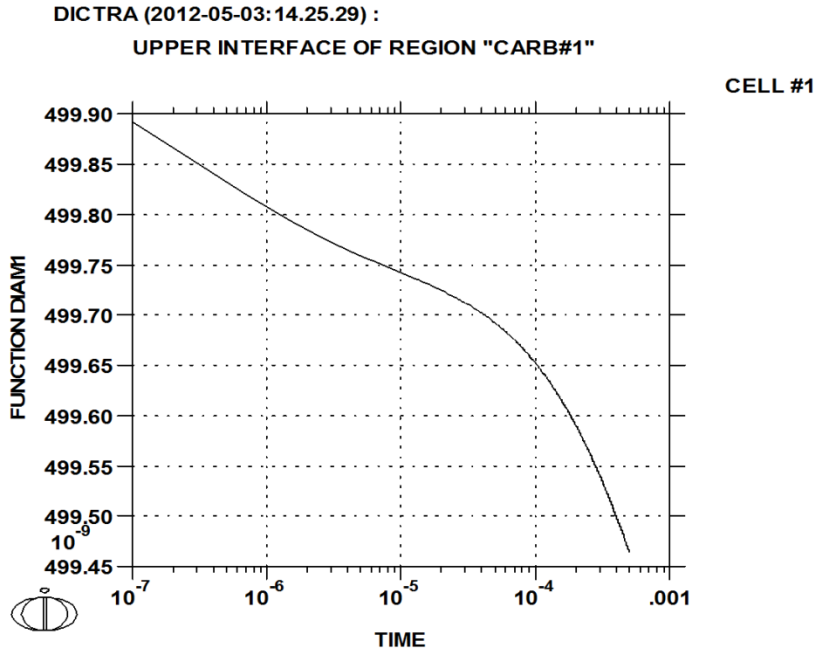

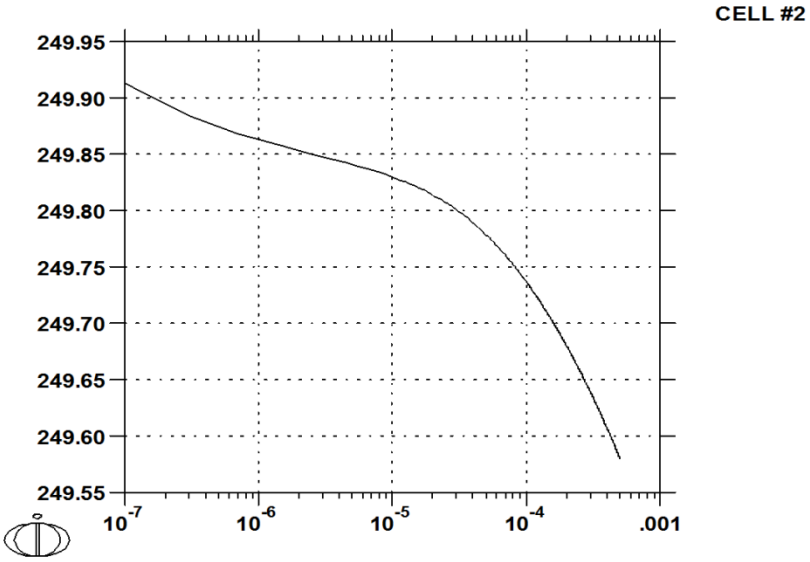

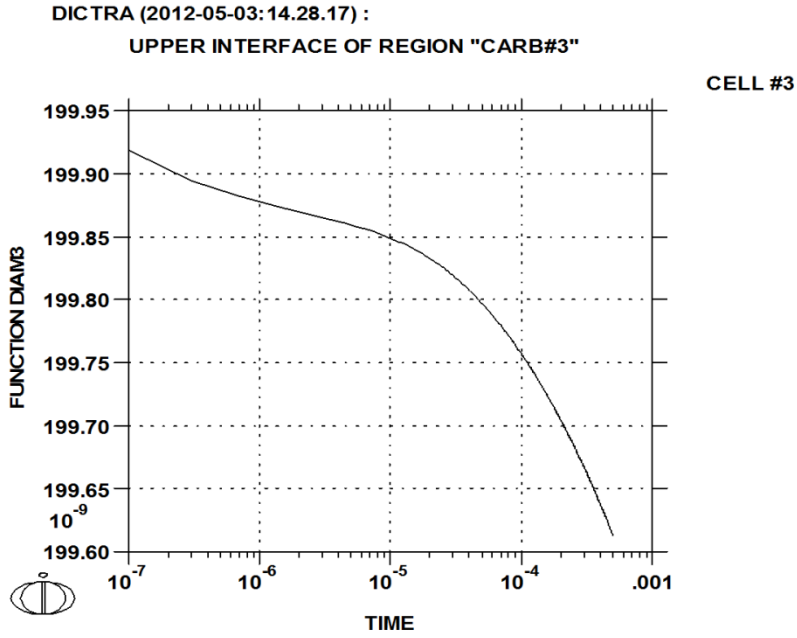

1100°C 1 atm

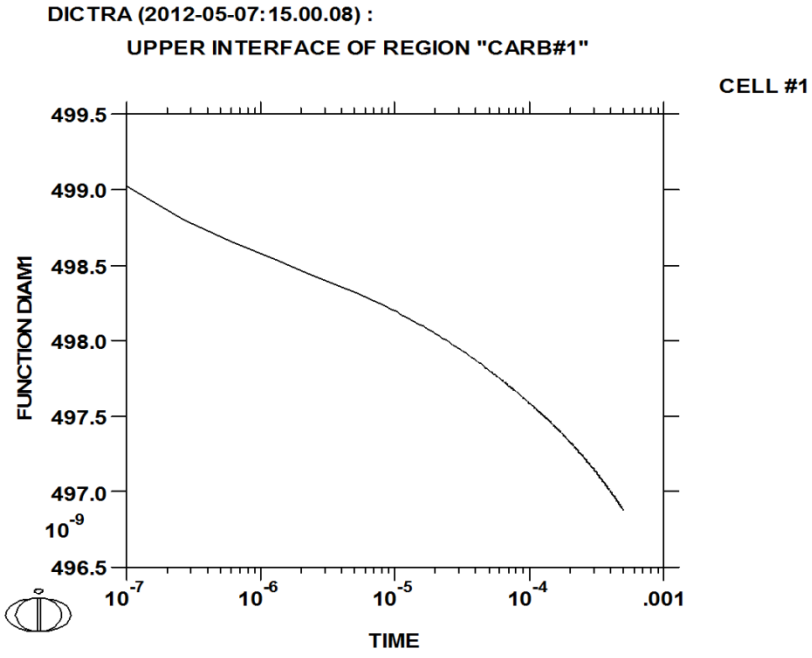

1200°C 1 atm

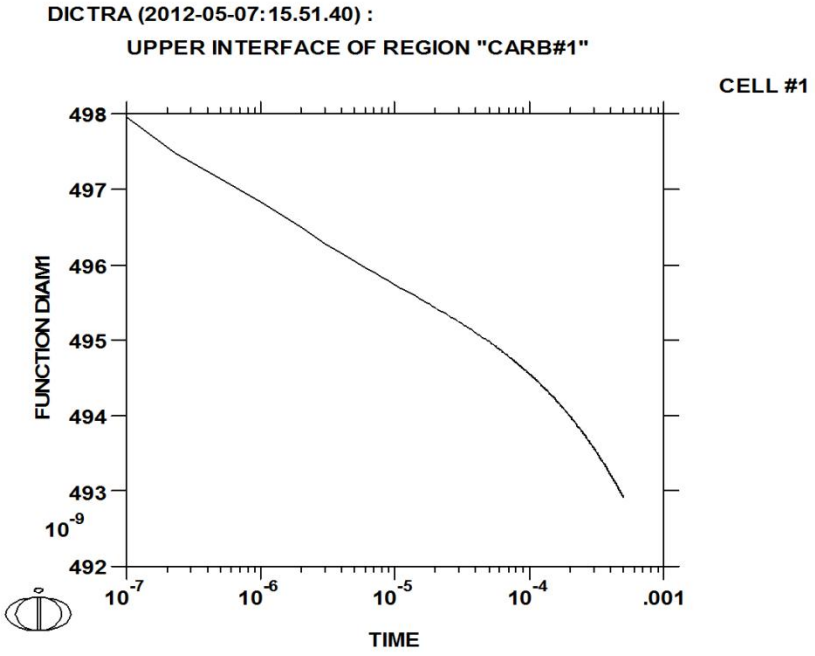

1300°C 1 atm

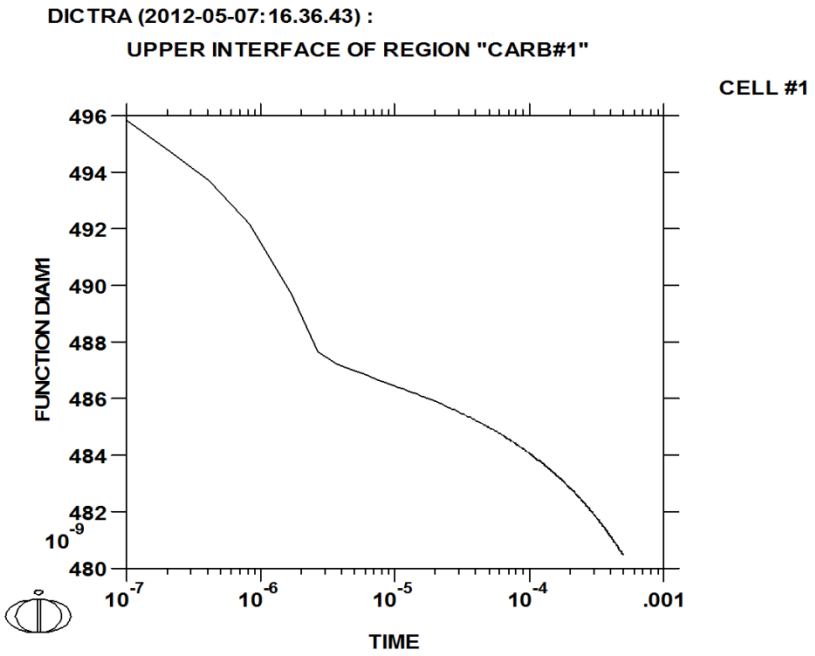

Appendix B

```
@@
@@ RETRIEVE DATA FROM DATABASE
@@

go da

@@USE A PUBLIC DATABASE FOR THERMODYNAMIC DATA
@@ Here the database tcfe6 from thermocalc is chosen

switch tcfe6

@@Specify which elements you have in your system. Here Iron Chromium and Carbon is chosen

def-species fe cr c

@@ Reject all phases and restore the ones you are interested in. Here austenite and cementite is chosen

rej ph * all

res ph fcc cementite

get

@@
@@ SWITCH TO MOBILITY DATABASE TO RETRIEVE MOBILITY DATA
@@

app mobfe1

@@Specify which elements you have in your system. Here Iron, Chromium and Carbon is chosen

def-species fe cr c

@@ Reject all phases and restore the ones you are interested in. Here austenite and cementite is chosen

rej ph * all
res ph fcc cementite
get


@@
@@ ENTER THE DICTRA MONITOR
@@
```

Appendix B

```
go d-m

@@
@@ ENTER GLOBAL CONDITION TEMPERATURE AND PRESSURE
@@

@@ Temperature in Kelvin

set-cond glob t 0 1273; * n

@@ Pressure in Pascal

set-cond glob p 0 4e9; * n

@@------------------------------------------------------------------------
@@ CELL NUMBER ONE
@@------------------------------------------------------------------------

@@
@@ ENTER REGIONS carb AND aus and attach region aus to carb
@@
enter-region carb
enter-region aus
carb
y

@@
@@ ENTER GEOMTRICAL GRIDS INTO THE REGIONS
@@



@@
@@ THE SIZE OF THE CEMENTITE PARTICLES WE KNOW SINCE WE ASSUME
@@ IT HAS BEEN MEASSURED.
@@

@@Size is entered in radius of the carbide. 16 Gridpoints is entered with a geometrical function to
@@ensure narrower distribution of gridpoints near the interface


enter-grid
carb
0.25e-6
Geo
```

```
16
0.80


@@ THE SIZE OF THE FCC REGION WE MAY CALCULATE FROM A MASSBALANCE
@@ AFTER ESTIMATING THE INITIAL COMPOSITIONS IN THE TWO PHASES.

@@
@@Size is entered in thickness of the austenite. 20 Gridpoints is entered with a geometrical function to
@@ensure narrower distribution of gridpoints near the interface

enter-grid
aus
0.452e-6
Dou
20
1.25
0.8

@@
@@ ENTER PHASES INTO REGIONS
@@

@@
@@ Enter an active cementite phase in the carbide
@@

enter-phase
act
carb
matrix
cementite

@@
@@ Enter an active austenite phase in the matrix
@@

enter-phase
act
aus
matrix
fcc#1
```

```
@@
@@ ENTER INITIAL VALUES FOR THE COMPOSITIONS IN THE PHASES
@@

@@Here a linear composition in weight fraction is entered

@@Chromium content in the carbide

enter-composition carb cementite w-f

cr lin 0.09 0.09

@@Chromium and carbon content in the austenite matrix
@@

enter-composition aus fcc#1 fe w-f
cr lin 0.01 0.01

c lin 0.007 0.007

@@----------------------------------------------------------------
@@ CELL NUMBER TWO
@@----------------------------------------------------------------

create-new-cell
2

@@
@@ ENTER REGIONS carb AND aus and attach region aus to carb
@@

enter-region carb
enter-region aus
carb
y

@@
@@ ENTER GEOMETRICAL GRIDS INTO THE REGIONS
@@

@@Size is entered in radius of the carbide. 16 Gridpoints is entered with a geometrical function to
@@ensure narrower distribution of gridpoints near the interface

enter-grid carb
0.125e-6
geo
```

```
16
0.80

@@
@@Size is entered in thickness of the austenite. 20 Gridpoints is entered with a geometrical function to
@@ensure narrower distribution of gridpoints near the interface

enter-grid aus 0.226e-6 dou 20 1.25 0.80

@@
@@ ENTER PHASES INTO REGIONS
@@

@@
@@ Enter an active cementite phase in the carbide
@@

enter-phase act carb matrix cementite

@@
@@ Enter an active austenite phase in the matrix
@@

enter-phase act aus matrix fcc#1

@@
@@ ENTER INITIAL VALUES FOR THE COMPOSITIONS IN THE PHASES

@@Here a linear composition in weight fraction is entered
@@Chromium content in the carbide

enter-composition carb cementite w-f

cr lin 0.09 0.09

@@Chromium and carbon content in the matrix

enter-composition aus fcc#1 fe w-f
cr lin 0.01 0.01
c lin 0.007 0.007
```

Appendix B

```
@@----------------------------------------------------------------
@@ CELL NUMBER THREE
@@----------------------------------------------------------------

create-new-cell
3

@@
@@ ENTER REGIONS carb AND aus and attach region aus to carb
@@
enter-region carb
enter-region aus
carb
y

@@
@@ ENTER GRIDS GEOMTRICAL GRIDS INTO THE REGIONS
@@Size is entered in radius of the carbide. 16 Gridpoints is entered with a geometrical function to
@@ensure narrower distribution of gridpoints near the interface

enter-grid carb 0.1e-6 geo 16 0.80

@@
@@Size is entered in thickness of the austenite. 20 Gridpoints is entered with a geometrical function to
@@ensure narrower distribution of gridpoints near the interface

enter-grid aus 0.181e-6 dou 20 1.25 0.80

@@
@@ ENTER PHASES INTO REGIONS
@@

@@
@@ Enter an active cementite phase in the carbide
@@

enter-phase act carb matrix cementite

@@
@@ Enter an active austenite phase in the matrix
@@
enter-phase act aus matrix fcc#1
```

Appendix B

```
@@
@@ ENTER INITIAL VALUES FOR THE COMPOSITIONS IN THE PHASES
@@

@@Here a linear composition in weight fraction is entered
@@Chromium content in the carbide
enter-composition carb cementite w-f
cr lin 0.09 0.09

@@Chromium and carbon content in the matrix
enter-composition aus fcc#1 fe w-f
cr lin 0.01 0.01
c lin 0.007 0.007

@@----------------------------------------------------------------
@@ GLOBAL CONDITIONS
@@----------------------------------------------------------------



@@
@@ SET SPHERICAL GEOMETRY
@@

enter-geo 2

set-numerical-limits

@@
@@ SET THE SIMULATION TIME
@@First number is simulation time, y is for automatic timestep control, next number is the maximum
timestep,initial time step and finally lowest acceptable timestep

set-simulation-time

5e-4
y
1e-6
1e-07
1e-07



@@
@@ SAVE THE SETUP ON A NEW STORE FILE
@@
```

Appendix B

```
save Name

@@
@@ RUN SIMULATION
@@

Sim


@@
@@ POST PROCESSOR
@@

@@
@@ PLOT CHROMIUM AND CARBON CONCENTRATION PROFILES
@@


@@ Set a global distance on x-axis

set-diagram -axis  x dist glo

@@ Set  weight fraction of chromium on y-axis
set-diagram -axis  y w(cr)

@@ Select time for plot
set-plot-condition time 1e-4

@@ Set title on diagram and plot on screen

set-title “Chromium profile”
plo SCREEN

@@ Change to weight fraction of carbon on y-axis
set-diagram -axis  y w(c)

@@Set new title and plot again

set-title “Carbon profile”
plo SCREEN


@@
@@ SELECT CELL 2 AND REPEAT
@@
```

Appendix B

```
@@ Set a global distance on x-axis

set-diagram -axis  x dist glo

@@ Set  weight fraction of chromium on y-axis
set-diagram -axis  y w(cr)

@@ Select time for plot
set-plot-condition time 1e-4

@@ Set title on diagram and plot on screen

set-title “Chromium profile”
plo SCREEN

@@ Change to weight fraction of carbon on y-axis
set-diagram -axis  y w(c)

@@Set new title and plot again

set-title “Carbon profile”
plo SCREEN

@@
@@ SELECT CELL 3 AND REPEAT
@@

select-cell 3

@@ Set a global distance on x-axis

set-diagram -axis  x dist glo

@@ Set  weight fraction of chromium on y-axis
set-diagram -axis  y w(cr)

@@ Select time for plot
set-plot-condition time 1e-4

@@ Set title on diagram and plot on screen

set-title “Chromium profile”
plo SCREEN

@@ Change to weight fraction of carbon on y-axis
set-diagram -axis  y w(c)

@@Set new title and plot again
```

```
set-title “Carbon profile”
plo SCREEN

@@
@@ PLOT HOW THE DIAMETER OF THE CEMENTITE PARTICLE VARIES
@@ WITH TIME IN THE THREE CELLS
@@

@@
@@ SELECT FIRST CELL
@@

sel-cell  1

@@ set time on x-axis

s-d-a x time
@@ set upper and lower limit of time to be plotted
set-scaling-status x n .01 10000

@@ set a logarithmic scale on x-axis
set-axis-type x log

@@ Enter diameter function

enter func diam1=2*poi(carb,u);

@@ Set the function on the y-axis
s-d-a y diam1

@@ set upper and lower limit of diameter to be plotted
s-s-s y n 0 1.5e-6
@@ select the interface to be plotted
set-plot-condition interf carb upp

@@ Set title on diagram and plot on screen
set-title “Diameter change”
plo SCREEN



@@
@@ SELECT CELL 2 AND REPEAT
@@

sel-cell 2
```

```
@@ set time on x-axis

s-d-a x time
@@ set upper and lower limit of time to be plotted
s-s-s x n .01 10000

@@ set a logarithmic scale on x-axis
set-axis-type x log

@@ Enter diameter function

enter func diam2=2*poi(carb,u);

@@ Set the function on the y-axis
s-d-a y diam2

@@ set upper and lower limit of diameter to be plotted
s-s-s y n 0 1.5e-6
@@ select the interface to be plotted
s-p-c interf carb upp
@@ Set title on diagram and plot on screen
set-title “Diameter change”
plo SCREEN

@@
@@ SELECT CELL 3 AND REPEAT
@@

@@ set time on x-axis

s-d-a x time
@@ set upper and lower limit of time to be plotted
s-s-s x n .01 10000

@@ set a logarithmic scale on x-axis
set-axis-type x log

@@ Enter diameter function

enter func diam3=2*poi(carb,u);

@@ Set the function on the y-axis
s-d-a y diam3
```

Appendix B

```
@@ set upper and lower limit of diameter to be plotted
s-s-s y n 0 1.5e-6
@@ select the interface to be plotted
s-p-c interf carb upp

@@ Set title on diagram and plot on screen
set-title “Diameter change”
plo SCREEN
```